TECHNISCHE UNIVERSITÄT MÜNCHEN

Wetting Behavior of Titanium Carbide Films for Carbon-Copper Braze Joints in High Heat Flux Components

Peter Worbs

Vollständiger Abdruck der von der Fakultät für Maschinenwesen der Technischen Universität München zur Erlangung des akademischen Grades eines

Doktor – Ingenieurs

genehmigten Dissertation.

Vorsitzender:	Univ.-Prof. Dr.-Ing. H. Baier
Prüfer der Dissertation:	1. Hon.-Prof. Dr.-Ing., Dr.-Eng. (Univ. Nagoya/Japan) H. H. Bolt
	2. Univ.-Prof. Dr. mont. habil. E. Werner

Die Dissertation wurde am 25.06.2009 bei der Technischen Universität München eingereicht und durch die Fakultät für Maschinenwesen am 13.10.2009 angenommen.

Für meine Familie

Abstract

The divertor design of future fusion machines like ITER or WENDELSTEIN 7-X comprises joints between carbon fiber reinforced carbon matrix composites (CFC) and the copper alloy heat sink. These joints must operate under vacuum conditions and withstand cyclic thermal, mechanical and neutron loads. One approach of the joint manufacturing is the CFC/Cu brazing technology developed by the Italian company, Ansaldo Ricerche, which foresees the use of a commercial Cu–Ti active brazing alloy (Copper-ABA®). Due to an insufficient penetration of the CFC pores by this brazing alloy, the sudden change of physical and mechanical properties across the CFC/Cu joint and the presence of intermetallic compounds formed by the titanium atoms that do not react with the CFC surface, the control of the wettability during the CFC/Cu joint manufacturing process is of high relevance.

The main focus of this work was to investigate the wettability behavior of thin titanium carbide films (TiC_x). The goal was to improve the brazing procedure of CFC/Cu high heat flux components by the introduction of a wetting enhancing thin TiC_x film in order to obtain a good anchorage to the porous CFC and hence a better component adhesion under thermal and mechanical exposures.

Thin TiC_x films with stoichiometries from pure titanium to stoichiometric TiC ($0 \leq x \leq 1$) were produced by dual magnetron sputter deposition. For these films three crystallinity ranges were determined by X-ray diffraction: the α-Ti phase (hcp structure) for $x = 0$, the TiC phase (fcc structure) for $x = 0.6 - 1$ and a distorted or metastable crystallinity for $0 < x < 0.6$. Under certain deposition conditions, magnetron sputter deposited TiC_x films exhibited high compressive film stresses resulting in extensive buckling and delamination. Therefore, systematic investigations of the intrinsic film stress were performed using both, the curvature and the $\sin^2\psi$ method. Low-stress coatings could be achieved by varying the deposition parameters power density, C/Ti power ratio and the argon gas pressure. The wettability behavior of Copper-ABA on TiC_x films was characterized by the sessile drop method. For these experiments a contact angle measurement device was constructed and successfully tested. The tests have shown that due to the high titanium activity in the Copper-ABA alloy, every sample was wetted at a low final contact angle. The significantly highest spreading velocities of Copper-ABA droplets were achieved for magnetron sputter deposited $TiC_{0.9}$ films. Thus, the wetting behavior of Copper-ABA on carbon materials can be improved by coating of TiC_x films, which already exist in the face-centered cubic TiC crystal phase ($x = 0.6 - 1$).

Subsequently, TiC_x modified CFC/Cu braze joints were tested on their ability to withstand thermal and mechanical loads. Shear strength experiments have shown, that the modification by thin TiC_x films do not increase the CFC/Cu bonding strength. An increase of the shear strength by a factor of 2 and more was only achieved by oxygen plasma treatment of the initial CFC surface. Thermal fatigue tests at the high heat flux test facility GLADIS have shown that, according to the wetting test results, magnetron sputter deposited TiC_x coatings in the range of $x = 0.6 - 1$ improve the long-term performance of brazed CFC/Cu/CuCrZr components under high heat flux loadings and are possible candidates to be implemented in actively cooled divertor applications.

Kurzfassung

Der Divertorentwurf von zukünftigen Fusionsanlagen wie ITER oder WENDELSTEIN 7-X sieht Verbindungen zwischen faserverstärktem Kohlenstoff (Engl.: **C**arbon **F**iber reinforced **C**arbon, CFC) und Wärmesenken aus einer speziellen Kupferlegierung vor. Diese Verbindungen müssen den Anforderungen unter Vakuum genügen und mechanischen und thermisch zyklierenden Belastungen sowie den Beschuss durch Neutronen standhalten. Eine Herstellungsmethode dieser CFC/Cu Verbindung ist eine Löttechnologie, welche vom italienischen Unternehmen Ansaldo Ricerche entwickelt wurde. Sie sieht die Benutzung einer aktiven kommerziell erhältlichen Cu-Ti Lötlegierung (Copper-ABA®) vor. Aufgrund ungenügendem Eindringungsvermögen dieses Lotes in die CFC Poren, unterschiedlichen physikalischen und mechanischen Eigenschaften der Bestandteile des CFC/Cu Verbundes und die Entstehung von intermetallischen Verbindungen durch Titan, welches nicht mit der CFC Oberfläche reagiert hat, ist die Kontrolle des Benetzungsverhaltens während der Herstellung des CFC/Cu Verbundes von hoher Relevanz.

Das Hauptaugenmerk dieser Arbeit war die Untersuchung des Benetzungsverhaltens von dünnen Titancarbid Schichten (TiC_x). Das Ziel war, das Lötverfahren von CFC/Cu Komponenten durch die Einführung einer benetzungsfördernden dünnen TiC_x Schicht zu verbessern, um eine gute Verankerung im porösen CFC und daher eine bessere Haftung unter thermischen und mechanischen Belastungen zu erhalten.

Dünne TiC_x Schichten mit einer Zusammensetzung zwischen reinem Titan und stöchiometrischem TiC ($0 \leq x \leq 1$) wurden mittels Magnetronsputtern an zwei Kathoden hergestellt. Durch Röntgenbeugung wurden für diese Schichten drei Kristallinitätsbereiche festgestellt: die α-Ti Phase (hdp Struktur) für $x = 0$, die TiC Phase (kfz Struktur) für $x = 0.6 - 1$ und eine gestörte oder metastabile Kristallinität für $0 < x < 0.6$. Unter bestimmten Beschichtungsbedingungen wiesen diese TiC_x Schichten hohe Druckspannungen auf, welches zu Schichtversagen durch Stauchung und zu Abplatzungen führte. Daher wurden unter Verwendung der Stoney- und der $\sin^2\psi$ Methode systematische Untersuchungen zur intrinsischen Schichtspannung durchgeführt. Nahezu spannungsfreie Schichten konnten durch Variation der Beschichtungsparameter Leistungsdichte, Verhältnis der Leistungen C/Ti und des Argon Gasdruckes erzielt werden. Das Benetzungsverhalten von Copper-ABA auf TiC_x Schichten wurde mit der sogenannten *sessile drop* Methode charakterisiert, für das eine eigens konstruierte Anlage aufgebaut wurde. Die Untersuchungen zeigten, dass aufgrund der hohen Titan Aktivität im Copper-ABA Lot jede Probe unter einem niedrigen Endkontaktwinkel benetzt wurde. Die signifikant höchste Ausbreitungsgeschwindigkeit eines Copper-ABA Tropfens wurde für gesputterte $TiC_{0.9}$ Schichten erreicht. Das Benetzungsverhalten von Copper-ABA auf Kohlenstoffmaterialien kann daher durch die Beschichtung von TiC_x Schichten verbessert werden, welche bereits in der kubisch-flächenzentrierten TiC Kristallstruktur ($x = 0.6 - 1$) existieren.

Anschließend wurden TiC_x modifizierte CFC/Cu Lötverbindungen auf ihre Fähigkeit, thermische und mechanische Belastungen zu überstehen, getestet. Versuche unter Scherbelastung haben gezeigt, dass die CFC/Cu Haftfestigkeit durch dünne TiC_x Schichten nicht erhöht werden kann. Ein Anstieg der Scherfestigkeit um den Faktor 2 und höher wurde nur durch eine

Sauerstoff-Plasma Behandlung der ursprünglichen CFC Oberfläche erreicht. Thermische Ermüdungsversuche am Wärmeflussteststand GLADIS haben gezeigt, dass, in Übereinstimmung mit den Benetzungsergebnissen, gesputterte TiC_x Schichten im Bereich von $x = 0.6 - 1$ die Beständigkeit von gelöteten CFC/Cu/CuCrZr Komponenten unter hoher Wärmebelastung verbessern. Diese sind damit mögliche Kandidaten, um in aktiv gekühlten Divertor Anwendungen eingesetzt zu werden.

Contents

1 Introduction

Safe and sustainable energy supply for a growing world population with increasing energy demand is one of the most important issues mankind has to deal with in the coming decades. By 2030, the world's primary energy demand will increase by nearly 50% [1]. Presently, more than 80% of the consumed energy is based on fossil fuels. The maximum output of oil is expected in about 10-20 years, whereas coal will be available for more than 100 years [2]. Despite the resource issue, the effect of global warming will force us to drastically reduce the production of the greenhouse gas CO_2, associated with the burning of carbon-based fuels[1].

Since nuclear fission (applied as fast breeder technique) is hardly an option due to unsolved disposal, proliferation and safety policy issues, only three main long term primary energy sources remain: solar energy (i.e. all renewable energies), geothermal energy and nuclear fusion.

1.1 Nuclear fusion as energy source

Energy generation by nuclear fusion – which is actually the origin of solar energy – utilizes the fact that the nuclear binding energy of the atom formed (e.g. helium) is larger than that of the original light atoms (e.g. hydrogen isotopes) that undergo fusion, i.e. energy is released. The most promising reaction on earth is fusion of the hydrogen isotopes deuterium and tritium proceeding at about 100 Mio K in a plasma reactor with magnetic confinement [4]:

$$D + T \longrightarrow {}^4He\,(3.5\,MeV) + n\,(14.1\,MeV)$$

Utilizing the heat generated from impacting neutrons and particles, electrical energy will be generated via a conventional steam process.

Resources required for this type of energy generation are available for centuries. Deuterium can be extracted from abundant sea water, whereas tritium will be bred from lithium, which is widespread in the earth's crust. Nevertheless, due to immense technological challenges, a commercial fusion plant is not expected before mid-century. During some years of operation, a fusion plant will accumulate radioactive inventory due to activation of materials by neutron irradiation. The total amount generated is comparable to fission plants, but the much lower half-life of the formed radioactive isotopes leads to timescales for safe storage of only about 100–150 years. This is much less compared to the nuclear waste generated from fission reactors, which has to be safely stored for thousands of years.

[1] According to the 2007 IPCC report an absolute reduction of greenhouse gas emissions of 50 – 85% in 2050 (based on the year 2000) is required to stabilize the global temperature increase to 2 – 2.4°C since the beginning of industrialization [3].

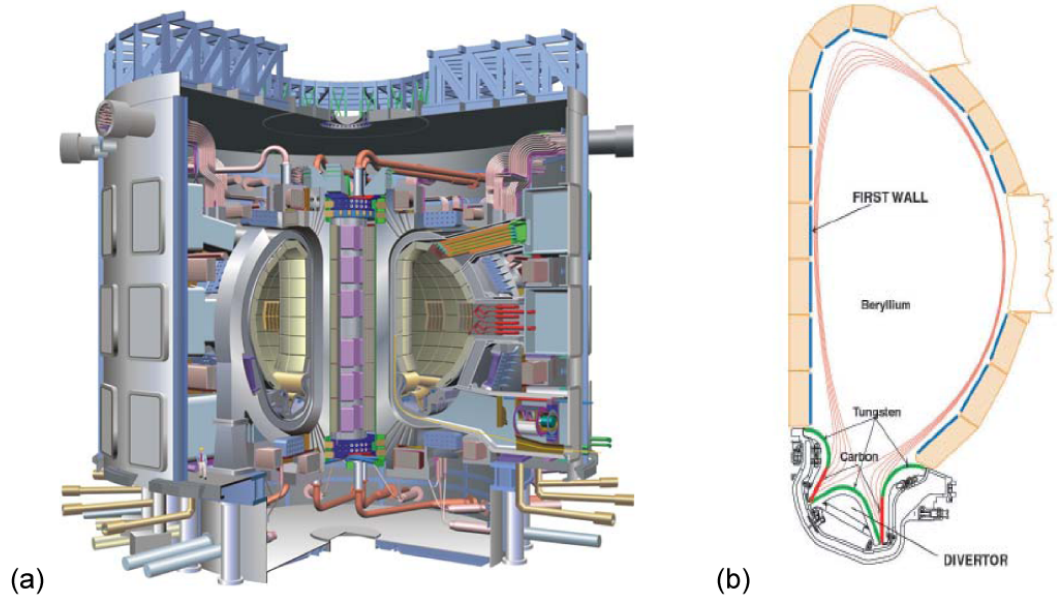

Figure 1.1: (a) Principal design of ITER, the next-step fusion device to be built in Cadarache, France. The person on the left gives a rough scale on the dimensions. Source: www.iter.org. (b) ITER cross-section with the divertor system at the bottom. The different wall materials Be, W and C are located as indicated. The red lines represent the poloidal magnetic flux surfaces. Taken from [5].

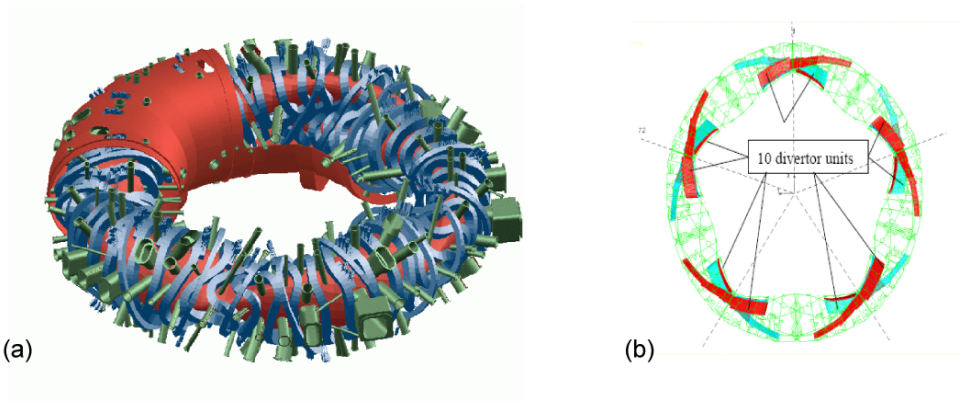

Figure 1.2: (a) Cryostat, magnetic coils and plasma vessel of WENDELSTEIN 7-X, the next stellarator experiment currently under construction in Greifswald, Germany. The major plasma radius will reach 5.5 m. Source: www.ipp.mpg.de. (b) WENDELSTEIN 7-X top view with amount and positions of the divertor units installed symmetrically inside the plasma vessel along the plasma column. Taken from [6].

Controlled nuclear fusion has been studied for about 60 years, and is now on the border of demonstrating its feasibility for power generation. In 1997, JET, the largest fusion experiment built yet, achieved a fusion power of 16 MW, 65% of the power consumed for heating the plasma. This is expressed by the fusion energy gain factor Q, which is 0.65 for that JET experiment. The joint international research and development project ITER, shown schematically in fig. 1.1 (a), aims "to demonstrate the scientific and technological feasibility of fusion

power for peaceful purposes". Projected to be built in France between 2009 and 2016, ITER will be the first experiment realizing a net energy gain with $Q > 5 - 10$ and operate at quasi steady-state.

Up to now, two different types of experiment have been developed for possible fusion reactors, the tokamak and the stellarator. Most of the devices in the world today are of the tokamak type, which is best investigated and comes closest to the ignition conditions. ITER will be a tokamak as well. Both types feature ring-shaped magnetic fields. Tokamaks produce a part of these fields by means of an electric current flowing in the plasma. Stellarators, on the other hand, form the magnetic field cage solely by means of external coils. Stellarators are thus suitable for continuous operation, whereas tokamaks without auxiliary facilities can only work in pulsed mode. However, a complicated shape of the stellarator's magnetic coils makes it quite difficult and expensive for manufacturing. Nevertheless, the WENDELSTEIN 7-X stellarator (see fig. 1.2 (a)), now being built at the Greifswald branch of the Max-Planck-Institut für Plasmaphysik, will test a magnetic field optimized to overcome the difficulties of previous stellarator concepts.

1.2 Divertor design of future fusion machines

The divertor of a nuclear fusion reactor is the component being exposed to the highest particle impacts and heat loads. About 15% of the energy produced by fusion reactions must be removed through the divertor yielding a thermal load of up to 20 MW/m^2, which constitutes a significant technical challenge. The main function of the divertor system is to exhaust the flow of energy from charged particles and to remove helium and other impurities resulting from the reactions and from interactions of plasma particles with the material walls [7].

The divertor configurations proposed so far can be classified into two distinct categories: monoblock and flat tile (see fig. 1.3). In the monoblock geometry a round hole is obtained in each armor tile by drilling. Then the cooling tube is inserted and joined to the armor. The flat tile geometry consists in a copper alloy heat sink with a rectangular external cross section. Armour flat tiles are then joined onto the plasma facing surface. The cooling channel can be either round or rectangular.

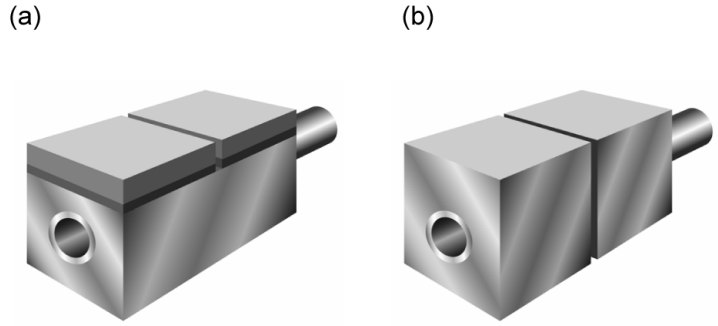

Figure 1.3: Divertor design of future fusion machines: (a) flat tile and (b) monoblock configuration. Source: I. Smid, Pennsylvania State University

In ITER, mainly tungsten ($\approx$100 m^2) will be applied in the actively cooled divertor (located at the bottom of the reactor, see fig. 1.1 (b)) since it is able to handle the expected heat loads of $\approx$3 MW/m^2 while possessing a high sputtering threshold [8]. The divertor *strike point*

region has to withstand up to 20 MW/m^2, which requires 75 m^2 carbon in form of tiles of carbon fiber reinforced carbon (CFC). Carbon fiber composites have been selected as plasma facing material due to their excellent thermal shock resistance, high temperature resistance in comparison to the melting point of metals, ability to retain the strength up to high temperature and good thermal conductivity, which allows using a thick sacrificial armor [9].

WENDELSTEIN 7-X is equipped with an actively cooled divertor, which yields an effective exhaust of energy and particle fluxes (see fig. 1.2 (b)) [10]. The target areas, which follow the plasma column, are the interaction zones with the open field lines at the plasma boundary. They are designed to remove up to 10 MW/m^2 convective stationary heat load for long pulse operation up to 30 min [11]. The 19 m^2 of the heavily loaded baffle plates of the WENDELSTEIN 7-X divertor are manufactured from precipitation hardened CuCrZr and CFC, which is a material combination that has also been proposed for ITER and qualified by prototypes.

The divertor design of future fusion machines comprises joints between CFC armor tiles and the CuCrZr heat sink. These joints must operate under vacuum conditions and withstand cyclic thermal, mechanical and neutron loads. In particular, the ITER divertor shall sustain 3000 cycles at 10 MW/m^2 plus 300 cycles at 20 MW/m^2 [12]. The WENDELSTEIN 7-X divertor is designed to withstand a heat flux up to 10 MW/m^2 and a maximum total load of 10 MW for steady state operation [10]. Furthermore, the joints must have an adequate lifetime and reliability in order to limit the overall cost of the component. The main problem related to the CFC/CuCrZr joints is the large thermal expansion mismatch between the two materials (α_{CFC} = -0.2 – 1.5 $\cdot$ 10^{-6} K^{-1}, for directions parallel to the CFC/CuCrZr interface; α_{CuCrZr} = 16 – 20 $\cdot$ 10^{-6} K^{-1} [13,14]), which generates large residual stresses at the interface during the joining process and leads to fatigue induced delamination at the interface under extreme thermal loads, i.e. high heat fluxes. These residual stresses can partially relax by the introduction of a 0.5 – 2 mm ductile layer of pure copper between the CFC composite and CuCrZr [15]. Furthermore, the very large contact angle θ of molten copper on carbon materials (θ = 122° [16]) does not allow the direct bonding of pure copper to CFC. The C–Cu system is a non-reactive system: C and Cu are not soluble in the solid state and they do not form stable carbides.

1.3 CFC/Cu bonding techniques for divertor components

To overcome the problems identified in the previous section, acceptable CFC/Cu bonding techniques have to be developed to provide effective joining methods for divertor components. A wettability study is of great importance for several applications such as coating and joining processing.

In the early 1970s, Mortimer and Nicholas [17] studied the improving of copper bonding to vitreous carbon and graphite with small amounts of active metals. Their investigation focused on segregation of active metals at the interface and subsequent carbide production, being able to improve copper adhesion to the reaction layer. From literature, it is known that transition metals react strongly with carbon to form carbides and some of these carbides are wetted by copper. The metal-like carbides of the transition metals are wetted better than the covalent carbides. In fact, these carbides have a partly metallic bonding, which improves the interfacial adhesion to metals. Furthermore, these ceramics have metal-like behavior such as good electrical and thermal conductivities. The latter is one of the main requirements in divertor CFC/Cu joints [16–20].

Up to now, four possible solutions are available in Europe for CFC/Cu joints:

- The active metal casting (AMC®) has been developed by the Austrian company Plansee AG and consists in the casting of pure copper on the laser-machined CFC surface previously activated by CVD or PVD titanium [21]. Recently, beside titanium, silicon is also employed during the AMC process [22].

- The second method, which is pursued by the Materials Science and Chemical Engineering Department of the Polytecnico di Torino, Italy, consists in the CFC surface modification by solid-state reaction with chromium (slurry deposition) followed by the direct joining of copper [23].

- Another technique, developed by the Italian Association ENEA, investigates the possibility of using a commercial copper – titanium – nickel brazing alloy to activate the CFC surface and to allow a proper joining between the cast copper and the CFC [24].

- Finally, direct brazing of copper to CFC was developed by the Italian company, Ansaldo Ricerche. This technology foresees the use of a commercial Cu–Ti active brazing alloy (Copper-ABA®) with good wetting characteristics on the CFC surface [25].

These joining techniques have in common that they use activating transition metals (e.g. Ti, Cr) in order to form metal-like carbides at the CFC/Cu bonding interfaces. All of them are silver-free joints to avoid cadmium as transmutation product of the neutron irradiation affecting the divertor modules of a nuclear fusion reactor.

The subsequent Cu/CuCrZr joint can be obtained by several methods, e.g. hot isostatic pressing (900°C, 1000 bar) followed by a heat treatment to restore the overaged CuCuZr alloy [22] or by brazing with a commercial copper – germanium – nickel alloy (Gemco®) at the annealing temperature of 975°C followed by a rapid cooling (> 1 °C/s) and later ageing at 475°C for 3 h to maintain the good mechanical properties of the CuCrZr alloy [26]. For the brazing technologies a single-step process to join both, the CFC/Cu and the Cu/CuCrZr interfaces, at the same time is shown to be possible, e.g. in [27].

The CFC/Cu bonding technologies for divertor components have been extensively tested in many efforts and nevertheless, experiments are still ongoing. Actively cooled mock-ups were subjected to high heat flux loadings using facilities like JUDITH (Forschungszentrum Jülich, Germany) [28] and GLADIS (Max-Planck-Institut für Plasmaphysik Garching, Germany) [29]. However, bonding defects, namely cracks, dewetting and delamination, could be observed regularly (see fig. 1.4). Even if a soft Cu interlayer mitigates most of the residual stress by plastic deformation, the interface stress from the manufacturing process is still high. Furthermore, the sudden change of physical and mechanical properties across the CFC/Cu joint and the presence of intermetallic compounds formed by the transition metals that do not react with the CFC surface are detrimental to thermal fatigue lifetime [25]. The insufficient penetration of CFC pores turned out to be a main bonding drawback, especially for brazing technologies. Here, the brazing alloys formed solid carbide bridges over the CFC pores, which results in a poor anchorage to the porous CFC and hence in a poor component adhesion under thermomechanical exposures. Thus, the control of the wettability during the CFC/Cu joint manufacturing process is of high relevance.

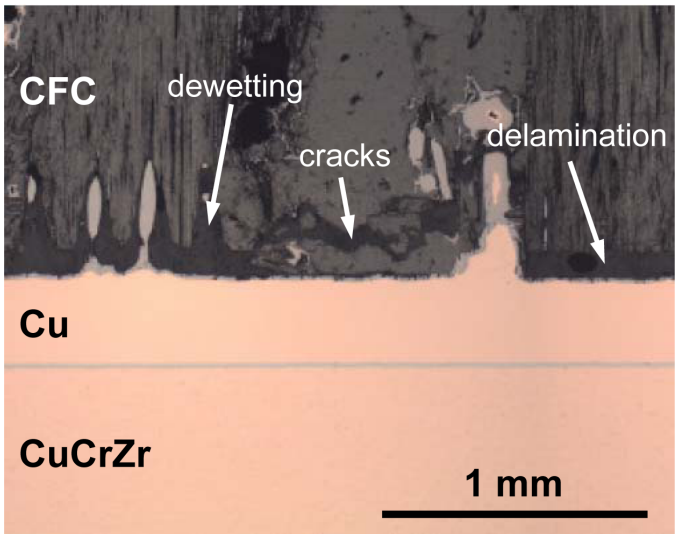

Figure 1.4: Typical bonding defects of CFC/Cu joints: cracks, dewetting and delamination. The image was made after testing an AMC (active metal casting) copper to CFC joint in the high heat flux facility JUDITH (Forschungszentrum Jülich, Germany). Picture illustrated with permission of the European organization Fusion for Energy.

1.4 Objectives

The CFC/Cu brazing technology for manufacturing divertor components has advantages in terms of industrialization and cost reduction. However, brazing is affected by the mismatch of the thermal expansion and by the poor wetting of the CFC surface. Furthermore, the requirement of silver-free brazing reduces the available filler alloys. R&D has been carried out by Ansaldo Ricerche to investigate the high temperature brazing using silver-free alloys. Thus, wetting can be improved by using an active Cu–Ti brazing alloy, namely Copper-ABA®, where the Ti reacts with carbon and forms a thin TiC layer that promotes wetting [25]. The composition of the brazing alloy is 86.5 *at.*% Cu, 2.8 *at.*% Ti, 6.3 *at.*% Si and 4.4 *at.*% Al and its solidus and liquidus temperature are 958°C and 1024°C, respectively. It turned out that the CFC/Cu brazing technology is affected by the bonding defects described in the previous section. An insufficient penetration of CFC pores by the Copper-ABA brazing alloy requires further R&D to control and enhance the wettability of CFC surfaces.

Many efforts have been made in this direction, e.g. the addition of carbon fibers to the brazing alloy, which smoothes the transition between CFC and Cu and traps the Ti excess with beneficial effects on the wettability and the thermal fatigue strength of the CFC/Cu joint [25]. The idea of this work is to deposit thin films on CFC surfaces, which should promote the wettability behavior of possible brazing alloys, but especially of Copper-ABA. The aim is to improve the brazing procedure of CFC/Cu flat tile divertor components by the introduction of a wetting enhancing thin film in order to obtain a good anchorage to the porous CFC and hence a better component adhesion under thermal and mechanical exposures.

The wetting enhancing thin film should be a metal-like nitride or carbide including an active transition metal (e.g. Ti, Cr, W), because they show an adequate wetting behavior in many metal-ceramic applications [17, 18]. In fact, these nitrides or carbides have a partly metallic bonding, which improves the interfacial adhesion to metals. The activity of titanium is very

high compared to other transition metals [30,31]. Concerning film species and way of deposition different alternative concepts of thin wetting promoting films have been developed within the framework of the integrated project "ExtreMat" (Contract NMP-CT- 2004-500253) with financial support by the European Community. Possible candidates are for example reactively sputter deposited WN_x or TiN_x films with good wettability properties [32–37]. Besides, it has been suggested that TiC_x films are one of the most promising coatings for improving the wettability behavior in CFC/Cu brazing applications [32]. The main purpose of this work is to investigate the feasibility of producing such TiC_x films, their characterization and their applicability as wetting promoting films in divertor components. Further, the influence of different stoichiometric Ti/C ratios has to be analyzed.

TiC films are characterized by their excellent physical and mechanical properties: high hardness, high melting point, high electrical conductivity, etc. These properties have led to their wide applications as aerospace structural components, coating materials for surface protection of cutting tools and thin films for electronic devices [31,38]. At room temperature they are chemically stable and present excellent oxidation resistance [39].

The basis of this work is the evaluation of a wetting improving behavior of thin TiC_x films using an adequate characterization method and the subsequent implementing of these films in CFC/Cu braze joints for test series in divertor-like flat tile mock-ups. Thin TiC_x films were produced by the magnetron sputter deposition technique, a well-established Physical Vapor Deposition (PVD) method, that offers a variety of deposition parameters in order to tailor the coatings properties and to adjust a specific stoichiometry. In addition, titanium carbide films were created by Chemical Vapor Deposition (CVD) to utilize the unique feature of CVD compared to other deposition techniques, the non-line-of-sight-deposition capability, which has allowed the coating of complex components like the porous CFC.

Background information on TiC_x structures, the thin film deposition techniques used in this work and on the main applied characterization techniques are summarized in chapter 2. The experimental details are given in chapter 3. Chapter 4 describes the **characterization** of the deposited TiC_x films, e.g. film stoichiometry, crystal structure and morphology. It turned out that it is important to control the internal stress state of the films. Wetting properties of TiC_x films will be presented using the brazing relevant alloys Copper-ABA and Gemco. Results of the **implementation** of thin TiC_x wetting promoting films in braze joined CFC/Cu components are shown in chapter 5. Their impact will be evaluated by testing of TiC_x modified CFC/Cu braze joints on their ability to withstand mechanical loads. Further, the overall thermal performance of actively cooled TiC_x modified CFC/Cu/CuCrZr flat tile divertor mock-ups will be estimated under high heat flux loadings in the test facility GLADIS. Chapter 6 gives an assessment of the performance of these implementation tests.

2 Background knowledge

2.1 TiC_x structures

This section gives the general characteristics of strongly nonstoichiometric titanium carbide compounds (TiC_x) which are interstitial phases and it describes their crystal structures and homogeneity interval. The position of the lower boundary of the homogeneity interval is discussed in detail.

In nonstoichiometric compounds the chemical composition does not coincide with the concentration of crystal lattice sites for different species of the compound. Strongly nonstoichiometric TiC_x compounds are substances with structural vacancies and a homogeneity interval such that the concentration of vacancies is sufficient for their interaction [40, 41]. A homogeneity interval is a concentration region within which the crystal structure of a compound or a substitutional solid solution remains unchanged if the composition is changed.

Compounds of groups IV and V transition metals with carbon have a similar simple structure and broad homogeneity intervals [42]. Titanium is a hexagonal close-packed (hcp) transition metal of group IV (see fig. 2.1 (a)) and forms monocarbides with a face-centered cubic (fcc) metallic sublattice. The basic crystal structure of fcc titanium carbide is of type $B1$ (NaCl) and space group $Fm\bar{3}m$ (see fig. 2.1 (b)). This structure can be visualized as successively alternating layers of atoms of unlike species perpendicular to the direction $[1\,1\,1]_{B1}$ (or perpendicular to equivalent directions). The alternation of metallic atomic planes provides a sequence of ABCABC... type, i.e. the closest cubic packing. Layers formed by the nonmetallic sublattice sites alternate in the same sequence XYZXYZ.... The general alternation sequence of atomic layers in the direction $[1\,1\,1]_{B1}$ in a $B1$-type cubic structure has the form AXBYCZ AXBYCZ....

A characteristic structural feature of TiC_x compounds is the presence of hcp titanium lattice, while carbon atoms statistically fill octahedral interstitial sites of the metallic lattice.

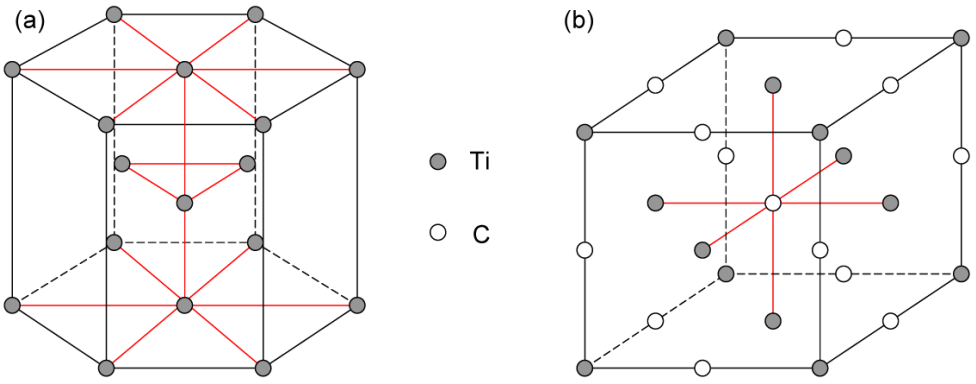

Figure 2.1: Crystal structures of (a) α-Ti with hcp lattice and (b) $B1$-type TiC (space group $Fm\bar{3}m$) with fcc lattice

However, the symmetry of the metallic lattice in titanium carbides differs from the symmetry of the crystal lattice of titanium, i.e. the titanium crystal structure is altered upon formation of TiC_x. Thus, a seemingly independent metallic sublattice serves as a matrix for carbon atoms occupying its intersite free spaces and forming the nonmetallic sublattice. Any site of the nonmetallic sublattice has an octahedral environment of six nearest sites of the metallic sublattice, whereas any metal atom has an octahedral environment of six nearest sites of the nonmetallic sublattice. Vacant interstitial sites (structural vacancies $\square$) are analogs of interstitial carbon atoms to a first approximation. Structural vacancies and interstitial carbon atoms form a substitutional solution in the nonmetallic sublattice.

According to [43], nonstoichiometric interstitial compounds are formed if the atomic radii of the metal R_M and nonmetal R_X meet the condition $0.41 < R_X/R_M < 0.59$. When this condition is fulfilled, nonmetal atoms are located at the largest interstitial sites of the metallic lattice, which are a little smaller than the interstitial nonmetal atoms. The change of symmetry and a slight expansion of the metallic lattice in carbide, nitride or oxide ensure stability of the structure. In the case of titanium carbides the atomic radii are $R_{Ti} = 0.1467\,\text{nm}$ and $R_C = 0.0772\,\text{nm}$[1], respectively and the radius ratio $R_C/R_{Ti} = 0.526$.

Group IV metal titanium form only monocarbides TiC_x with the $B1$ (NaCl) structure. A disordered nonstoichiometric compound has a homogeneity interval if the type of its crystal structure is preserved when the concentration of structural vacancies changes. TiC_x has one of the widest homogeneity intervals, from $TiC_{1.00}$ to $TiC_{0.48}$ at 1700 K [42], i.e. the carbon sublattice contains over 50 *at.*% of structural vacancies at the lower boundary of the homogeneity interval. Actually, the exact positions of the homogeneity interval differ by the authors, for example the Ti-C phase diagram [44] of Murray gives a homogeneity interval from $TiC_{0.95}$ to $TiC_{0.47}$ at 1900 K.

According to [42], the upper boundary of the homogeneity interval of TiC_x is normally a compound of stoichiometric composition ($TiC_{1.00}$) where all octahedral interstitial sites of the crystal structure are filled with carbon atoms. The change in the composition of disordered cubic TiC_x from the upper to the lower boundary of their homogeneity interval, i.e. the growth of the concentration of structural vacancies, is accompanied by the decrease in the lattice constant a_{B1} (0.4326 at $TiC_{1.00}$ to 0.4296 at $TiC_{0.48}$ [42]). The lattice constant measured by diffraction methods represents a statistical average over sizes of a multitude of unit cells. The lattice constant variation with the carbide composition $a_{B1}(x)$ can be described by a second-order polynomial ($a_{B1}(x) = b_0 + b_1x + b_2x^2$). The coefficients of the polynomial were determined from the experimental dependency of the lattice constant of TiC_x as $b_0 = 0.4216\,\text{nm}$, $b_1 = 0.0237\,\text{nm}$ and $b_2 = \text{-}0.0127\,\text{nm}$ [45]. A weak maximum in the dependence $a_{B1}(x)$ is observed for TiC_x at $x > 0.9$. If one or more structural vacancies are present in the nearest neighborhood of a titanium atom, this atom is displaced statically because of the combined asymmetric effect of the nearest neighbors. In order to provide for the experimentally observed decrease in the lattice constant of $TiC_x$the direction in which atoms can be displaced was discussed by Gusev et al. [42].

If titanium atoms shift towards a vacancy (see fig. 2.2 (a)), compression of vacant octahedral interstitial sites $\square Ti_6$ will be opposed by Ti-C interactions in adjacent occupied octahedra CTi_6. If the concentration of vacant interstitial sites, which have a smaller linear size than occupied octahedral interstitial sites, increases, the lattice constant a_{B1} will shrink provided vacancy-induced static displacements of titanium atoms decrease monotonically and

[1] Atomic radii R are given for coordination number 12, see [42].

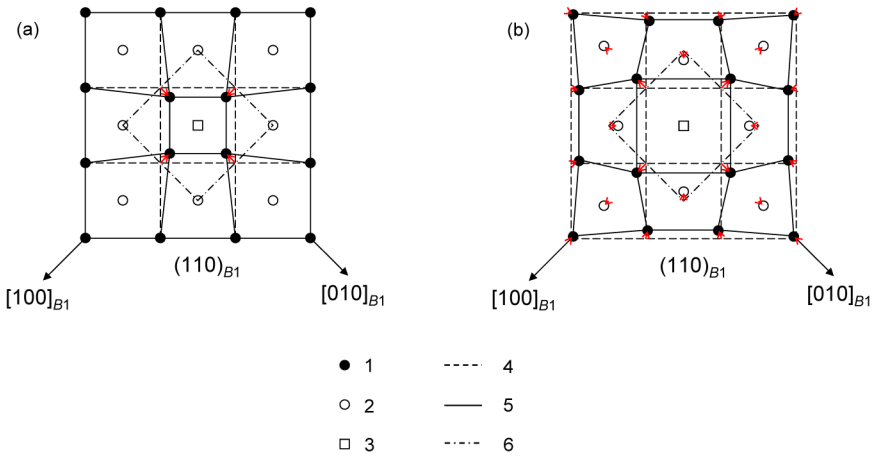

Figure 2.2: Diagrams for the model to explain the decrease of the lattice constant of nonstoichiometric TiC_x compounds with the $B1$ structure upon formation of a vacancy □ and static atomic displacements around a vacancy in the $(1\,1\,0)_{B1}$ plane (according to [42], modified): (a) nearest titanium atoms shift towards the vacancy, (b) nearest titanium atoms shift away from the vacancy; (1) titanium atom, (2) carbon interstitial atom, (3) vacancy □, (4) defect free ideal lattice, (5) real lattice taking account of atomic displacements due to a vacancy, (6) unit cell outline. Arrows show directions of displacements

tend asymptotically to zero with increasing distance from the vacancy. The lattice constant will decrease even if vacancy-induced disturbances extend to the nearest environment of a vacancy only. However, in this case it is impossible to explain the weak maximum in $a_{B1}(x)$ relating the lattice constant to the composition of titanium carbide.

If titanium atoms nearest to a vacancy shift away from this vacancy (see fig. 2.2 (b)), titanium atoms forming the next sphere of the vacancy should be displaced in the opposite direction, i.e. towards the vacancy, so that the lattice constant decreases. So, a vacancy-induced field of disturbances should extend to at least two spheres of titanium atoms. In this case attenuation of disturbances with distance from the vacancy represents Friedel oscillations. As long as the concentration of vacancies is small and vacancy-induced disturbance regions in the lattice do not overlap, the lattice constant a_{B1} will increase with growing concentration of vacancies. When the disturbance regions overlap, static atomic displacements induced by neighboring vacancies are mutually compensated and the lattice constant decreases. Consequently, a maximum should be observed in the dependence $a_{B1}(x)$ for disordered TiC_x.

Thus, structural vacancies bring about static distortions of the crystal lattice. The resistance of a $B1$-type structure to the formation of structural vacancies is probably due to the fact that occupied octahedral groups CTi_6 preserve the system of titanium atom packing and resist stresses arising around a vacancy.

At the lower boundary of the homogeneity interval necessary and sufficient conditions for the loss of stability by the crystal lattice upon formation of structural vacancies have to be fulfilled. The necessary condition of stability loss reduces to the appearance of structural vacancies having the smallest admissible radius of a vacant octahedral interstitial site $R_{\square}^{min}$. The sufficient condition of stability loss is that the concentration of vacancies with the smallest size $R_{\square}^{min}$ should be sufficient for the formation of an infinite vacancy cluster in the crystal. The size $R_{\square}^{min}$ depends on the phase with which the nonstoichiometric compound is in equilibrium at the lower boundary of the homogeneity interval. TiC_x is in equilibrium with hcp α-Ti.

Octahedral interstitial sites in the structure of titanium are much smaller than the least possible size $R_{\square}^{min}$ of octahedral interstitial sites of the fcc titanium sublattice of TiC_x.

Thus, to determine the lower boundary of the homogeneity interval for TiC_x, Gusev et al. [42] suggest to find the $R_{\square}^{min}$ value and calculate the vacancy concentration $z_c = 1 - x_c$ sufficient for the formation of an infinite vacancy cluster. For titanium carbide they estimated the minimum admissible size of a vacant octahedral interstitial site to $R_{\square}^{min} = 0.059$ nm and the critical concentration of structural vacancies to $z_c = 0.462$. The lower boundary of the homogeneity interval was determined to $TiC_{0.54}$, which is in good agreement with experimental data [42, 44].

High-sensitivity diffraction techniques and, particularly, neutron diffraction revealed that under certain conditions interstitial carbon atoms may have an ordered distribution in TiC_x. These ordered phases, so-called superstructures, occur as a phase transformation at decreasing temperatures after atomic redistribution over lattice sites of the substitutional solid solution. As a result, lattice sites of the disordered solution may separate into several sublattices differing in the probabilities of their sites being filled with carbon atoms.

The ordered cubic phase Ti_2C, which is formed in titanium carbide $TiC_{0.52}$-$TiC_{0.71}$ during slow cooling from 1300 to 800 K, has double the lattice parameter as compared to the disordered carbide [46]. Its disorder-order transition temperature is about 1000 K. It was found [47] that the trigonal ordered phase (space group $R\bar{3}m$) Ti_2C is formed as a result of ordering of nonstoichiometric titanium carbide in the $TiC_{0.58}$-$TiC_{0.63}$ range, while a rhombic superstructure Ti_3C_2 (space group $C222_1$) can appear at a higher carbon concentration. A structural and electrokinetic study of disorder-order phase transformation in TiC_x ($0.5 < x < 1.0$) [48] revealed the formation of cubic (space group $Fd\bar{3}m$) and trigonal (space group $R\bar{3}m$) superstructures of Ti_2C type and of a rhombic superstructure (space group $C222_1$) Ti_3C_2. The ordered phase Ti_6C_5 with hexagonal symmetry was found in thin Ti-C films [49]. A detailed listing of ordered phases of TiC_x compounds and their location in the Ti-C phase diagram is given in [42].

Chemical bonds in TiC_x compounds were estimated using band and cluster methods, e.g. ESCA studies (electron spectroscopy for chemical analysis). A combined covalent-metallic-ionic type of chemical bond is found in TiC_x [50, 51]. This is in line with specific feature of TiC_x such as the combination of main parameters of metals (a simple structure and high thermal and electric conductivity decreasing with temperature) and covalent compounds (high hardness and low plasticity). The band structure of titanium carbide was comprehensively reviewed in [52]. Changes in the electron energy spectrum caused by the formation of vacancies in the carbon sublattice can be interpreted as the increase in the metal-metal interaction combined with diminishing of covalent and ionic components of metal-nonmetal bonds. The effect of structural vacancies on the electronic structure of titanium carbide was discussed in sufficient detail in [53, 54].

2.2 Deposition of thin films

2.2.1 Magnetron sputter deposition

Thin film production by Physical Vapor Deposition (PVD) is of high technological relevance in many industrial sectors like the production of hard and wear resistant coatings, diffusion barriers, optical films and in semiconductor applications. PVD – generally applied in vacuum – is based on the production of a vapor by physical processes and the subsequent condensation

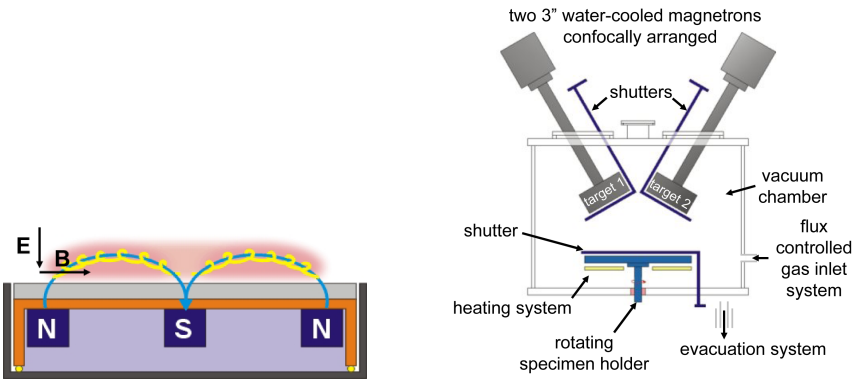

(a) (b)

Figure 2.3: (a) Schematic cross-section of a planar magnetron. Electrons are trapped in cyclic motion near the target surface, leading to a higher plasma density and therefore higher sputtering rates. (b) Scetch of a dual magnetron sputter deposition device with two confocally arranged magnetrons. Both pictures from [58].

as thin film on a substrate [55]. The two most important methods to produce a vapor are evaporation and sputtering. Whereas evaporation transfers the atoms thermally into the gas phase, in sputtering they are ejected by ion impact [56].

Sputter deposition of materials is based on the plasma-assisted production of ions (usually argon), which bombard a target, acting as cathode of the plasma discharge. As a result of ion bombardment, target atoms are ejected (*sputtered*) and deposit on the substrate, thus forming a thin film. Details of the underlying processes (*collision cascades*), leading to a sputtered surface atom can be found in [57]. Pure DC and RF sputtering, where the plasma is simply created by a DC or RF discharge, suffer from low deposition rates due to low Ar ionization in the plasma. The magnetron sputter arrangement, developed in the 1970's, is the most common one and offers higher deposition rates.

In fig. 2.3 (a) the effect of a planar magnetron setup is shown. A magnetic field is created by a set of permanent magnets, placed behind the target, providing a ring-shaped magnetic field. It is oriented parallel to the target surface and perpendicular to the electric field, which was created when plasma interacts with a surface. Electrons are concentrated with cycloidal motion above the target ("race track"). This leads to a high plasma density near the target, resulting in increased Ar ionization and enhanced ion bombardment. The magnetron configuration can be used with DC and RF discharges and leads to much higher deposition rates. Thanks to the increased plasma density, depositions can be performed at lower pressures, which increases film quality.

The sputtered atoms – mainly neutral atoms are ejected – have a broad energy distribution, that has its maximum at a few eV, approximately half the surface binding energy [59]. Influence on the film properties is possible by varying the discharge power, argon gas pressure, deposition temperature and a substrate bias voltage. Additional energy of several eV is deposited on the film surface by reflected argon ions from the cathodes, which also leads to a small amount of implanted argon in the film.

Besides reactive sputter deposition by injection of reactive gases, deposition of multiple materials simultaneously (co-deposition) is possible, too. Fig. 2.3 (b) shows the sputter ar-

rangement of a dual magnetron sputter deposition process to produce coatings consisting of two different materials. By varying the individual discharge power of both cathodes different compositional distributions can be achieved.

2.2.2 Chemical Vapor Deposition (CVD)

Chemical Vapor Deposition (CVD) is a chemical process used to produce thin films of a large variety of materials. The process involves chemical reactions of gaseous reactants (precursors) on or in the vicinity of a heated substrate surface. CVD is an atomic deposition method and can provide high-purity, high-performance solid materials with structural control at atomic or nanometer scale. Moreover, it can produce single layer, multilayer, composite, nanostructured, and functionally graded coating materials with well controlled dimension and unique structure at low processing temperatures. Furthermore, the unique feature of CVD compared to other deposition techniques, the non-line-of-sight-deposition capability, has allowed the coating of complex shape engineering components and the fabrication of nano-devices, carbon–carbon (C – C) composites and free standing shape components. The versatility of CVD has led to rapid growth and it has become one of the main processing methods for the deposition of thin films and coatings for a wide range of applications including semiconductors for micro-electronics, optoelectronics, refractory ceramic materials used for hard coatings, protection against corrosion, oxidation or as diffusion barriers [60].

In a typical CVD process, reactant gases (often diluted in a carrier gas) dissociate and/or undergo chemical reactions in a activated (heat, light, plasma) environment, followed by the formation of a stable solid product. The deposition involves homogeneous gas phase reactions, which occur in the gas phase, and/or heterogeneous chemical reactions, which occur on or in the vicinity of a heated surface leading to the formation of thin films. The deposits will diffuse along the heated substrate surface forming crystallization centres, which induce film growth. Volatile by-products are often produced and removed by gas flow through the reaction chamber.

Due to surface temperatures between 850°C and 1200°C common CVD processes are restricted to substrates with adequate temperature resistance. High surface temperatures can be prevented by providing reaction energy via particles, i.e. by using a plasma discharge. This so-called plasma assisted chemical vapor deposition (PACVD) process can be applied on temperature sensitive substrate surfaces, e.g. plastic materials [61]. Further advantages of PACVD can be found in [62].

2.3 Film and interface characterization techniques

2.3.1 Rutherford backscattering spectroscopy (RBS)

Rutherford Backscattering Spectroscopy (RBS) is a fast and well established ion beam analysis method for supplying depth sensitive compositional information in the surface near region of thin films [63–66]. A monoenergetic MeV ion beam of light atoms (typically He^+ or H^+ at 0.5 – 4 MeV) is created by an accelerator and directed to the sample surface. The particles backscatter at the nuclei of atoms in the surface near region and transfer a fraction of the energy to the target atom. The number and energy distribution of the backscattered ions are detected by an analyzer.

The energy ratio of an ion before (E_0) and after (E_1) a scattering event depends on the masses of projectile and target atom (M_1, M_2) and the scattering angle θ. It can be derived from the binary collision theory [66]:

$$\frac{E_1}{E_0} = \left[\frac{\left(M_2^2 - M_1^2 \sin^2\theta\right)^{1/2} + M_1 \cos\theta}{M_2 + M_1}\right]^2 \tag{2.1}$$

Therefore, the target element can be easily identified. The ion beam penetrates the target and scattering occurs at the outermost surface as well from deeper atoms. During traveling through matter, the projectile looses energy. This energy loss $\frac{dE}{dx}$ is called stopping power and leads to peak broadening in a RBS spectrum, which delivers the depth information. The different atomic species and their (atomic) concentrations as well as the layer thickness (more exactly the *area/density* in at $\cdot$ cm^{-2}) of the film is generally determined by fitting a theoretical spectrum to the measured data. This can be performed by programs like SIMNRA [67].

It is important to note that RBS is an absolute method, which requires no standards (except an energy calibration). It has a very high accuracy with typical uncertainities of $\pm 3\%$ for areal densities and less than 1% for stoichiometric ratios. On the other hand, the method is limited to thin films of only a few µm, and roughness can influence depth resolution. By decreasing the ion energy (e.g. 500 keV $^4He^+$) a depth resolution in the nm range can be achieved for the surface near region. Also overlapping of signals from different elements can be problematic.

2.3.2 X-ray diffraction (XRD)

Elastic scattering (*Thomson scattering*) of X-ray radiation with matter is the basis for all structural analysis by X-ray diffraction (XRD) since the wavelength of X-rays is on the length scale of interatomic distances. The radiation is scattered by electrons, which oscillate at the frequency of the incoming beam. If periodic structures are present, a diffraction experiment leads to maxima at defined scattering angles, due to constructive interference [68]. The *Bragg equation* correlates the distance d of two crystal lattice planes with the observed diffraction angle θ, when radiation of a wavelength λ is scattered at the planes [69]:

$$2d \sin\theta = n\lambda \tag{2.2}$$

Fig. 2.4 (a) illustrates that constructive interference only occurs if the phase shift $2d\,sin\theta$ between the two reflected waves is a multiple n of the wavelength.

The number, positions and intensities of the diffraction peaks (the *diffraction pattern*) are dependent on the crystal structure and can therefore be used to determine the crystallographic phase of a substance. This can be done by comparing the diffraction pattern with known crystal structures, which can be obtained from databases. The most frequently used measurement geometry is the $\theta/2\theta$ configuration (Bragg-Brentano geometry, see fig. 2.4 (b)). Here, the diffraction pattern is collected by changing the X-ray incidence angle by θ and the scattering angle by 2θ. In a diffractogram the scattered intensity is plotted as function of 2θ.

Crystal structures with preferred orientations of lattice planes are textured and do not fulfill the Bragg equation at every orientation. To determine textured crystallites by scattering of X-ray radiation the surface of a sample has to be tilted and rotated, while the 2θ angle of a certain reflex remains fixed. Thus, crystal planes, which are not parallel to the surface

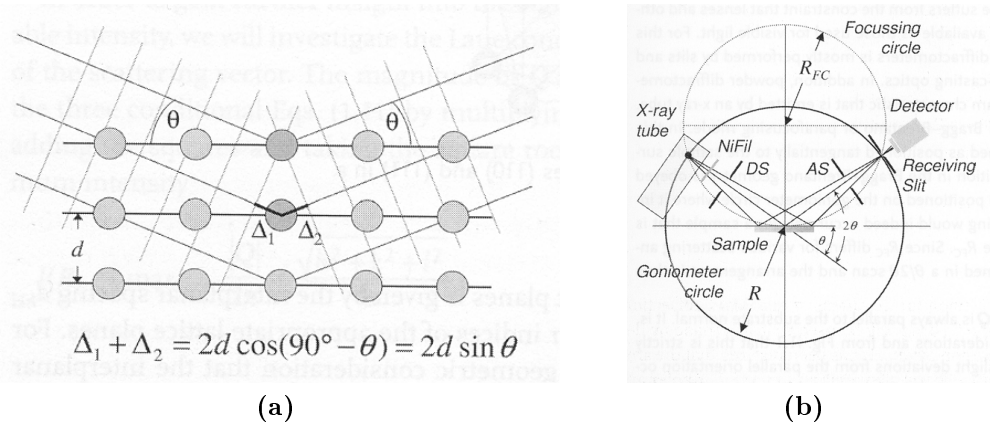

(a) **(b)**

Figure 2.4: (a) Illustration of the relation between lattice spacing d and the phase shift $2d\,sin\theta$ manifested in the Bragg equation. (b) Schematic representation of $\theta/2\theta$ diffraction in Bragg-Brentano geometry. Both pictures from [69].

can be detected. By this way, a so-called pole figure is generated, which visualizes textures, e.g. strongly oriented crystallites parallel to the surface are characterized by negligible mosaic spreading (peak broadening in a pole figure).

A very small crystallite size leads to broadening of the measured diffraction peaks. By applying the Scherrer formula the average crystallite size D can be calculated [69]:

$$D = \frac{K\,\lambda}{B_{2\theta}\,\cos\theta_B} \tag{2.3}$$

with $B_{2\theta}$ the peak FWHM (Full Width at Half Maximum), θ_B the peak position and λ the radiation wavelength (e.g. 0.154 nm for Cu K_α). Using this relation it is assumed that peak-broadening is determined by the small crystallite size only. Nevertheless, there exist several other factors, which have an impact on peak-broadening (i.e. the FWHM) as there are the crystallite shape, the shape distribution and distortions in the crystal structure like stacking faults, dislocations and microstrain. K is a dimensionless constant, which can vary between 0.89 and 1.39 depending on the crystallite shape and is dedicated to 0.94 for monodisperse (i.e. all particles have the same size), cube-shaped crystallites. Being aware of the different influences on peak-broadening and the unrealistic assumption of monodisperse crystallite distribution, size determination by the Scherrer equation should be regarded as an estimate.

2.3.3 Scanning electron microscopy (SEM)

Microscopic investigations that go beyond the information length scale of an optical microscope are performed by Scanning Electron Microscopy (SEM). This technique is widely used for studying morphology and grain topography due to its features providing high magnifications in an acceptable resolution range. SEM exhibit great options for imaging surfaces and 3D structures.

Generally, a focused electron beam (beam size 1 – 10 nm) accelerated with a voltage between 1 – 30 kV scans a electrical conductive sample surface under a vacuum pressure lower than 10^{-5} mbar. The most common imaging mode collects low-energy ($<$ 50 eV) secondary electrons (SE) that are ejected of the specimen atoms by inelastic scattering interactions with

beam electrons. At an increasing angle of incidence more secondary electrons will be emitted. Thus, steep surfaces and edges tend to be brighter than flat surfaces, which results in images with a well-defined, three-dimensional appearance. Backscattered electrons (BSE) consist of high-energy electrons originating from the electron beam, that are reflected or back-scattered out of the specimen interaction volume by elastic scattering interactions with specimen atoms. Since heavy elements (high atomic number) backscatter electrons more strongly than light elements (low atomic number), and thus appear brighter in the image, BSE are used to detect contrast between areas with different chemical compositions. Both, SE or BSE define the intensity of the corresponding pixel displayed in the image.

Energy dispersive X-ray spectroscopy (EDX) serves as an additional feature to perform qualitative and semi-quantitative chemical analysis. The number and energy of the X-rays emitted from a specimen due to electron bombardment can be measured by an energy dispersive spectrometer. As the energy of the X-rays characterizes the atomic structure of the element from which they were emitted, this allows the elemental constitution of the specimen to be measured. Detailed information of SEM principles can be found in [70].

2.4 Stress measurement in thin films

Disregarding their nature (intrinsic or thermal), internal stresses are a fundamental feature of coatings. Indeed, the global mechanical behavior of coating–substrate systems is conditioned by internal stresses, particularly concerning durability and tribological performances. For instance, internal compressive stresses often are used to increase the apparent fracture resistance and improve tribological properties. Thus, controlling the sign and amplitude of stresses in coatings has become for some times an important concern of surface engineering.

Films or coatings on a substrate are usually in a stressed state. The film "wants" to be smaller or larger than the substrate allows it to be, hence the film is in tensile stress (film "wants" to shrink) or compressive stress (film "wants" to expand). Stresses in thin films typically range from minus a few GPa to plus a few GPa. Tensile stresses are designated by a positive sign, compressive stresses by a negative sign [71]. Large stresses have to be avoided for many applications. Large tensile stresses may lead to cracking of the film. Large compressive stresses may lead to buckling [72–74].

The trivial reason for a film to be in a stressed state is deposition at a different (higher) temperature than the temperature at which the stress is measured. Due to a difference in thermal expansion coefficients between the film and substrate, the film is in a stressed state. This dependency in differential form is [75]:

$$\frac{d\sigma_{th}}{dT} = (\alpha_f - \alpha_s)\left(\frac{E_f}{1-\nu_f}\right) \tag{2.4}$$

with σ_{th} the thermal stress in the film, T the temperature, α_f the coefficient of linear thermal expansion of the film, α_s the coefficient of linear thermal expansion of the substrate, and $E_f/(1-\nu_f)$ the biaxial modulus of the film. In addition to this thermal stress, an intrinsic stress may also be observed.

Intrinsic stress in thin films is created during the film growth, depends on deposition parameters and is a result of structural disorder, i.e. of incorporated miscellaneous atoms (impurities). Further theories are specified in [56]. Sign and amplitude of intrinsic stresses of thin PVD films can be influenced by parameters, like substrate temperature, apparatus geometry, deposition

rate, energy distribution of film atoms, incorporation of miscellaneous atoms, gas pressure and bias voltage [76–78]. However, due to the plasma environment and the effect of the working gas generalizations with respect to stress are difficult to make for sputter deposited films [56].

Intrinsic stress can be measured in two ways: (1) by directly measuring the crystal lattice strain in the film using X-ray diffraction [79] and (2) by measuring the elastic deformation of the substrate. The substrate becomes curved due to the stress in the film [80–82]. When the elastic properties of the substrate are known, intrinsic stress in the film can be calculated as difference between thermal and total internal stress.

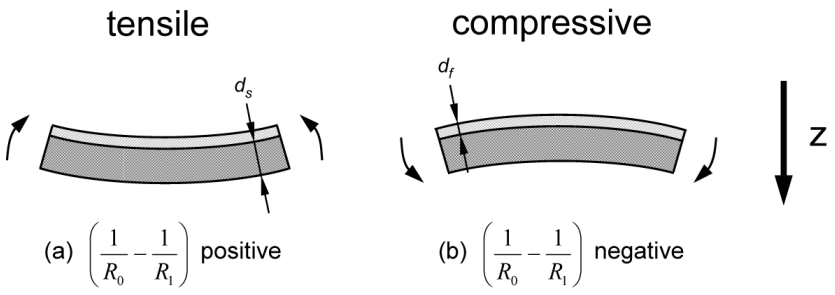

Figure 2.5: Schematic scetch of the curvature method: (a) film is in tensile stress and (b) film is in compressive stress. d_s and d_f are the thickness of the substrate and the film, respectively.

2.4.1 The curvature method

The curvature (or bending) method is a simple way to measure internal stresses in coatings. Stress in a thin film attached to a flexible substrate will induce a bending of that substrate. The curvature method involves a theoretical formula which connects the internal stress with the experimentally measured sample curvature: the Stoney formula gives the total internal stress (σ_f) in the film versus the measured sample curvature radius [80] (according to the conventions in fig. 2.5, the curvatures R_0 and R_1 are positive if the concave side is oriented towards positive z and vice versa):

$$\sigma_f = \frac{1}{6}\left[\frac{E_s}{1-\nu_s}\right]\frac{d_s^2}{d_f}\left(\frac{1}{R_0}-\frac{1}{R_1}\right) \tag{2.5}$$

In this equation, E_s and ν_s are Young's modulus and Poisson's ratio of the substrate, d_s and d_f the thickness of the substrate and the film. R_0 and R_1 are the experimentally determinable bending radii before and after deposition, whereas the curvature $1/R_0$ is zero in the case of a plane-parallel substrate ($R_0 \to \infty$). E_s and ν_s are averaged values. Eq. 2.5 is valid for the biaxial and rotationally symmetric stress state ($\sigma_{xx} = \sigma_{yy} = \sigma_f$; $\sigma_{xy} = \sigma_{yx} = 0$), which is applicable to the majority of the experiments. The surface of the film is stress free ($\sigma_{xz} = \sigma_{yz} = \sigma_{zz} = 0$). This simple formula results from the following basic hypotheses [71]:

1. strains and rotations are infinitesimal,
2. substrate and coating thicknesses are very small compared to the lateral dimensions of the plate and edges' effects are negligible,
3. coating thickness is small compared to substrate thickness ($d_f \ll d_s$),
4. substrate and coating are homogeneous, isotropic and linear elastic.

Since the edge effects are disregarded and the physical quantities are invariant in every plane parallel to the interface, the deformed shape is spherical. Particularly due to assumption 3 ($d_f \ll d_s$), Stoney's formula (see eq. 2.5) is simple and offers the advantage not to require knowledge of the mechanical properties of the coating. Nevertheless, the hypothesis $d_f \ll d_s$ may be responsible for important errors, as shown by different authors [83,84].

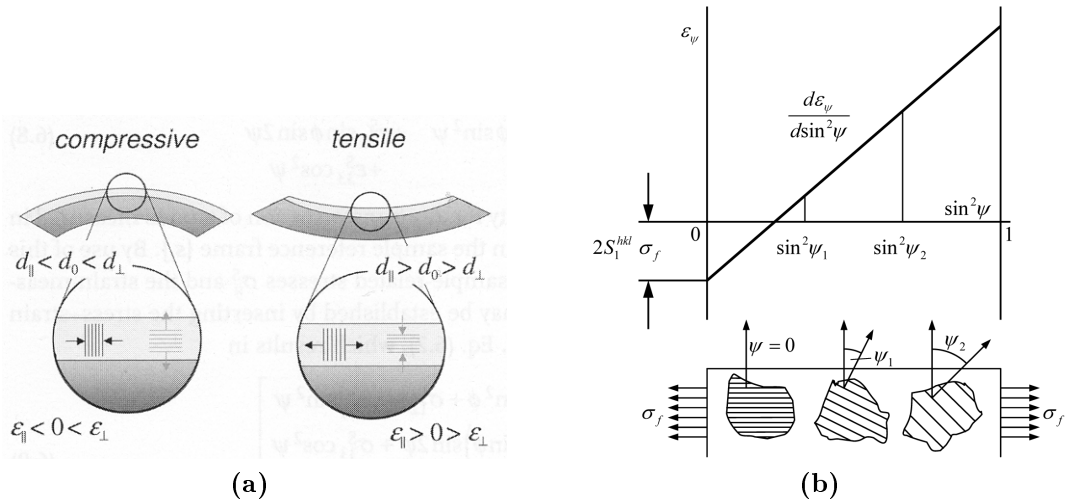

Figure 2.6: (a) Typically bended film-substrate composite with variation of the lattice spacing under compressive and tensile stress in the film plane. Taken from [69]. (b) lattice strain-$\sin^2\psi$-dependency for a biaxial rotationally symmetric stress state and orientations of stressed lattice planes for different ψ.

2.4.2 The $\sin^2\psi$ method

In elastically strained crystalline film materials, the lattice spacing depends on the strain (see fig. 2.6 (a)). In polycrystalline material, this dependence is used in the so-called "$\sin^2\psi$ method" to determine the strain in the material. For a biaxial rotationally symmetric stress state, the lattice spacing d_ψ is a function of the angle ψ between surface normal and the diffraction vector [68,79]. From d_ψ, the strain $\varepsilon(\psi)$ follows [71]:

$$\varepsilon_\psi = \frac{d_\psi - d_0}{d_0} = \left(2S_1^{hkl} + \frac{1}{2}S_2^{hkl}\,\sin^2\psi\right)\sigma_f \tag{2.6}$$

where d_0 is the strain free lattice spacing and S_1^{hkl} and $\frac{1}{2}S_2^{hkl}$ are the X-ray elastic constants (XEC) of the film material. They are defined as follows:

$$S_1^{hkl} = -\frac{\nu^{hkl}}{E^{hkl}} \tag{2.7}$$

$$\frac{1}{2}S_2^{hkl} = \frac{\nu^{hkl} + 1}{E^{hkl}} \tag{2.8}$$

The lattice spacing $d_\psi$can be determined by measuring the X-ray diffraction angles. The variation of the diffraction angle $\Delta\theta_\psi$ is essential to:

$$\Delta\theta_\psi = \theta_\psi - \theta_0 \tag{2.9}$$

when θ_0 is the stress free diffraction angle and θ_ψ the diffraction angle under stressed state. By differentiation of Bragg's equation (see eq. 2.2), the relationship between $\Delta\theta_\psi$ and the strain $\varepsilon(\psi)$ follows:

$$\varepsilon_\psi \;=\; -\cot\theta_0\,\Delta\theta_\psi \tag{2.10}$$

For accurate calculation of ε_ψ and the further use in eq. 2.6, the knowledge of the strain free lattice spacing d_0 and thus, the stress free diffraction angle θ_0 is absolutely necessary.

The XEC depend on (hkl) and on the macroscopic elastic constants. They are calculated from the single-crystal elastic constants using linear elastic models, e.g. the model of Reuss, Voigt or Hill-Neerfeld [85], taking the specific nature of a diffraction experiment into account, i.e. only those grains diffract that have the normal to the lattice plane parallel to the diffraction vector. An overview of the different elastic models is given in [86] for the case of both isotropic and textured materials. For textured materials, the XEC not only depend on (hkl) and macroscopic elastic constants, but also on the φ and ψ angles. The elaboration by taking the orientation distribution function (ODF) as a weighting factor for the crystals involved in diffraction in combination with a linear elastic model is described by [87,88]. An experimental estimation of the XEC is described in [89] and [90] and requires an application of a series of loads in the elastic range. However, this is inadequate for thin films.

By plotting the strain, $\varepsilon(\psi)$, as a function of $\sin^2\psi$ (see fig. 2.6 (b)), the total internal stress in the film, σ_f, can be determined from the slope of the straight line [89]:

$$\sigma_f \;=\; \frac{\frac{d\varepsilon_\psi}{d\sin^2\psi}}{\frac{1}{2}S_2^{hkl}} \tag{2.11}$$

Nonlinear behavior in the lattice strain-$\sin^2\psi$-dependency can be generated by:

1. steep stress gradients perpendicular to the surface (e.g. after surface treatments, like sand blasting)

2. occurrence of textures in the film material

Complexity increases when the occurrence of texture has to be considered (case 2), which may hardly be avoided in thin films stress analysis. A nonrandom distribution of crystalline orientation may cause a Bragg reflection to be observable only for a restricted range of tilt angles. A reliable regression of the measured strain distribution may thus be impossible. For low-intensity peaks the determination of the lattice strain ε_ψ might become largely erroneous or even impossible. The second handicap to X-ray stress analysis posed by texture is a more fundamental one, since a textured polycrystal is elastically anisotropic even on a macroscopic scale and cannot be modelled by assuming the crystallites to be embedded in an elastically homogeneous matrix. The calculation of the XEC's then becomes questionable or inadequate. For the evaluation of residual stress in the presence of texture some approaches have been developed for textured bulk materials and in some cases these techniques have also been applied to the investigation of thin films [69].

A common approach consists of idealizing the texture as a set of crystallite groups [91, 92]. A crystallite group is a set of crystallites with the same orientation. In the crystallite-group method, the crystallites are treated as being one crystal and the strain is measured for the intensity poles of each crystallite group separately. It is implicitly assumed that the intensities that are measured originate exclusively from crystallites that belong to the

considered crystallite group. In general, only for sharp textures can measuring directions be found for which this is an acceptable simplification. Stresses are deduced from the strains using the single-crystal elastic constants. Hauk & Vaessen [93] first introduced this method for cold-rolled steel. Flinn & Chiang [94], Quaeyhaegens et al. [95] and Gergaud et al. [96] have applied the principle of this method to thin coatings.

2.5 Wettability at high temperatures

2.5.1 Wettability

Wetting phenomena are of great technological importance for many industrial applications. Printing, painting, adhesion, lubrication, cleaning, coating, soldering, brazing and composite processing are few examples among the innumerable fields utilizing wetting phenomena [97,98]. Some applications, like joining processes, require a good wetting between a liquid and a solid substrate surface whereas some others demand poor wetting or repellency. For example, the well known "lotus effect" of plant surfaces towards water plays a vital role in self cleaning mechanism [99, 100]. The removal of contaminating particles from plant surfaces is achieved by rolling water droplets which do not stick to the surface. Using the same idea ultra or super hydrophobic surfaces have been developed which give water contact angles as high as 160° or more.

Wettability can be defined as the tendency for a liquid to spread on a solid substrate [101]. Spreading is a physical process through which the liquid wets the surface. It can be defined as the increase in the area of coverage by the liquid with respect to time on placing a drop of liquid on the surface. Fig. 2.7 (a) represents the drop at time $t = 0$ s or at the moment when the drop is placed on the substrate. The successive figures show the spreading of liquid drop at increased time periods. The continuous decrease in the contact angle and continuous increase of the base diameter as well as contact area are common features of spreading of a liquid on a solid.

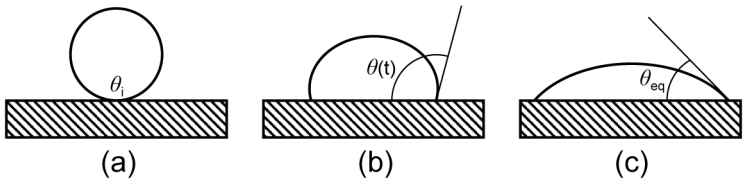

Figure 2.7: Spreading drop of liquid on a solid substrate

There are two important parameters to characterize the wettability of a liquid on a solid [102, 103]. They are:

- Degree or extent of wetting, and
- Rate of wetting.

The degree of wetting is generally indicated by the contact angle formed at the interface between solid and liquid. In the equilibrium case, it is governed by the laws of thermodynamics. It is dependent on the surface and interfacial energies involved at the solid/liquid interface. The rate of wetting indicates how fast the liquid wets the surface and spreads over it. It

is influenced by a number of factors such as the thermal conditions of the system, capillary forces, viscosity of the liquid, the chemical reactions occurring at the interface, etc.

The contact angle θ is widely used for characterizing interfacial phenomena or wetting/dewetting of solid surfaces. It is known as the angle between the tangent drawn at the triple point between the three phases (solid, liquid and vapor) and the substrate surface (see fig. 2.8 (a)). The contact angle is specific for any given system and, under equilibrium conditions, governed by the surface and interfacial energies.

On an ideal surface, i.e. a smooth surface of an inert solid the dynamic driving force for wetting ($F_{\mathrm{d}}(t)$) is given by [104]:

$$F_{\mathrm{d}}(t) = \gamma_{\mathrm{sv}} - \gamma_{\mathrm{sl}} - \gamma_{\mathrm{lv}} \cos\theta(t) \tag{2.12}$$

where γ_{ab} is the interfacial tension between the phases a and b and subscripts s, l, v indicate the solid, liquid and vapor phases respectively.

At thermodynamic equilibrium, the spreading stops and the drop has a definite contact angle. Hence, there is no driving force for spreading or $F_{\mathrm{d}} = 0$. Presuming uniformity of temperatures and chemical potentials, this condition results in Young's equation [105]:

$$\cos\theta = \frac{\gamma_{\mathrm{sv}} - \gamma_{\mathrm{sl}}}{\gamma_{\mathrm{lv}}} \tag{2.13}$$

Dupre defined the work of adhesion between solid and liquid as follows [16,106]:

$$W_{\mathrm{a}} = \gamma_{\mathrm{sv}} + \gamma_{\mathrm{lv}} - \gamma_{\mathrm{sl}} \tag{2.14}$$

Insertion of eq. 2.14 in eq. 2.13 yields to the famous Young–Dupre equation:

$$W_{\mathrm{a}} = \gamma_{\mathrm{lv}} (1 + \cos\theta) \tag{2.15}$$

For a given value of γ_{lv}, the contact angle increases as the adhesion between the liquid and solid decreases. An angle of 180° indicates zero adhesion between the liquid and surface and therefore represents a total non-wetting condition. Most frequently, it is said that the liquid wets the surface of a solid when the contact angle is less than 90°. On the other hand, if the contact angle is greater than 90°, the liquid is considered as non-wetting the solid. In such cases, the liquid drops do not have any tendency to enter into pores or holes by capillary action. It is generally accepted that the smaller the contact angle, the better the wettability. Hence, good wettability can be expected when γ_{lv} is as large as possible while γ_{sv} and γ_{sl} are as small as possible. The liquid is considered to wet the solid completely only when the contact angle is zero. This is the case when $(\gamma_{\mathrm{sv}} - \gamma_{\mathrm{sl}})$ is larger than γ_{lv}. Fig. 2.8 schematically shows a liquid drop on a solid substrate under various conditions: from complete wetting ($\theta = 0°$) to total non-wetting condition ($\theta = 180°$).

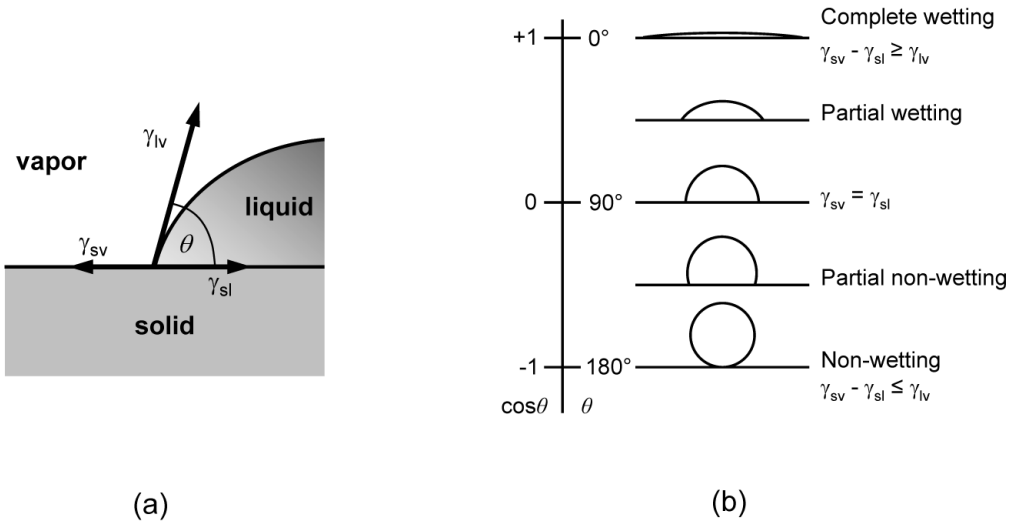

Figure 2.8: (a) Liquid drop on a solid substrate and (b) under various wetting conditions

The work of adhesion can be thought as the work that must be performed per unit area of the interface to separate the two phases. Hence, it is a degree of the bonding strength between the phases. A lower value of contact angle indicates better adhesion. For complete wetting, $\theta = 0°$, which corresponds to $W_a = 2\gamma_{lv}$, the condition for perfect wetting is given as $W_a \geq 2\gamma_{lv}$.

These derivations are made under the assumptions of spreading of a non-reactive liquid on an ideal (physically and chemically inert, smooth, homogeneous and rigid) solid. These conditions are rarely met in the practical situations. The wetting processes are affected by a number of factors such as viscosity of the fluid, roughness and heterogeneity of the surface, temperature of the fluid as well as the substrate, quantity or volume of fluid spreading, reaction between the fluid and surface of substrate, etc., which are extensively discussed in [104] and [16]. However, Young's equation is the most fundamental starting point for understanding of the complex field of wetting.

2.5.2 Reactive wetting

Wetting or spreading can be broadly classified into two categories, non-reactive wetting and reactive wetting. A liquid spreading on a substrate with no reaction or absorption of the liquid by the substrate material is known as non-reactive or inert wetting. In reactive systems, wetting frequently occurs with extensive chemical reaction and the formation of a new solid compound at the spreading liquid/reactive substrate interface. For example, during soldering on a copper substrate the process will always result in the formation of intermetallics of Sn and Cu. Similarly, in the reactive metal penetration technique of producing novel composites, a molten metal wets, penetrates and reacts with either a dense or a porous ceramic preform, converting it to a metal-ceramic composite [107]. Hence, the nature and rate of spreading is influenced by the reaction between the spreading liquid and the reactive substrate material. The quality of bonding between the constituents is determined by wettability as well as reactivity [108]. The reactive wetting is advantageous in number of cases since even a small addition of a constituent to a spreading liquid reacts with the substrate material and

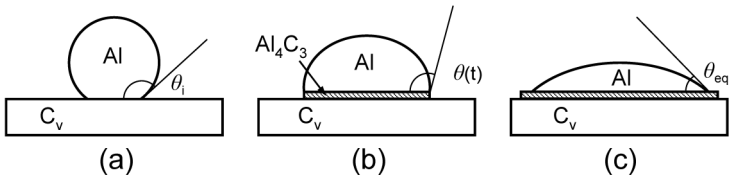

Figure 2.9: Reaction product control (RPC) model for reactive wetting (stages of reactive wetting of liquid aluminum on vitreous carbon substrate) [105, 112, 116]

causes pronounced improvement in wetting. This phenomenon is exploited in brazing and soldering [109].

Alteration of interface and formation of intermetallic compounds are the two important features of reactive wetting. Fig. 2.9 is a sketch of a liquid/substrate interface where the reactive wetting process results in the formation of an intermetallic compound. Generally, it is accompanied by material transport at the solid/liquid interface. A chemical reaction occurs between the associated surfaces and the resulting chemical bonds are responsible for wetting.

Eustathopoulos and co-workers [105, 110–115] carried out extensive work in the field of reactive wetting. They studied the wetting behavior by the sessile drop technique in a number of reactive systems that includes systems with good wetting as well as non-wetting behavior in order to analyze the mechanism of wetting. Initially it was thought that the interfacial energy change affected by the interfacial reaction could be a major cause for enhanced wetting in reactive systems [115] and hence the following equation was proposed for the smallest contact angle in a reactive system:

$$\cos\theta_{min} = \cos\theta_0 - \frac{\Delta\gamma_r}{\gamma_{lv}} - \frac{\Delta G_r}{\gamma_{lv}} \tag{2.16}$$

where γ_{lv} is the surface tension of the liquid, θ_0 is the contact angle on the substrate in the absence of any reaction, $\Delta\gamma_r$ represent the change in interfacial energy due to interfacial reaction and ΔG_r is the change in free energy per unit area released by the reaction of the material contained in the immediate vicinity of the liquid/substrate interface. However, it was found from the later experiments [111, 113] that the main effect of interfacial reaction on wetting is a change in the relevant energies of the system and not linked to the free energy change produced by the reaction. Further, it was observed that the steady state contact angle is almost the same as the contact angle obtained on the reaction product itself [105]. For example, the steady state contact angle in the reactive CuSi/vitreous carbon (C_v) system is nearly equal to the contact angle of the alloy on SiC. The observation is similar for the wetting of Cu–Cr alloy on C_v substrate.

On the basis of this observation, Eustathopoulos [116] proposed a reaction product control (RPC) model to explain the reactive wetting behavior (see fig. 2.9). According to this model, the final degree of wetting and the spreading kinetics are controlled by the new compound formed at the interface and not by the parent base metal. The initial contact angle obtained in a reactive system is the contact angle on the unreacted substrate (see fig. 2.9 (a)). After a transient stage, a quasi-steady configuration is established at the triple line where the continuation of the liquid's reaction is hindered by the presence of a non-wettable substrate in front of the triple line (see fig. 2.9 (b)). Hence, the only way to move ahead is by lateral growth of the wettable reaction product layer until the dynamic contact angle becomes equal to the equilibrium contact angle for the liquid on the reaction product. Then, due to bulk

diffusion processes the lateral extension of the reaction product goes over the triple line (see fig. 2.9 (c)).

A wide range of processes such as diffusion and chemical reaction and their possible combinations affect not only the extent of wetting but also the wetting rate. In real reactive systems, one function can hardly describe the full range of the kinetic behavior which actually results from different phenomena. Hence, different rate laws should be expected for kinetics of reactive wetting depending on the controlling processes. Reactive wetting and spreading with solidification in various systems have been studied, analyzed and modeled by various researchers and was reviewed in [104].

Five stages are identified in a reactive wetting: (i) an initial rapid spreading stage, (ii) a quasi equilibrium stage, (iii) an interfacial front advancing stage, (iv) no advancing but continuous decrease in drop height stage and (v) a final wetting equilibrium stage. The rapid spreading stage is similar to the non-reactive wetting and can generally be explained by Young's equation. However, no theoretical models are developed to describe complete reactive wetting phenomena. Only empirical relations are used in which best fit equations are suggested for the experimental results.

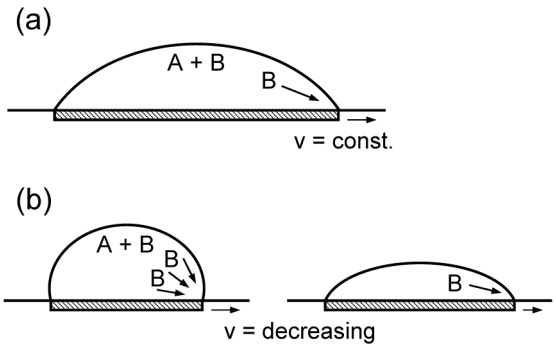

Figure 2.10: Reaction controlled reactive wetting (a) and diffusion controlled reactive wetting (b)

The spreading kinetics of reactive wetting has two limiting cases [16, 110, 117], depending on the time for the reaction at the triple line and the diffusion of reactant from the bulk drop to the triple line:

- Reaction limited reactive wetting (see fig. 2.10 (a)) and
- Diffusion limited reactive wetting (see fig. 2.10 (b))

In the first case diffusion is comparatively fast so the triple line chemistry is rate limiting resulting in a constant triple line velocity. In the second case the local reaction rates are comparatively high and the reaction is limited through the diffusive supply of reactants from the bulk drop to the triple line. The decreasing contact angle during the experiment leads to a decreasing diffusion field, so a time dependent triple line velocity is expected.

2.5.3 The sessile drop method

Various methods for measuring the contact angle have been developed over the years to evaluate wettability of a solid by a liquid. Among these, the sessile drop method is a versatile and popular technique and provides reliable data. It is used by a large number of re-

searchers [37,102,105,118] since it simulates the actual conditions in many applications. However, a large scatter is found in the data reported in the literature and these inconsistencies in the wetting behavior can be attributed to the purity of the atmosphere and the physical conditions of the wetting system employed during the experiments [119].

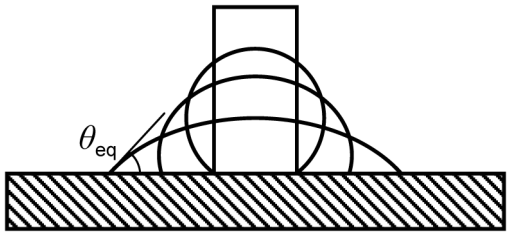

Figure 2.11: Schematic illustration of the contact angle measurement using the sessile drop method: a solid cylinder melts to form a sessile drop, which then spreads over the substrate, displaying transient contact angles to achieve a final equilibrium contact angle θ_{eq}

In this test, a known quantity of liquid is placed on the substrate and allowed to spread. The images of a spreading sessile drop are captured and processed (see fig. 2.11). Contact angles are measured by fitting a mathematical expression to the shape of the drop and then calculating the slope of the tangent to the drop at the solid–liquid–vapor interface [120]. The principal assumptions in drop shape analysis are:

- The drop is symmetric about a central vertical axis.
- The drop is not in motion. Then, only interfacial tension and gravity are the forces shaping the drop.

The radius of the spreading area, the height of the drop from the substrate surface, etc. can also be used to evaluate wettability [16]. The radius of the spreading area, contact angle and drop height are geometrically related for any axisymmetric drop and one parameter may be calculated if the other two are known.

3 Experimental details

3.1 Materials

3.1.1 Carbon fiber reinforced carbon matrix composite (CFC)

Because of their excellent properties, such as high thermal conductivity, high thermal shock and thermal fatigue resistance, the carbon fiber reinforced carbon matrix composites (CFCs) are considered as one of the armor materials for the ITER divertor [121]. One of the reference European materials for ITER applications is SEPCARB R NB31, a three-directional (3D) CFC material produced by by the French company SNECMA Propulsion Solide, consisting of ex–pitch (x), ex–PAN (y) and needled fibers (z, ex–PAN). This composite material is also proposed for the use as the plasma facing material of the high heat flux components of WENDELSTEIN 7-X [122].

NB31 uses high modulus pitch fibers, carbon fibers with high Young's modulus and very high conductivity made from pitch, that are expensive and difficult to handle, making this composite costly with a long delivery time. The 3D structure is densified with pyrocarbon through a chemical vapor infiltration (CVI) process. The densified material is submitted to heat treatment in order to make it highly conductive. The NB31 material has a high conductivity in the x-direction, high density and good mechanical strength characteristics [13, 123]. All NB31 specimens used in this work were taken from the same manufacturing batch.

3.1.2 Copper-alloys for brazing

In this work commercial brazing alloys produced by the German company WESGO Ceramics were used for CFC/Cu and Cu/CuCrZr braze joints: copper titanium alloy Copper-ABA® (copper with 2.8 *at.*% titanium, 6.3 *at.*% silicon and 4.4 *at.*% aluminum) and copper alloy Gemco® (copper with 10.7 *at.*% germanium and 0.3 *at.*% nickel). The melting temperatures are 1024°C and 975°C, respectively. Physical and mechanical properties of these brazing alloys can be found in [124, 125]. Copper-ABA is an important active brazing alloy mainly used for ceramic material joining.

3.1.3 Other materials

Thin TiC_x coatings were deposited on different substrates in order to analyze their properties by different characterization methods: pyrolytic graphite (polished, grade HPG, parallel orientation of the graphitic layers with 20° mosaic spread, ∼1 mm thickness, Union Carbide, USA) and SiO_2 quartz glass (polished, amorphous isotropic material, 20 mm diameter, 1 mm thickness, commercial name: 'Silux', GVB, Germany).

Oxygen free copper (Cu ≥ 99.95%, No. 2.0040) and the precipitation hardened copper alloy CuCrZr [26] (ELMEDUR X, Thyssen Duro Metall, Germany) were used for manufacturing CFC/Cu and CFC/Cu/CuCrZr braze joints in order to perform thermomechanical tests.

3.2 Deposition process and film/interface characterization

3.2.1 Sample preparation and deposition

Pyrolytic graphite and quartz glass substrates were ultrasonic cleaned in isopropanol and CFC NB31 in de-ionized water for 10 min. Additionally, CFC NB31 samples were heated at 300°C for 5 hours in order to outgas the samples and to fully evaporate the solvent in the CFC pores.

The TiC_x coatings were produced by dual magnetron sputter deposition (Discovery 18, Denton Vacuum) using argon (99.999%) as sputtering gas. A schematic scetch of the apparatus is given in fig. 2.3. A titanium target (99.6%) was installed at cathode 1 and operated in DC mode. A graphite target (99.999%) was sputtered in RF mode at cathode 2. Both targets were confocally arranged and include shutters to inhibit deposition. The distance between targets and substrate holder is fixed at ∼12 cm. Before deposition, the substrates were sputtered by an argon plasma for 2 min (100 W, 550-600 V bias) to remove the oxide layer and adsorbed species. Subsequently, the sputter targets were cleaned by operation with closed shutters for 2 min (∼400 V). All depositions were performed without external heating. The sample temperature did not exceed 100°C during film deposition. A substrate bias voltage was not applied and the substrate holder was rotating at 10 rpm during deposition. Due to the substrate holder rotation a widely homogeneous film thickness with variations of only 5% could be achieved. The deposition chamber was pumped by a turbo molecular pump, by means of a liquid nitrogen trap a base pressure of $\sim 5 \cdot 10^{-7}$ mbar was achieved. During sputter deposition 20 sccm argon lead to a pressure of $\sim 5 \cdot 10^{-3}$ mbar, 80 sccm to $\sim 15 \cdot 10^{-3}$ mbar. The film thickness varied between 450 nm and 600 nm and was measured by a profilometer (Veeco Dektak 8) on a glass sample on which a line of ink was drawn before deposition. The line of ink inhibited adhesion of the film on the glass sample so that the layer could be removed, generating a step, on which the film thickness could be measured.

In addition, TiC coatings were produced by Chemical Vapor Deposition (CVD), performed at Archer Technicoat, High Wycombe, UK. The deposition was done at atmospheric pressure in a stainless steel rotating chamber at 935°C using a $TiCl_4/CH_4/H_2$ mix for 3 hours.

3.2.2 Film composition (RBS)

Depth sensitive compositional analyses on TiC_x coated pyrolytic graphite samples were carried out by Rutherford Backscattering Spectroscopy (RBS) at the IPP tandem accelerator, which provides energetic ion beams. The measurements were performed in the RKS analyzing chamber. A beam of 4 MeV $^4He^+$was used to determine the elemental composition of the TiC_x films with a depth resolution of ∼1 µm. The spot size was about 1x1 mm^2 and a charge of 40 µC was accumulated for a spectrum. The scattering angle was 165°. Measurements on different positions of the sample revealed good lateral homogeneity. The spectra were simulated using the program SIMNRA 6.04 [67]. Hence, the film composition could be determined in *at.%*.

3.2.3 Crystal structures (XRD)

The crystallographic phase, textures and size of crystallites formed in magnetron sputter deposited TiC_xfilms were determined by X-ray diffraction (XRD). The diffractometer (Seifert XRD 3003 PTS) was operated with Cu K_α radiation (wavelength 0.154 nm). The experimental setup was optimized to achieve high resolution measurements. A parabolic multilayer mirror

(W/Si) was used on the primary side to achieve a parallel beam and almost complete K_β suppression. Therefore, no Rachinger correction [126] was applied on acquired spectra. On the secondary side, a parallel plate collimator – orientated perpendicular to the scattering plane – was installed to prevent detection of non-parallel beam intensity. Spectra were acquired in a $\theta/2\theta$-scan on TiC_x films coated on amorphous quartz glass in order to avoid the adoption of texture properties. Interplanar spacings were estimated by the Bragg equation, see eq. 2.2 of section 2.3.2. Annealed films were measured on pyrolytic graphite samples before and after the heat treatment. Contributions from the sample holder were excluded using an amorphous plexiglass sample holder.

The Scherrer formula (see eq. 2.3 of section 2.3.2) was used with a pre-factor of 0.94 to estimate the crystallite size. Determination of the FWHM (Full Width at Half Maximum) was done by fitting PearsonVII [127] profiles to the diffraction peaks using the program fityk (version 0.8.6, [128]). The background of each spectrum was adjusted by eye and removed before fitting. All PearsonVII variables were free fit parameters, fityk provided standard deviations. It is assumed that peak broadening is dominated by the crystallite size and not by the micro-stress of a distorted lattice. The influence of the diffractometer setup on peak broadening ($FWHM_{setup}$) was considered by removing its contribution from the FWHM using the relation:

$$FWHM_{ex}^2 = FWHM_{setup}^2 + FWHM^2 \tag{3.1}$$

with $FWHM_{ex}$ as full width at half maximum that was measured experimentally. Both terms are linked through a Gaussian convolution. $FWHM_{setup}$ was estimated using the reflexes of a $\theta/2\theta$-scan on coarse-grained polycrystalline Si-powder, which exhibits sharp peaks only broadened by beam divergences of the primary and secondary side that could not be eliminated.

3.2.4 Microscopy and cross-sections

An optical microscope was used for surface analysis with resolutions of up to 300 nm. For higher magnification Scanning Electron Microscopy (SEM), detecting Secondary Electrons (SE) and Backscattered Electrons (BSE), served as a high resolution technique for studying the morphology and grain topography. The devices Philips XL 30 ESEM and FEI HELIOS nanolab 600 have been used with e^- beams at 5 – 30 kV. Cross-sections were produced by either the typical method in metallurgy, cutting, embedding in a modified epoxy resin and polishing of the cross-section surface or by sputtering using a 30 keV Focussed gallium-Ion Beam (FIB) of the HELIOS nanolab 600 device. The latter method has the advantage that compared to the typical method smooth cross-section surfaces without artefacts (scratches of the polishing paper; shadow effects at inhomogeneous interfaces; polishing paste remains in pores and comes out during observation) can be achieved. The gallium-ion beam cuts a cavity following by a subsequent ion beam polishing step. Artefacts generated by the surface roughness ('curtaining' effect [129,130]; typical phenomenon during FIB preparation that has the same shape like a curtain) could be eliminated by the former deposition of a homogeneous and smooth carbon protection layer. The carbon film was produced inside the FIB chamber using molecules of a precursor gas and cracking them by either the electron or the gallium-ion beam. The curtaining effect induced by pores could not be avoided. It has to be noticed that the ion beam and the electron beam are arranged at an angle of 38° to each other. Therefore,

the surface of the sample has an angle of 52° to the electron beam and a correction factor is needed while measuring distances on SEM images in the direction of the tilt. Additionally, lamellae were produced by the FIB fixed on a copper grid and thinned to 250 nm in order to perform Scanning Transmission Electron Microscopy (STEM) analysis. Energy dispersive X-ray spectroscopy (EDX) was used for qualitative chemical analysis (Oxford INCA Energy software).

3.3 Film stress investigations

To evaluate the intrinsic stress of magnetron sputtered TiC_x films the curvature method and the $\sin^2\psi$ method were applied on coated planar SiO_2 quartz glass substrates. These isotropic and amorphous substrates enable comparable measurements in more than one direction, inhibit propagation of textures due to the substrate and allow calculations assuming a biaxial rotationally symmetric stress state. Thermal stress created during deposition was calculated using eq. 2.4. The substrate temperature generated by impinging energetic target particles during the deposition process was measured by thermocouples near the substrate holder.

The material properties of quartz glass are: Young's modulus 73 GPa, Poisson's ratio 0.17, coefficient of thermal expansion $0.58 \cdot 10^{-6}$ K^{-1} [131]. A well established way to determine the Young's modulus of thin films is measuring by nano-indentation [132]. However, due to their hard and brittle materials properties this method cannot be applied on thin ceramic coatings, e.g. metal-carbides or metal-oxides. These expectations have been confirmed by nano-indentation measurements at $\sim$ 500 nm thin TiC_x films using the device nano test 600. The TiC_x coatings cracked due to the indentation of the diamond tip. Thus, elastic and thermal expansion properties for TiC_x coatings as function of x were collected in an extensive literature search. Data of pure titanium [133–139] and $TiC_{0<x\leq 1}$ [31, 140, 141] were fitted linearly (see fig. 3.1).

In order to determine intrinsic stress by the curvature method the surface profiles of quartz glass substrates were measured by a profilometer (Veeco Dektak 8) in two perpendicular directions before and after TiC_x deposition. The profiles were fitted by the approximation to a segment of a circle. Then, the curvature radii could be evaluated, respectively. The total stress was calculated by the Stoney formula (see eq. 2.5 of section 2.4.1).

X-ray diffraction peaks indexed as hcp Ti (0 0 2) and fcc TiC (1 1 1) (see fig. 4.4 of section 4.1) were used for intrinsic stress measurements of TiC_x films by the classical $\sin^2\psi$ method. Measurements were performed with at least ten 2θ-signals per peak, in four orientations of the sample (φ = 0°, 30°, 60° and 90°; φ is the angle of rotation) and at tilting angles ψ from -70° to 70° in a step width of 10°. On the primary side of the experimental setup a Ni filter and a 2 mm beam-focus collimator were used in order to guarantee focused measuring at varying tilting angles ψ. Due to the diminished intensity a parallel plate collimator without apertures was assembled on the secondary side. Stress-free values (θ_0) of the employed reflexes could not be evaluated from literature or experimental methods, like Trefilov et al. [90] did, as they determined the X-ray elastic constants with different applied load levels. A similar performance with thin TiC_x films was not possible. Thus, approximated values for θ_0 as a function of x were estimated from the interpolation of interplanar spacings shown in fig. 4.5 (a) and using the Bragg equation 2.2. These data were measured at the tilting angle ψ =0°. Deviations from the real θ_0 values are almost marginal ($< 1\%$), e.g. comparing $2\theta_{x=1,measured} = 35.84°$ with $2\theta_{x=1} = 35.91°$ from [142].

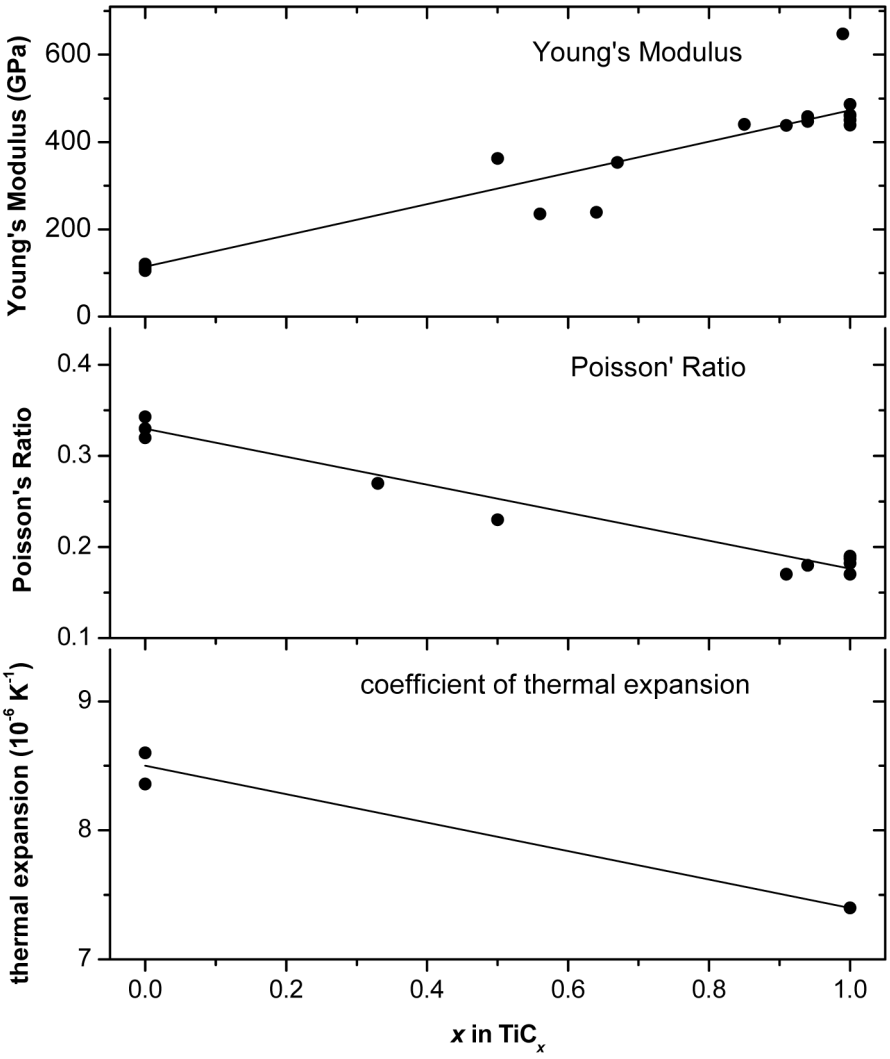

Figure 3.1: averaged values of elastic and thermal properties of TiC_x; data from [31,133–141]

The evaluation of the intrinsic stress was performed using a self-made software program that estimates the 2θ-peak positions by fitting double Gauss profiles (necessary for K_β correction), the $\sin^2\psi$ dependence (see fig. 3.2) and the stress values. The software calculated under the assumption of a biaxial rotationally symmetric stress state, provided standard deviations and could exclude failed fits. Linear fitting of nonlinear lattice strain-$\sin^2\psi$-dependencies, which appeared at a few TiC_x films (see fig. 3.2 (b)), was performed to simplify the $\sin^2\psi$ method.

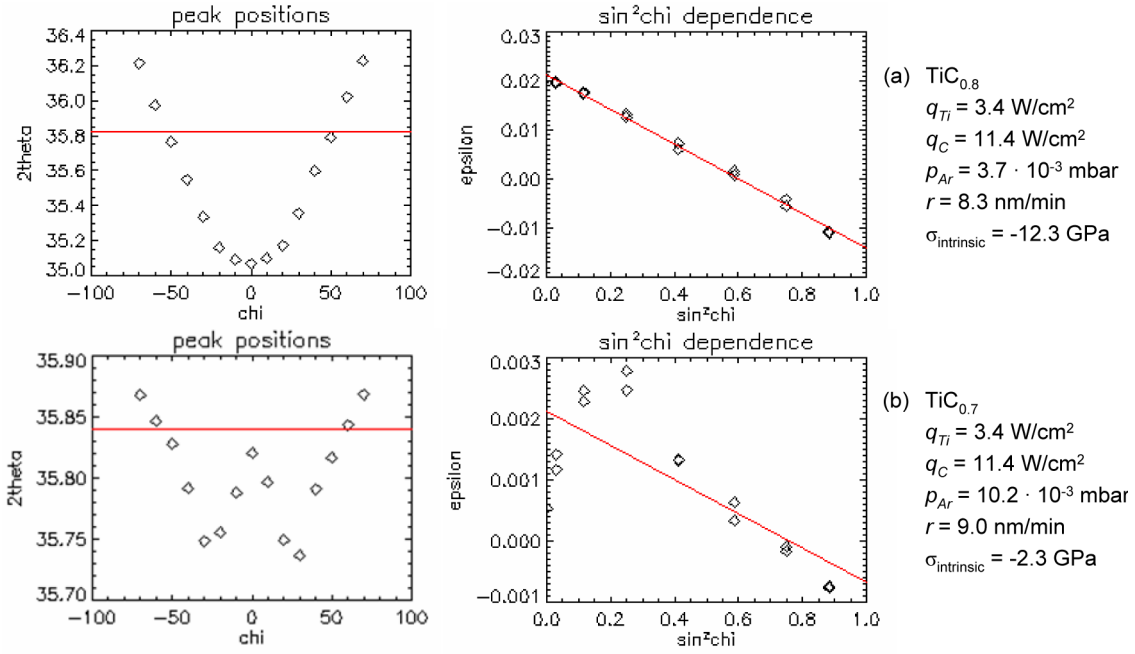

Figure 3.2: Film stress measurement by the $\sin^2\psi$ method. TiC_x films revealed, (a) linear behavior in the lattice strain-$\sin^2\psi$-dependency (red line: linear fit) with a typical V-form in the 2θ-peak position vs. tilting angle ψ diagram (red line: stress-free peak position $2\theta_0$) and (b) nonlinear behavior in the lattice strain-$\sin^2\psi$-dependency with a W-form in the 2θ-peak position vs. tilting angle ψ diagram.

3.4 Wetting experiments

Wettability is characterized by measuring the contact angle of a liquid drop on a solid substrate by means of the widely employed sessile drop method. In the sessile drop configuration, the wetting material is molten to a droplet and its curvature is imaged optically. The recorded contact angle and the shape of the droplet give evidence of the wetting behavior. This knowledge is of great technological interest, because metallic spreading is intrinsic to many industrial processes such brazing, soldering and thin-film processing. Wetting properties are also needed to describe the liquid-state processing of composites, for example, the infiltration of ceramic fiber preforms by liquid metals. A big variety of different types of sessile drop devices can be found in the literature [37, 143–148]. They all consist of different types of vacuum furnaces for heating the samples.

A high temperature sessile drop device was constructed to characterize the wetting behavior of the copper-based brazing alloys Copper-ABA and Gemco (for chemical composition see section 3.1.2) on TiC_x films. For the purpose of wetting, a main requirement of this device is to prevent the copper materials of oxidation. The formation of a copper oxide skin on the wetting materials surface is one reason that inhibits reactive wetting [16, 111, 149, 150]. The growth rate of copper oxide on pure copper follows a parabolic law and depends on two factors: (1) temperature and (2) oxygen pressure [151, 152]. Thus, an oxygen rich environment during the wetting experiments has to be avoided by either decreasing the oxygen partial pressure (vacuum conditions) or by an inert gas (e.g. argon) atmosphere [16]. In addition, the duration of the heating ramp has to be as short as possible.

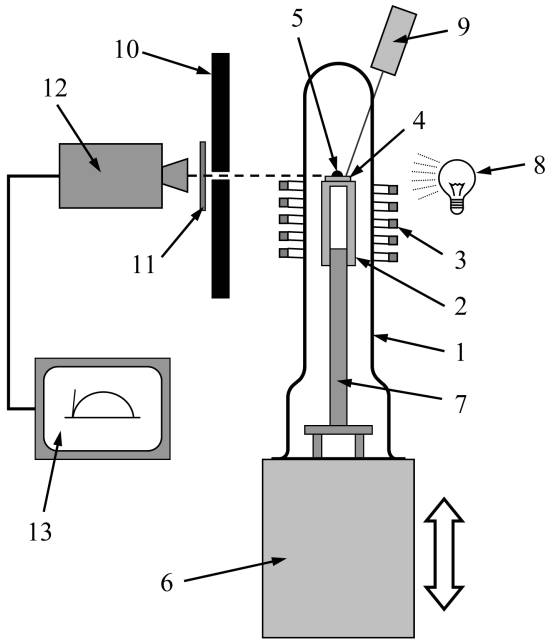

Figure 3.3: Schematic sketch of the high temperature sessile drop device: (1) vacuum glass cylinder, (2) conductive medium (graphite block), (3) water cooled solenoid coil, (4) graphite substrate, (5) metal piece for wetting, (6) movable vacuum pump system (turbomolecular and forepump), (7) Al_2O_3 holder, (8) back illumination, (9) two-color pyrometer, (10) thermal protection shield, (11) filter, (12) CCD camera with optics and (13) PC with examination software

A schematic sketch of this sessile drop experiment is shown in fig. 3.3. The device consists of a vacuum furnace using an inductive heating system. The advantage of a vacuum induction furnace is rapid heating at a low oxygen partial pressure, which minimizes the surface oxidation of the wetting materials (Copper-ABA and Gemco) during the heating ramp. The heat was applied by induction heating of a conductive medium (graphite block) in a water-cooled alternating current solenoid coil. Eddy currents are induced in the graphite block and the circulation of these currents produces extremely high temperatures. A RF generator (Hüttinger Elektronik, JG4/800S, $\backsim$50 V, 4 kW, not shown in fig. 3.3) provided an operating frequency of 0.8 MHz. The amplitude of the alternating current was adjusted manually resulting in different temperatures in the graphite block. The tube-shaped graphite block (outer diameter: 20 mm) was fixed by an Al_2O_3 holder. TiC_x coated pyrolytic graphite substrates (12 mm x 20 mm, $\sim$1 mm thick) were placed on top of the graphite block and heated as well.

For wetting on uncoated and TiC_x coated pyrolytic graphite substrates, small pieces (diameter: 1 mm, thickness: 0.7 mm) of the Gemco and the Copper-ABA alloy were used. These small pieces were cut from a 1 mm diameter wire, respectively. Acidic (55% H_3PO_4, 20% HNO_3, 25% CH_3COOH, for 1 min) and ultrasonic cleaning (2-propanol, for 5 min) contributes to minimization of the surface contamination (copper oxides formed in air). The removal of copper oxides by chemical etching (deoxidation) provides clean wetting alloys.

Wetting experiments with Copper-ABA and Gemco samples (applied on top of the TiC_x coatings) were performed in an evacuated glass cylinder, mounted with its open side on a mov-

able vacuum pump system and sealed by a rubber ring. The turbomolecular pump provides a base pressure of $8 \cdot 10^{-7}$ mbar. The vertical position of the graphite block in the solenoid coil was fixed in such a way that the surface of the pyrolytic graphite substrate is above the upper end of the solenoid coil. The position of the substrate surface was defined by the intersection point of two crossed laser beams, which provided a reproducible heating ramp at the substrate surface for all wetting experiments. The surface temperature of the TiC_x coated pyrolytic graphite samples was measured by a two-color pyrometer (IMPAC Infrared GmbH, Infratherm IGAR 12-LO, measuring range 350 – 1300°C). The calibration of the two-color pyrometer was done by adjusting the temperature at the melting point of pure copper (1085°C). Measurements over the substrate surface have shown temperature variations of only ±10°C. For wetting tests Copper-ABA and Gemco samples were heated up to ∼1030°C and ∼980°C, respectively. Fig. 3.4 shows the temperature evolution of the substrate surface of typical wetting experiments. After a heating ramp of 1 min, 99% of the final temperature was already achieved. The melting of the wetting samples (60 – 70 s after starting the heating process) could be detected as small indentations within the temperature evolution. These indentations originate from the detraction of energy during the melting process (melting enthalpy of copper: 13.05 kJ/mol [153]). They mark $t = 0$ for subsequent wettability investigations. The difference between melting and final temperature was very low (< 20°C).

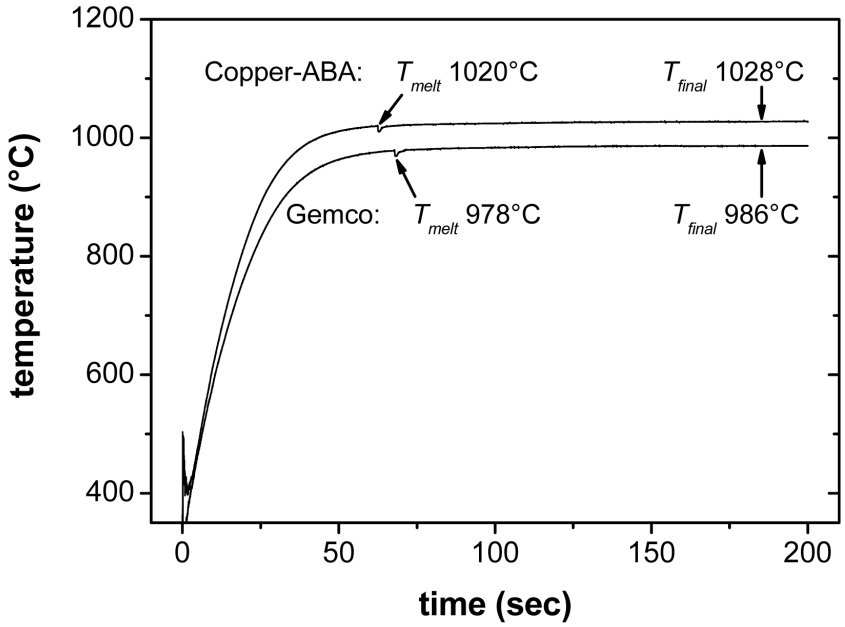

Figure 3.4: Typical temperature evolution during the wetting experiments with Copper-ABA and Gemco alloys on TiC_x coated pyrolytic graphite, performed at IPP's sessile drop device and measured by a two-color pyrometer; a small indentation of the curve represents the melting point

For the imaging of the liquid drop, a commercial CCD-camera (Skalar Microscope M2, 1 frame per second) with an additional macro zoom optic (Computar Macro Zoom Lense, MLH10XC) was used and connected to a PC in order to determine the evolution of the contact angles as a function of time θ(t). Optimal image contrast was ensured using an attenuation filter (semireflecting mirror) and a bright back illumination (500 W halogen lamp). The optical

system can be adjusted in x, y and z direction and is protected against heat by three parallel copper shields. The contact angle analysis of the images was done by a software which was developed by Dr. Hans Maier, IPP. This software detects the curvature of every droplet and calculates the tangents at the droplet edges in order to determine the contact angle θ. The droplet radius could also be detected.

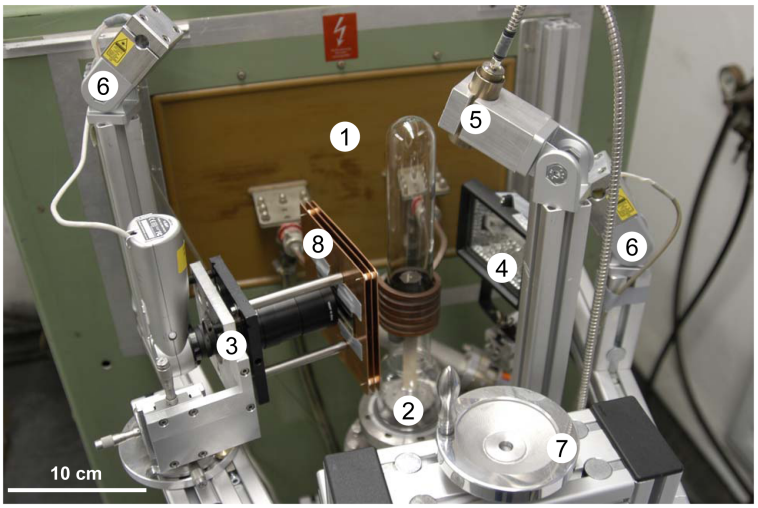

(a)

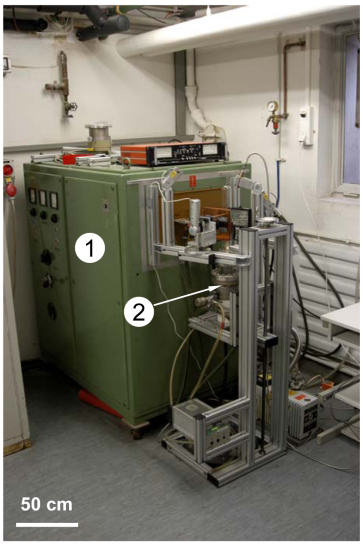

(b)

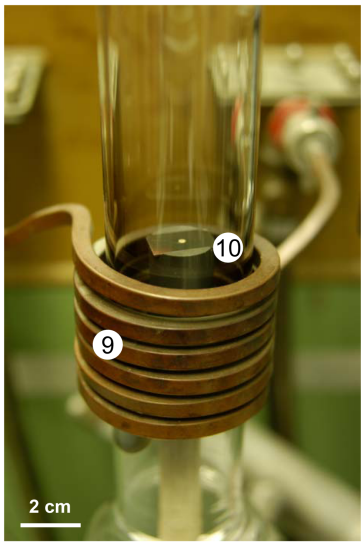

(c)

Figure 3.5: Images of the high temperature sessile drop device using a induction furnace; (1) RF generator, (2) turbomolecular pump with mounted vacuum glass cylinder, (3) optical system with CCD camera, (4) back illumination, (5) two-color pyrometer, (6) laser beams for the sample positioning, (7) crank-handle to move the vacuum pump system, (8) thermal protection shield, (9) water cooled solenoid coil, (10) heatable graphite block with wetting sample

Images of this contact angle measurement device are presented in fig. 3.5. A big advantage of this device is that the electronic supply of the heating system does not need to enter the

vacuum glass cylinder. Thus, the assembly of samples could be simplified by just moving the glass cylinder out of the induction coil. It has also the beneficial effect that the wetting samples reach their final temperature very fast. Then, surface oxidation effects of the copper-based wetting materials during the heating ramp can be neglected. With this sessile drop device, even long-term experiments (in the range of some hours) can be performed.

3.5 Brazing

Brazing of TiC_x modified CFC/Cu components was performed at the Italian company Ansaldo Ricerche in a vacuum furnace at 1035°C for 18 min. The materials used for the assemblies were CFC NB31, oxygen-free copper (Cu $\geq$ 99.95%) and the brazing alloy Copper-ABA (see section 3.1). The process pressure during the thermal treatment was measured between 2.5 – 7.0 $\cdot$ 10^{-5} mbar. The temperature was measured by thermocouples, which had contact to the surface of the specimens. The heating process and the final brazing temperature were automatically controlled according to the temperature evolution of fig. 3.6.

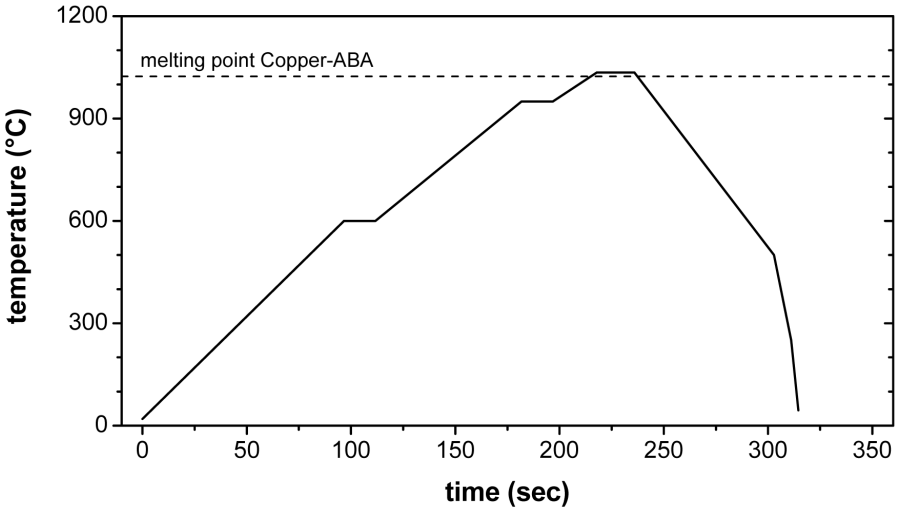

Figure 3.6: Temperature evolution vs. time during brazing of CFC to copper using Copper-ABA brazing alloy (melting point: 1024°C, dashed line)

In order not to exceed the brazing temperature at 1035°C a specified heating procedure was performed (ramp up to 600°C in 6°C/min, 15 min dwell, ramp up to 950°C in 5°C/min, 15 min dwell, ramp up to 1035°C in 4°C/min). Due to the small difference between the melting temperatures of copper ($T_{M,Cu}$ = 1084°C) and Copper-ABA ($T_{M,Copper-ABA}$ = 1024°C) it was necessary not to go far beyond the brazing temperature of 1035°C. Fast cooling was ensured by the inlet of argon gas. A thin Copper-ABA foil (thickness 50 µm) was used as brazing alloy. Before brazing, the Copper-ABA foil and oxygen-free copper were treated by acidic (55% H_3PO_4, 20% HNO_3, 25% CH_3COOH, for 1 min) and ultrasonic cleaning (2-propanol, for 5 min) in order to avoid surface contamination (copper oxides). During brazing the CFC/Copper-ABA/Cu assemblies were fixed by weights to avoid misalignments of the individual components. CFC samples were brazed to copper, so that fibers with the highest thermal conductivity (ex-pitch) are perpendicular to the brazing surface. This configuration

is based on the flat tile divertor design of future fusion machines that requires an eminent heat transfer from the plasma facing CFC to the heat sink [28,154].

3.6 CFC surface modification by O_2-plasma erosion

CFC NB31 brazing surfaces were pre-treated by oxygen plasma erosion in order to influence the adherence behavior of the CFC/Cu braze joint. The erosion of carbon in oxygen plasmas is a standard method for the cleaning of surfaces from carbon impurities [155,156] and has also been applied in nuclear fusion research [157]. The achievable erosion rates in an oxygen plasma are high compared with hydrogen plasmas. For satisfactory efficiency, high erosion rates are required. The most suitable way to achieve high erosion rates is to increase the ion energy, which can be varied by varying the substrate bias voltage [158].

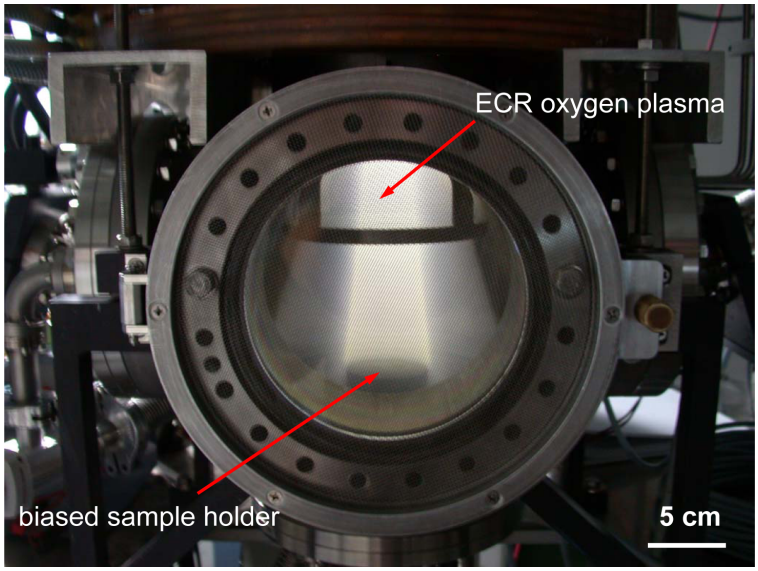

Figure 3.7: Oxygen plasma for CFC surface treatment using an electron cyclotron resonance (ECR) plasma setup (-100 V bias voltage)

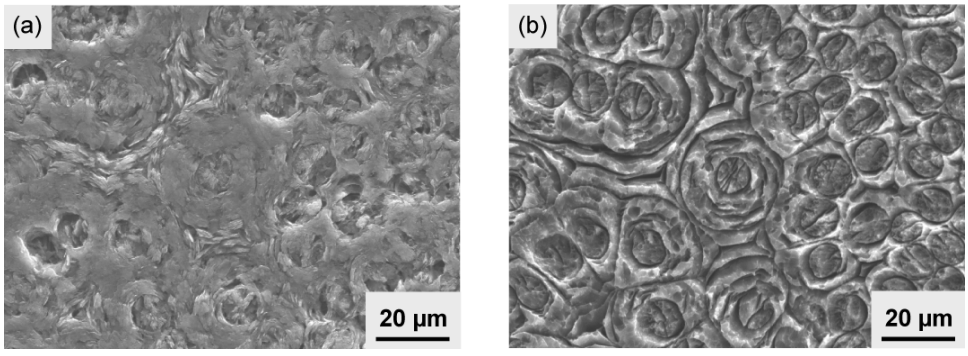

Figure 3.8: CFC NB31 surface (a) before and (b) after treatment by 20 hours oxygen plasma with a bias voltage of -100 V; the ex-pitch fibers are perpendicular to the surface

The CFC surfaces were exposed to an oxygen plasma using an electron cyclotron resonance

(ECR) plasma setup (see fig. 3.7). A detailed description of this facility is given in [159]. The vacuum base pressure was $\sim 10^{-6}$ mbar, the oxygen gas pressure during the plasma process $5 \cdot 10^{-3}$ mbar. A substrate bias voltage of -100 V induced a two-step process in which energetic ions damage the surface and predominantly neutral oxygen species react to form CO and CO_2 [158]. Hence, the oxygen plasma erosion of carbon is influenced by both, physical and chemical erosion. After 20 hours the CFC surface was 'cleaned' from carbon matrix that filled the pores during cutting. The erosion rate was determined to ~ 1 mg/h·cm^2. Primarily, the erosion of carbon occurred at the CFC fiber-matrix interface zone resulting in a high roughening of the CFC surface (see fig. 3.8).

3.7 Thermomechanical testing

3.7.1 Shear strength tests

To assess the quality of composite joints it is common to use a shear strength test. However, the stress field in the sample strongly depends on the shear test configuration. Therefore, only values obtained with the same shear test configuration and sample geometry can be compared directly [160]. In this work, samples for shear strength tests were produced by coating of different TiC_x layers (magnetron sputter deposition and CVD, thickness: 500 nm and 750 nm, respectively; see section 3.2) on both sides of 5 mm thick CFC NB31 plates (as-received and oxygen plasma treated; see section 3.6) and brazing them with two 10 mm thick oxygen-free copper pieces (see section 3.5). In that way, sandwich-like Cu/CFC/Cu components were created. Subsequently, shear strength test samples with a size of 25 mm x 5 mm x 5 mm (see fig. 3.9 (a)) were cut by electro wire-discharge machining. For shear strength testing, CFC NB31 fibers with the highest thermal conductivity (ex-pitch) are perpendicular to the brazing surfaces and to the load direction. This configuration is based on the flat tile divertor design of future fusion machines that requires an eminent heat transfer from the plasma facing CFC to the heat sink [28, 154].

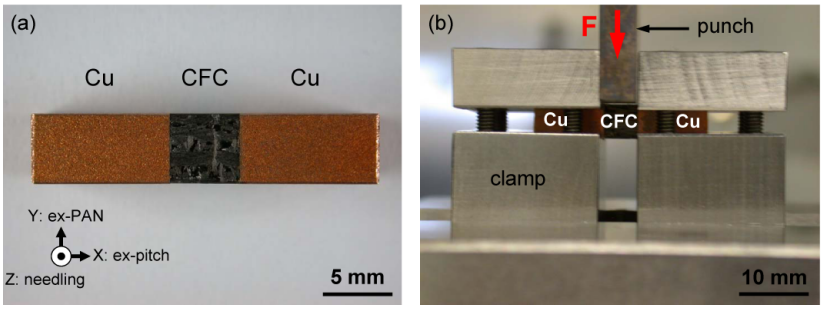

Figure 3.9: (a) Cu/CFC/Cu sample for shear strength tests; the compound was brazed by Copper-ABA at 1035°C using different TiC_x films; (b) shear strength test facility

The samples were mounted in the shear strength test apparatus illustrated in fig. 3.9 (b). Eight shear strength samples were tested for each kind of joint. The test was performed at room temperature in an universal-material-strength-test device TIRA test 2820. The shear stress at the Cu-CFC interfaces was applied using a 4.9 mm thick punch pushing from the top onto the CFC. The load direction of the CFC shear strength test samples was parallel to the ex-PAN fiber direction. The distance between clamp and CFC/Cu interface and between

punch and CFC/Cu interface was 0.05 – 0.1 mm. During the shear test the force has been recorded that is required to move the punch at a constant cross head speed of 0.01 mm/s parallel to the CFC/Cu interfaces. The maximum force F_{max} is then related to the sheared area A_{shear} =2 x 5 mm x 5 mm, which gives the shear strength σ_{shear} used for the evaluation (see eq. 3.2).

$$\sigma_{shear} = \frac{F_{max}}{A_{shear}} \tag{3.2}$$

The mechanical tests were performed at least on five samples for each kind of joint. The fracture surfaces of the shear strength tests were investigated by Scanning Electron Microscopy (SEM) with the Philips XL 30 ESEM device.

3.7.2 High heat flux tests by hydrogen beam

High heat flux (HHF) tests on TiC_x modified CFC/Cu braze joints were carried out in the hydrogen beam facility GLADIS [161] at IPP Garching using actively water-cooled CFC/Cu/-CuCrZr flat tile mock-ups. This mock-up design corresponds to the divertor design of future fusion machines (see section 1.2) that includes a 0.5 – 2 mm ductile layer of pure copper between the CFC armor tiles and the CuCrZr heat sink. In this way, residual stresses generated by a large thermal expansion mismatch can partially relax [15]. The aim was to investigate the thermal performance of the whole flat tile mock-up under fusion relevant power loads focusing on TiC_x coatings implemented at the interface between CFC NB31 and the pure copper interlayer.

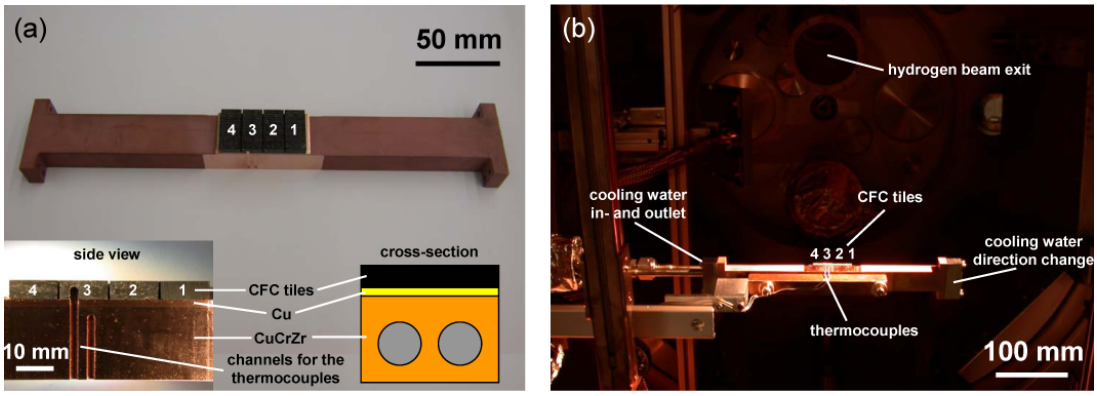

Figure 3.10: (a) TiC_x modified CFC/Cu/CuCrZr flat tile mock-up after the brazing process, (b) setup of the flat tile mock-up inside the GLADIS vacuum chamber

The flat tile mock-ups were produced by a single brazing step at the Italian company Ansaldo Ricerche (see section 3.5). The brazing alloys Copper-ABA and Gemco were used for the CFC/Cu and for the Cu/CuCrZr joints, respectively. Clean and oxygen-free brazing surfaces of the CuCrZr heat sink, the pure copper interlayer and the brazing alloys were achieved by acidic and ultrasonic cleaning. CFC NB31 tiles were treated by oxygen plasma (-100 V bias for 20 h) in order to increase the surface roughness and thus, the surface area. Then, they were coated by 500 nm of a magnetron sputter deposited $TiC_{0.9}$, $TiC_{0.2}$ or Ti film or by 750 nm of a CVD-TiC coating, respectively. A reference sample without TiC_x films was produced as well. Four 5 mm thick NB31 tiles were brazed via a 2 mm thick pure copper plate on the CuCrZr cooling structure, respectively (see fig. 3.10 (a)). The heat sink includes

two cooling tubes with a diameter of 9 mm. On the sides of each mock-up, two channels and boreholes for the thermocouples were manufactured in order to measure the temperature above the cooling channel, one inside the CFC and the other inside the CuCrZr cooling structure.

The CFC/Cu/CuCrZr flat tile mock-ups were installed perpendicular and centric to the ion beam axis in the HHF test facility GLADIS via an interlock system that allows a faster pumping. The distance between the hydrogen source and the target plane in fig. 3.10 (b) was 3 m. Four CFC tiles with a total width of 50 mm were loaded within 90 – 100% of the central power density. The beam profiles at the target position meet 2D Gaussian fit configurations and are shown in [29]. Further details about the HHF test facility GLADIS can be found in [161].

The mock-ups were connected with a cooling water supply. The cooling channels include swirl tubes to homogenize the water temperature under operation and to obtain adequate heat transfer coefficients. Pressurized water, with an inlet temperature of < 20°C, was pumped through the cooling channels with a static pressure of 9.6 bar. The cooling water flow of 0.6 l/s resulted in an axial velocity of 10 m/s.

The elements were tested in the hydrogen beam HHF test facility GLADIS in consecutive steps of power loading. At first, a screening at power densities from 2 to 15 MW/m^2 and 15 s duration was performed to determine the ultimate loading conditions and pre-test the performance of the flat tile mock-ups under heat load. Afterwards, all elements were loaded at 15 MW/m^2 for 100 cycles to characterize their fatigue behavior. Every minute the mock-ups were loaded for 10 s.

The surface temperature of the exposed mock-ups was determined by an infrared camera ($\lambda \approx 10$ µm) taking frames during each pulse and by an one- and a two-color pyrometer (temperature ranges: one-color 650°C – 2200°C and two-color 700°C – 1700°C). For the one-color pyrometer ($\lambda = 0.85 - 1.1$ µm) an emissivity of 0.8 was assumed for the CFC surface. A CCD video camera imaged the components during each pulse. The bulk temperatures of CFC and the CuCrZr cooling structure directly above one cooling channel were measured by thermocouples (temperature range limit 1800°C), which were placed 2.5 mm and 10 mm under the beam facing surface, respectively. The thermocouples were installed at each CFC tile #3 (see fig. 3.10) and in the shadow of the component to prevent them from direct contact with the beam.

The finite element model

A 2D Finite Element Analysis (FEA) was performed to pre-estimate the expected temperature at the surface and within the flat tile mock-up during high heat flux test. A mathematical model was generated that uses temperature-dependent material properties (values of specific heat, density, thermal conductivity and expansion from [13] for CFC NB31 and from [14] for Cu and CuCrZr), boundary conditions and the applied heat flux loads as input. The cross-section geometry of a CFC/Cu/CuCrZr flat tile mock-up (see fig. 3.10 (a)) was then discretized using a collection of finite elements joined by shared nodes (mesh). In the simulation step the temperatures of each finite element were determined depending on the applied heat flux on the CFC tile surface and was stored in an output file ready for post processing.

The commercial finite element suite ABAQUS [162] was used for modelling and analysis. The transient and steady-state FEA considers complex heat transfer phenomena, also occurring in the cooling tubes. Inserted swirl tapes in addition to the static pressure of 9.6 bar and the water inlet temperature of < 20°C provide the heat transfer in the forced convection

regime up to 10 MW/m^2 and in the partial sub-cooled boiling regime from 10 to 15 MW/m^2 power load at the target. In the fusion community [163–165], heat transfer processes at actively water-cooled HHF tests base upon thermo-dynamic and constitutive equations, briefly summarized in the following.

The cooling channels of the flat tile mock-ups are supplied by pressurized cooling water resulting in a high turbulent flow (Reynolds number Re = 90000 > 2300). Depending on the wall temperature, different heat transfer regimes occur in an uniformly heated tube (see fig. 3.11).

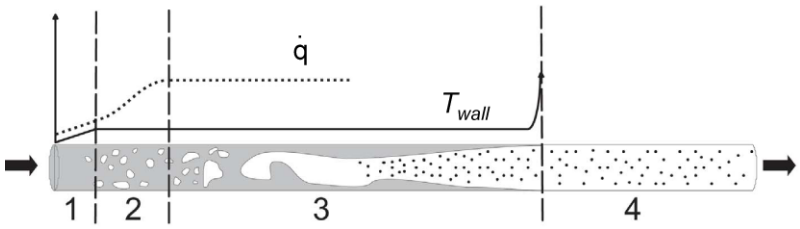

Figure 3.11: Heat transfer regimes in an uniformly heated tube (picture from [166]):
1) Single phase regime with forced convection
2) Transition region from forced convection to nucleate boiling
3) Sub-cooled boiling
4) Critical heat flux

- In the *single phase regime* ($T < 180$°C) the heat transfer is characterized by forced convection. For the turbulent flow in tubes, the heat exchange $\dot{q}$ is described by:

$$\dot{q}_{con} = \alpha \left(T_{wall} - T_{water}\right) \tag{3.3}$$

with heat exchange coefficient α:

$$\alpha = \frac{\lambda}{d} \cdot \mathrm{Nu} \tag{3.4}$$

and thermal conductivity λ, internal tube diameter d and the Nusselt number Nu. For swirl tubes, a correction factor was taken from Gambill [167]:

$$\alpha_{swirl} = \alpha_0 \cdot 2.18 \cdot y^{-0.09} \tag{3.5}$$

with $y = 2$ as number of the length per 180° twist of the tube. The short form of the Gnielinski equation for fluids [168] is an explicit function for calculating Nu used for the heat transfer eq. 3.4. It is described by:

$$\mathrm{Nu} = 0.012 \left(\mathrm{Re}^{0.87} - 280\right) \cdot \mathrm{Pr}^{0.4} \tag{3.6}$$

with Prandtl number Pr_{water} (20°C) = 6.94.

- At higher temperature ($T > 180$°C) the laws of forced convection are no longer valid due to the beginning of *partial sub-cooled boiling*, which can be mathematically described by Bergles and Rohsenow and by Thom [169]. During sub-cooled boiling, steam bubbles are formed within the liquid at the wall if the wall temperature rises above the saturation temperature of 180°C, while the bulk of the liquid is sub-cooled. The bubbles grow until

they reach a critical size, at which point they separate from the wall and are carried into the main fluid stream. Here, the bubbles collapse due to the lower temperature of the bulk fluid compared to the wall temperature. The heat transfer process in direction to the fluid is very efficient and can be calculated by the quadratic sum of convection and sub-cooled boiling by Bergles and Rohsenow (see fig. 3.12):

$$\dot{q} = \left(\dot{q}_{con}^2 + \dot{q}_{boil}^2\right)^{0.5} \tag{3.7}$$

with

$$\dot{q}_{boil} = \frac{\left(T_{wall} - T_{saturation}\right)^2}{22.65 \cdot e^{\frac{-p}{87}}} \tag{3.8}$$

with water pressure p and saturation temperature of water $T_{saturation}$. The end of the partial sub-cooled boiling (point A in fig. 3.12) is described by Engelberg-Forster and Grief [169]:

$$\dot{q}_{\mathrm{A}} = 1.4 \cdot \dot{q}_{\mathrm{B}} \tag{3.9}$$

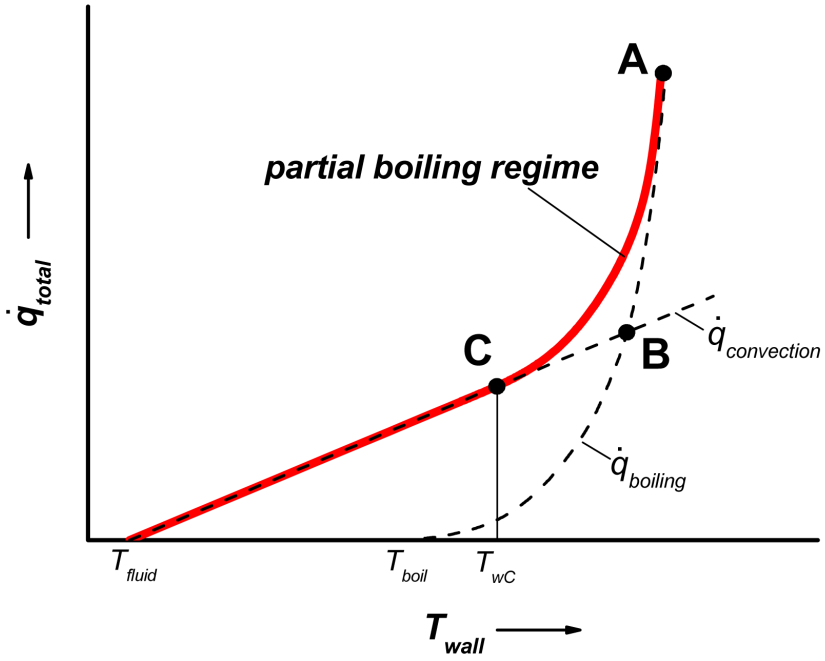

Figure 3.12: Heat transfer of convection and partial subcooled boiling

- The last heat transfer regime is the critical heat flux regime, where the wall temperature increases dramatically due to the isolation effect of the bubbles. This regime can be described by Tong's model [170, 171].

4 TiC_x films – properties and wetting characteristics

The main focus of this chapter is to evaluate the wetting behavior of thin TiC_x films as a function of the factor of nonstoichiometry x. Wettability will be determined by the well-established sessile drop method using the brazing relevant alloys Copper-ABA (Cu-Ti alloy) and Gemco (Cu alloy). Before, the TiC_x films will be characterized on their stoichiometry, crystal structure and morphology. They were produced by the dual magnetron sputter deposition technique (simultaneous sputtering at a titanium and a graphite cathode) that offers a variety of deposition parameters in order to tailor the coatings properties and to adjust a specific stoichiometry. To control the internal stress state of these films will be another important focus. In addition, titanium carbide was produced by Chemical Vapor Deposition (CVD).

4.1 Composition and TiC_x film structure

4.1.1 Compositional analysis

Magnetron sputter deposited TiC_x films Dual magnetron sputter deposition is a low temperature process that allows metastable, nonstoichiometric TiC_x films to be produced. TiC_x coatings with different stoichiometries could be achieved by varying the discharge power densities of both cathodes (C/Ti power ratio, R). Compositional analyses were carried out by Rutherford Backscattering Spectroscopy (RBS) using coated pyrolytic graphite substrates. TiC_x films were produced in the range from pure titanium to stoichiometric TiC ($0 \leq x \leq 1$). In fact, x reaches a maximum value of 1.3 that represents a slight excess of carbon in the TiC_x coating. In this work, the factor of nonstoichiometry x is the ratio of the carbon to titanium content c_C/c_{Ti}, which was determined by RBS. The composition of all TiC_x films and their factor of nonstoichiometry x as function of the C/Ti power ratio R is shown in fig. 4.1.

The elements distribution of the layers analyzed by RBS shows that among titanium and carbon the oxygen content plays a significant role, too (see fig. 4.1 (a)). In one case it even reaches a maximum of 20 *at.*% of oxygen. However, most of the TiC_x films reveal an oxygen content lower than 10 *at.*%. This is the result of a certain level of oxygen contamination during the deposition, which depends on the vacuum base pressure and the deposition rate. Experimental limitations and the extremely high reactivity of titanium with oxygen have been crucial for the observed oxygen contamination of TiC_x films. Normally, oxygen atoms form rutile, the most common natural form of TiO_2 [172], but Delplancke-Ogletree et al. [173] have reported that oxygen atoms can be incorporated in the TiC_x lattice substitutionally. According to Hägg's rule [43] for interstitial phases and compounds, a small content of oxygen atoms can replace carbon in the TiC_x lattice without altering the $B1$ structure.

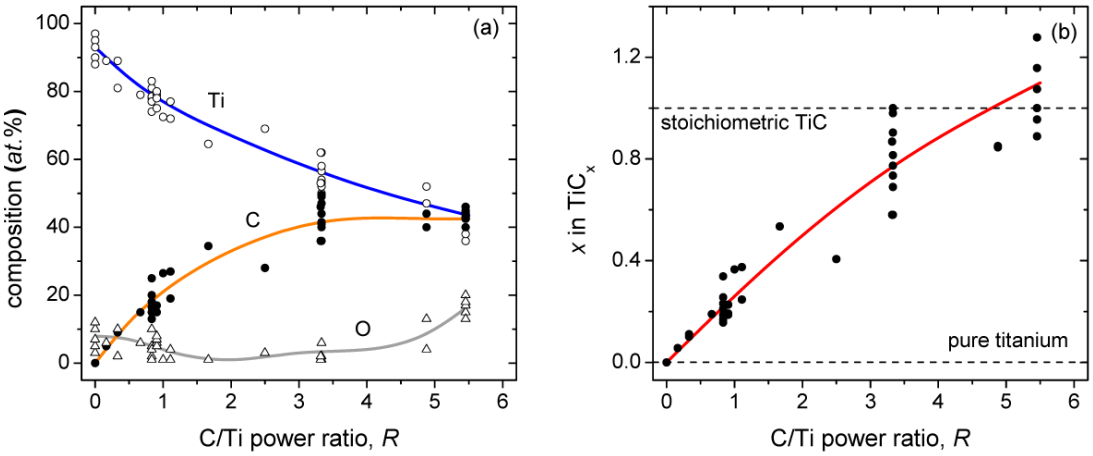

Figure 4.1: (a) composition of magnetron sputtered TiC_x coatings measured by RBS as a function of C/Ti power ratio, R; (b) dependency of the factor of nonstoichiometry x on the C/Ti power ratio, R

The graphite target has a lower sputter yield than the titanium target, because the surface binding energy of graphite is 7.41 eV (atomic weight 12 g/mol) and of titanium 4.89 eV (atomic weight 48 g/mol) [174]. Therefore, stoichiometric TiC films could not be achieved at a C/Ti power ratio of 1 (see fig. 4.1 (b)).

In literature a C/Ti power ratio of $R = 2 - 5$ is recommended to produce stoichiometric TiC films [175,176]. RBS analysis of different films coated at $R = 3.3$ show that x scatters between 0.6 and 1 (see fig. 4.1 (b)). The scatter could be caused by irregularities during the deposition due to non-constant discharge voltages, argon pressures or vacuum base pressures. In fig. 4.1 (b) the dependency of x is plotted over the C/Ti power ratio R for $0 \leq R \leq 5.5$. The factor x increases almost linear with R. TiC stoichiometry could be achieved between $3.3 \leq R \leq 5.5$. However, scattering due to the irregularities described above can be observed at any power ratio.

RBS spectra of selected TiC_x films ($TiC_{0.9}$, $TiC_{0.2}$ and Ti) are shown in fig. 4.2. These spectra were recorded after sputter deposition and after annealing at brazing conditions (see section 3.5). The thickness of these films was about 500 nm. The black curves are recorded energy spectra of backscattered $^4He^+$ ions detected at an angle of 165°. The red curves are simulated spectra assuming corresponding TiC_x layers that fit the experimental data very well. Fig. 4.3 shows the elements distribution of these films from the surface to the graphite substrate. RBS signals of as-deposited TiC_x films exhibit a homogeneous distribution of the elements and nearly no mixture with bulk carbon. With annealing at 1035°C for 18 min a carbon signal in the Ti film and an increase of the carbon signal in the $TiC_{0.2}$ layer could be observed indicating a reaction between titanium and bulk-carbon. Most likely, it formed titanium monocarbide, which has a high negative enthalpy of formation (-184 kJ/mol at $T = 1100$°C) [153] and is thermodynamically stable. From literature, it is known that transition metals like titanium react strongly with carbon to form carbides [17,177]. Inhomogeneities of these carbon signals suggest graded transition zones between film and substrate and indicate diffusion processes during the reactions. The diffusion profiles after annealing were simulated and are shown in fig. 4.3. Thicknesses were calculated using the atomic densities of solid titanium ($5.66 \cdot 10^{22}$ atoms/cm^3), carbon ($1.13 \cdot 10^{23}$ atoms/cm^3) and oxygen ($5.38 \cdot 10^{22}$ atoms/cm^3) [66]. Diffusion of carbon from the substrate into the films and dif-

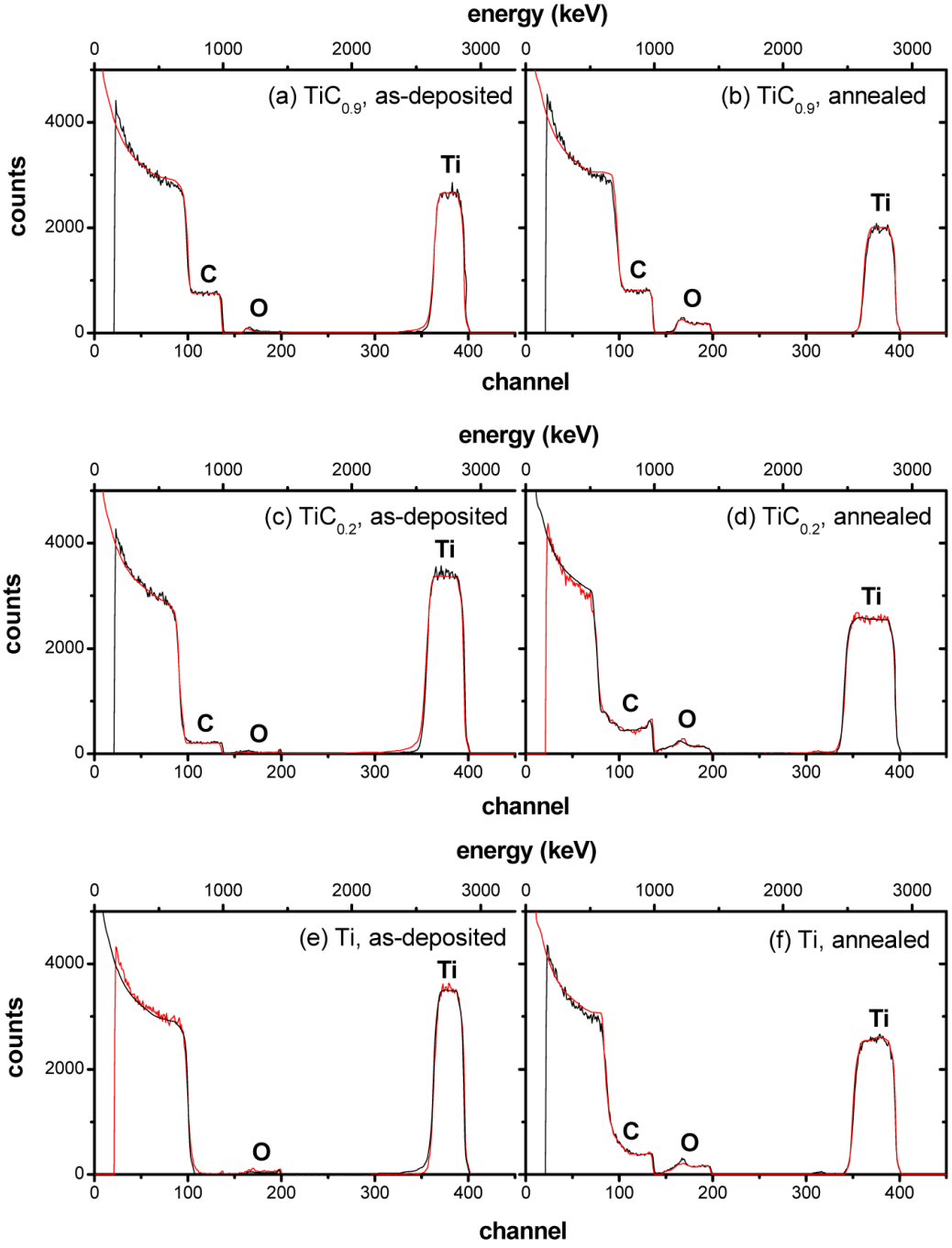

Figure 4.2: RBS spectra of as-deposited and annealed (1035°C for 18 min) magnetron sputtered TiC_x films on pyrolytic graphite, experimental (black) and simulated (red). Element labels (C, O, Ti) indicate signals of the TiC_x films, while signals below channel 100 result from the graphite substrates.

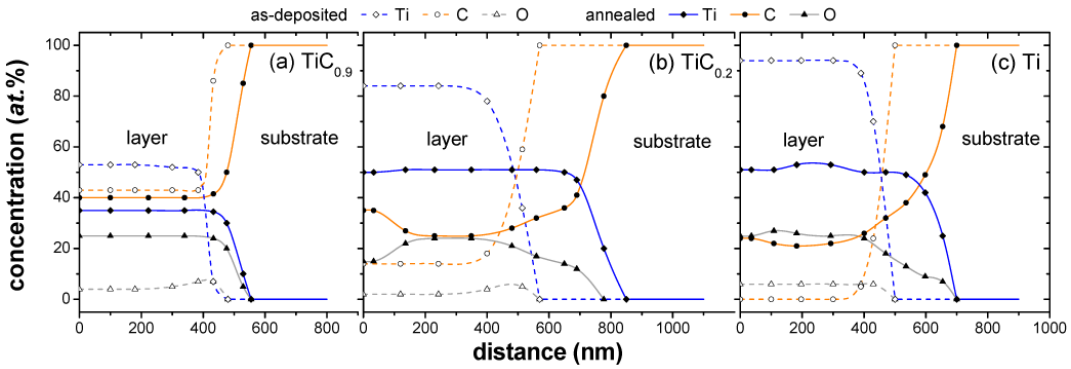

Figure 4.3: Elements distributions of (a) $TiC_{0.9}$, (b) $TiC_{0.2}$ and (c) Ti films coated on pyrolytic graphite, as-deposited (dashed) and annealed at 1035°C for 18 min (solid), determined by RBS. The x-axis is the distance to the coatings surface, respectively.

fusion of titanium into the graphite substrate are clearly visible. The $TiC_{0.9}$ film did not reveal any distinct change of the carbon signal. Thus, only little reaction occured, because the thermodynamically stable state has already existed.

After annealing each film shows a significant increase of the oxygen signal. A relatively low pressure of about $5{\cdot}10^{-5}$ mbar and the high ability of titanium to form titanium dioxide are responsible for these reactions between titanium and oxygen.

CVD-TiC films RBS measurements of CVD-coated titanium carbide films show an exact stoichiometric TiC composition $x = 1$. This stoichiometry was expected due to a sufficient amount of precursor materials and due to the high temperature of the deposition process (935°C). At this temperature, the thermodynamically stable titanium monocarbide was formed by surface diffusion processes. Thus, no nonstoichiometric (metastable) TiC_x films could be produced.

4.1.2 Crystal structure analysis

Magnetron sputter deposited TiC_x films In order to characterize their crystal structure, magnetron sputtered TiC_x films were deposited on quartz glass substrates in the range from pure titanium to stoichiometric TiC ($0 \leq x \leq 1$) and subjected to X-ray diffractometry (XRD). According to the powder diffraction files of the International Centre for Diffraction Data (ICDD) [142] stoichiometric titanium carbide TiC has two characteristic diffraction peaks at $2\theta = 35.91°$ and 41.71°. They belong to the (1 1 1) and (2 0 0) lattice planes of face-centered cubic (fcc) titanium carbide. Hexagonal closest packed (hcp) titanium (α-Ti) has peaks of the (1 0 0), (0 0 2) and (1 0 1) lattice planes at $2\theta = 35.05°$, 38.35° and 40.22°, respectively.

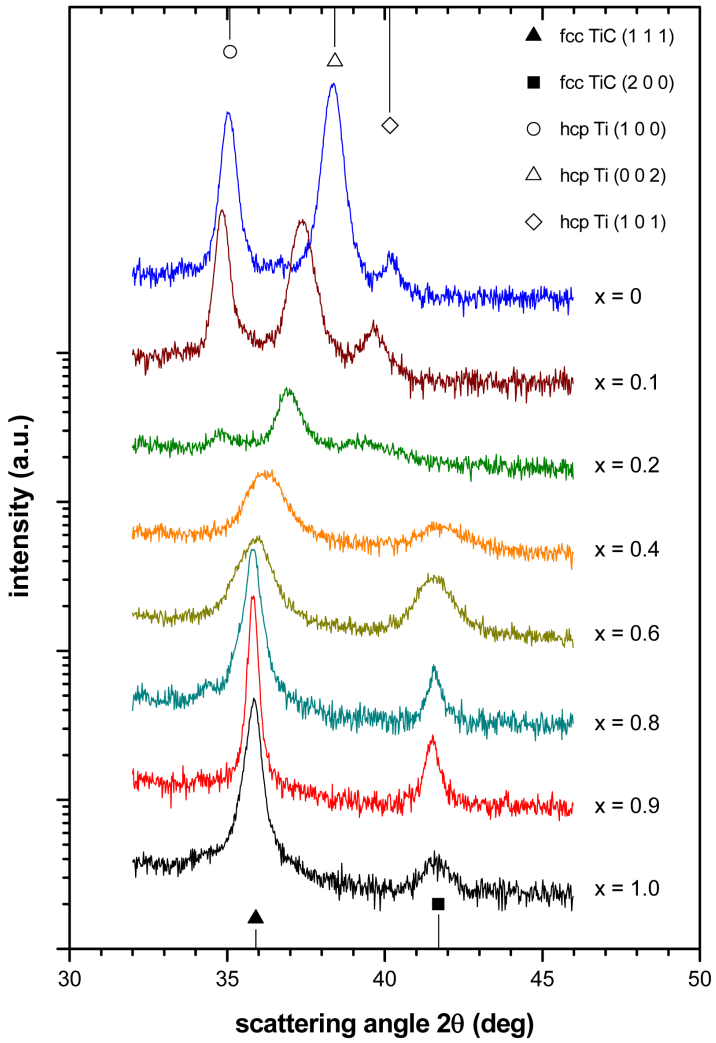

Figure 4.4: X-ray diffractogram of magnetron sputtered TiC_x films on quartz glass substrates as a function of x. The peak positions of fcc TiC (1 1 1), (2 0 0) and hcp titanium (1 0 0), (0 0 2) and (1 0 1) reflexes in the shown 2θ angle range are indicated, the powder diffraction file card numbers (ICDD database [142]) are PDF # 321383 and PDF # 441294, respectively.

Typical X-ray diffraction patterns are presented in fig. 4.4 as a function of stoichiometry. As seen in fig. 4.4, when films were deposited at $x = 0 - 0.2$ all reflection peaks can be identified by α-Ti with a hcp structure. On the other hand, when films were deposited at $x = 0.4 - 1$, all diffraction peaks can be identified by the fcc TiC phase ($B1$-type structure).

It is found that the diffraction peak at around $2\theta = 36.5° - 38°$ in fig. 4.4 tends to shift to a lower angle with increasing x. These peaks are indexed as (0 0 2) plane for hcp structure and (1 1 1) plane for $B1$-type structure, respectively. In fig. 4.5, the interplanar spacing, the peak intensity and the crystallite size measured from these peaks are plotted as a function of x. Open and closed circles indicate that the film has hcp or $B1$-type structure, respectively. As seen in fig. 4.5 (a), the interplanar spacing of the pure Ti film is a little larger than bulk Ti. Carbon atoms incorporated in the octahedral interstitial sites of the titanium lattice lead to a rapid increase of the interplanar spacing of films with hcp structure. It increases up to

0.243 nm when x increases to 0.2. When x is 0.4-1, the crystal structure changed to $B1$-type and its interplanar spacing also increases with increasing x. The interplanar spacing of the films deposited at $x = 0.6 - 1$ are nearly equal to bulk TiC. It is noted that the interplanar spacing has a weak maximum at $x = 0.9$. This maximum can be explained by vacancy-induced Friedel oscillations (see section 2.1). As seen in fig. 4.5 (b), the peak intensity has its minimum in the region of the change in crystal structure. In this region, crystallinity is less pronounced. Maxima of the peak intensity can be detected at $x = 0$ and 0.9. They correspond to undistorted hcp titanium and fcc titanium carbide crystal structures, respectively. As seen in fig. 4.5 (c), the crystallite size initially decreases with increasing x. A minimum of the crystallite size is observed at $x = 0.4 - 0.6$. When x comes to 1, the crystallite size increases rapidly and shows a local maximum at $x = 0.9$.

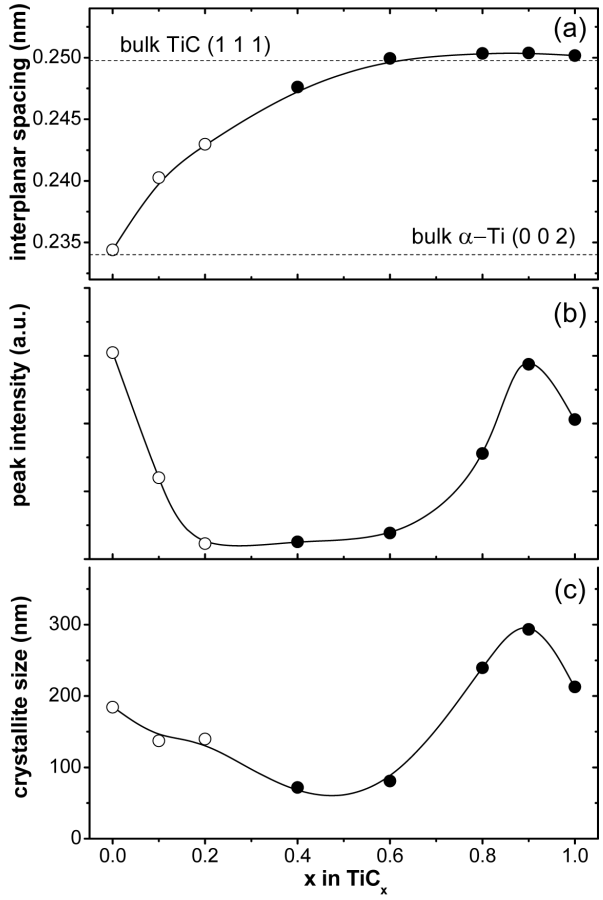

(a) Crystallite size

Figure 4.5: XRD parameter of magnetron sputtered TiC_x films using the reflexes indexed as hcp Ti (0 0 2) and fcc TiC (1 1 1): (a) interplanar spacing, (b) peak intensity, (c) crystallite size. Open and closed circles indicate that the film has hcp titanium and fcc TiC structure, respectively.

In fig. 4.6, the texture of selected TiC_x films is displayed. The pole figures of Ti, $TiC_{0.2}$ and $TiC_{0.9}$ coatings show that magnetron sputter deposition generates preferred orientations of the crystalline grains. As seen in fig. 4.6 (a), the (0 0 1) planes of hcp titanium are highly

fiber textured. Its pole figure exhibits a mosaic width of about 10°. Thus, the c-axis of hcp titanium is the preferred orientation in the direction perpendicular to the surface, hexagons are parallel to the surface. This behavior is in accordance to the columnar growth of titanium crystallites, as it is shown in fig. 4.11 (b). The increase of the carbon content decreases the degree of the c-axis preferred orientation. At face-centered cubic $TiC_{0.9}$, reflexes of the (1 1 1) planes are the preferred orientations. They are orientated not only in a single direction. These preferred orientations can be detected as circles in the pole figure at about $\psi = 10°$ and 60° (see fig. 4.6 (c)). Obviously, the (1 1 1) preferred orientation is tilted about 10° to the surface. Due to this 10° tilt and due to the reason that all (1 1 1) crystal planes of similar type include an angle of 70.5°, the reflexes at about $\psi = 60°$ have been expected. The intensities of all $TiC_{0.9}$ (1 1 1) reflexes are much lower than of the Ti (0 0 2) peak. The $TiC_{0.9}$ (1 1 1) pole figure shows fiber texture, but with a mosaic width of about 20° (measured at the $\psi = 60°$ reflexes). Thus, strongly orientated $TiC_{0.9}$ grains are less pronounced and can not be detected in fig. 4.9 (b). The texture behavior of the $TiC_{0.2}$ film is something in between pure titanium and $TiC_{0.9}$ (see fig. 4.6 (b)). A high mosaic width of about 25° and reflexes at about $\psi = 60°$, which are not clearly visible at each rotation angle φ, show that these films exhibit less-defined and distorted crystal structures with respect to the X-ray evaluation.

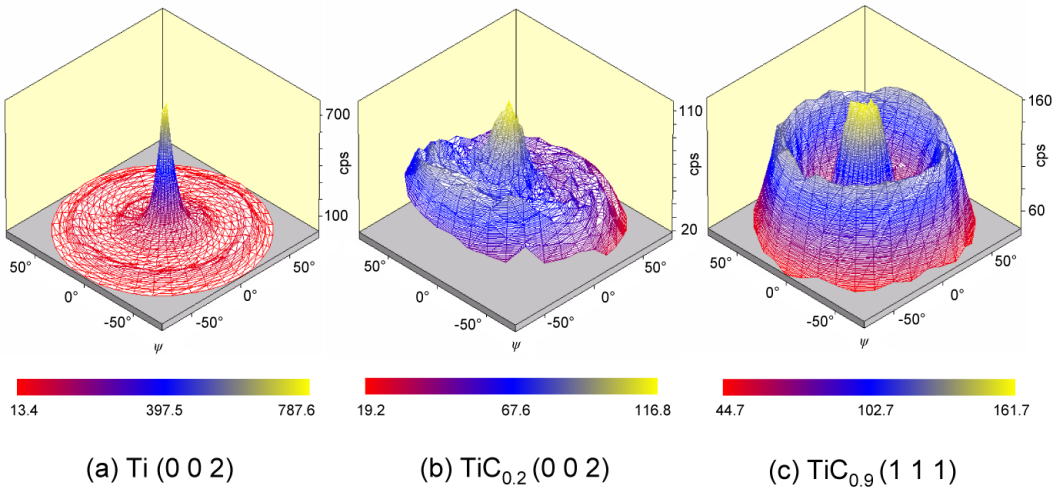

Figure 4.6: Texture analysis of selected magnetron sputtered TiC_x films: pole figures from Bragg reflections indexed as hcp Ti (0 0 2) and fcc TiC (1 1 1)

In fig. 4.7, diffraction patterns of annealed (1035°C for 18 min, red lines) $TiC_{0.9}$, $TiC_{0.2}$ and Ti films that have been coated on pyrolytic graphite substrates are compared with the as-deposited ones (black lines). The curved background originates from the carbon substrate. The $TiC_{0.9}$ film does not change its $B1$-type crystal character, while the $TiC_{0.2}$ (distorted hcp structure) and the Ti (hcp structure) film change into the $B1$-type crystal character. $TiC_{0.2}$ and Ti coatings have reacted with carbon atoms from the substrate in order to recrystallize into a new crystal constitution, which is observed to be the same than of $TiC_{0.9}$ films. Thus, $B1$-type crystallinity of $TiC_{0.9}$ is thermodynamically stable and will not change its crystal structure after any further thermal treatment. These investigations are in agreement to the RBS data shown in section 4.1.1.

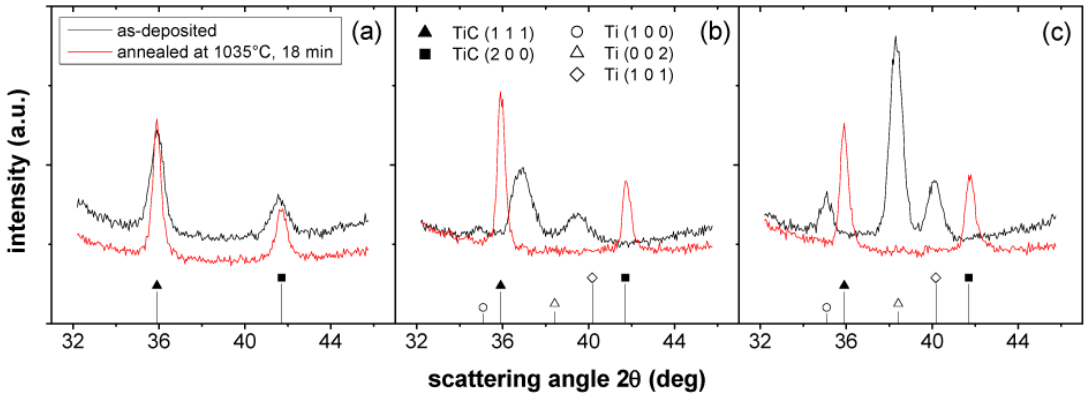

Figure 4.7: X-ray diffractograms of magnetron sputtered TiC_x films on pyrolytic graphite substrates, as-deposited (black) and annealed at 1035°C for 18 min (red): (a) $TiC_{0.9}$, (b) $TiC_{0.2}$, (c) Ti. The peak positions of fcc TiC and hcp titanium reflexes in the shown 2θ angle range are indicated, the powder diffraction file card numbers (ICDD database [142]) are PDF # 321383 and PDF # 441294, respectively.

It is summarized for magnetron sputter deposited TiC_x films that the α-Ti phase (hcp structure) and the TiC phase (fcc structure) can be produced for stoichiometries $x = 0$ and $x = 0.6 - 1$, respectively. For Ti and $TiC_{0.9}$ films, preferred orientations in the hcp (0 0 1) and in the fcc (1 1 1) direction were determined. Films in the range of $x = 0.6 - 1$ are in accordance with the homogeneity interval of the TiC_x phase, reported in the Ti-C phase diagram [44]. The maxima in fig. 4.5 at $x = 0.9$ and the annealing results of fig. 4.7 show that $TiC_{0.9}$ films exhibit a thermodynamically favored crystal structure.

In the range of $0 < x < 0.6$, hcp and $B1$-type structures were found as well, but due to the shifting of diffraction peaks to positions that deviate from bulk α-Ti and bulk TiC and due to the low intensities of these reflexes, the crystallinity can be assumed to be distorted or metastable. Hcp and $B1$-type structures were never found simultaneously within one diffractogram of a certain stoichiometry. The change of the α-Ti (0 0 2) peak into the TiC (1 1 1) peak points at the transition of the c-axis of hcp titanium into the space diagonal of fcc TiC.

As expected, ordered phases (e.g. Ti_2C or Ti_3C_2 [42]), which are formed after atomic ordering of nonstoichiometric cubic titanium carbide TiC_x were not detected.

CVD-TiC films The diffraction pattern of CVD-TiC coatings exhibits reflexes, which are exactly identified by the fcc TiC phase ($B1$-type structure). Any textures have not been detected.

4.1.3 Morphological analysis

Many of the TiC_x coatings were produced with deposition defects (e.g. buckling or delamination). Their origin and how to avoid them during magnetron sputter deposition processes will be discussed in section 4.2. In this section, sputtered coatings only without deposition defects are analyzed.

The typical grey appearance of titanium carbide [52] was observed at all magnetron sputter deposited TiC_x films (see fig. 4.8, no. 1a, 2a and 3a). It is noticeable that the color of the $TiC_{0.2}$ and Ti surfaces has changed after annealing (at 1035°C for 18 min) to bluish-gleaming and golden (see fig. 4.8, no. 2b and 3b). It is known that rutile (TiO_2) has such

possible appearances [178]. Although an increase of the oxygen content was observed (see section 4.1.1), the $TiC_{0.9}$ film did not change its color after annealing (see fig. 4.8, no. 1b). CVD-TiC surfaces are dark brown and areas of film delamination can be observed even by eye (see fig. 4.8, no. 4).

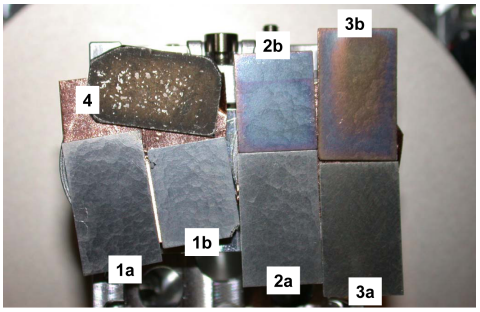

Figure 4.8: Optical appearance of thin TiC_x films deposited on pyrolytic graphite, (1a) magnetron sputtered $TiC_{0.9}$, as-deposited, (1b) magnetron sputtered $TiC_{0.9}$, annealed, (2a) magnetron sputtered $TiC_{0.2}$, as-deposited, (2b) magnetron sputtered $TiC_{0.2}$, annealed, (3a) magnetron sputtered Ti, as-deposited, (3b) magnetron sputtered Ti, annealed, (4) CVD-TiC, as-deposited

In the following, the morphology of selected magnetron sputtered TiC_x films ($TiC_{0.9}$, $TiC_{0.2}$ and Ti) and CVD-TiC, coated on both, pyrolytic graphite and CFC NB31, will be characterized by SEM. The thickness of the sputtered films was about 500 nm and of the CVD-TiC film about 750 nm.

$TiC_{0.9}$ on pyrolytic graphite The surface of sputter deposited $TiC_{0.9}$ films is slightly rippled and consists of many coherent round structures comparable to the surface of a cauliflower (see fig. 4.9 (a)). The size of these round structures ranges between 20 and 200 nm. They are the top parts of small fcc TiC grains. The cross-section of fig. 4.9 (b) shows a dense $TiC_{0.9}$ film without columnar or needle structures. After the heating process at 1035°C for 18 min cracks at the grain boundaries were formed all over the surface (see fig. 4.9 (c)). In addition, the round 'cauliflower' structures became larger in size. It seems that small grains have been connected to bigger ones. At the cross-section, no differences could be detected compared to the as-deposited one (see fig. 4.9 (d)).

Ti on pyrolytic graphite The surface of a sputter deposited titanium film is very granular (see fig. 4.11 (a)). The coating exhibits a crystalline character (α-Ti structure) that consists of tapered crystallites separated by voids. Fig. 4.11 (b) shows that these structures belong to a columnar grown titanium film. Such film growth is typical for atomic deposition processes at low-temperatures [56, 179]. The adatom surface mobility is not effective to avoid intergrain shading, which significantly affects the growth morphology. Initial nuclei tend to grow in the direction of the available coating flux and columns develop. Intergrain boundaries are voids rather than true grain boundaries, so that the titanium coating is underdense, although individual crystallites have near bulk density. Fig. 4.11 (c) shows that the Ti surface after the heat treatment has still granular, but smoother structures. Cracks through the entire film could also be observed. Titanium columns have been connected and recrystallization took place. Only some pores remained (see fig. 4.11 (d)).

$TiC_{0.2}$ on pyrolytic graphite SEM images of a sputter deposited $TiC_{0.2}$ film are shown in fig. 4.10 (a) and (b). Its structure is something between the $TiC_{0.9}$ and the Ti film. There are slight indications of a columnar film growth with nucleation points quite close to the interface (see fig. 4.10 (b)). The structures visible in fig. 4.10 (a) could be the tops of these columns. After annealing recrystallized grains with different orientations and an average size of 90 nm were observed in the entire layer (see fig. 4.10 (d)).

CVD-TiC on pyrolytic graphite Fig. 4.12 a shows the surface of a typical CVD-TiC film. On the surface, structures like 'droplets' can be observed. In between, small whiskers were detected, which is a common feature of CVD film growth [56]. The surface can be characterized by cracks over the entire film (see fig. 4.12) and by film delamination (see fig. 4.8, no. 4), indicating that high film stresses and poor adhesion may play a role during CVD-TiC deposition. Most likely, these stresses are mainly originated by the differences in thermal expansion between film and substrate, while the CVD-TiC films cool down from deposition temperature (935°C) to room temperature. In the cross-section of fig. 4.12 (b) cracks at the CVD-TiC/graphite interface and pores within the coating can be observed, too.

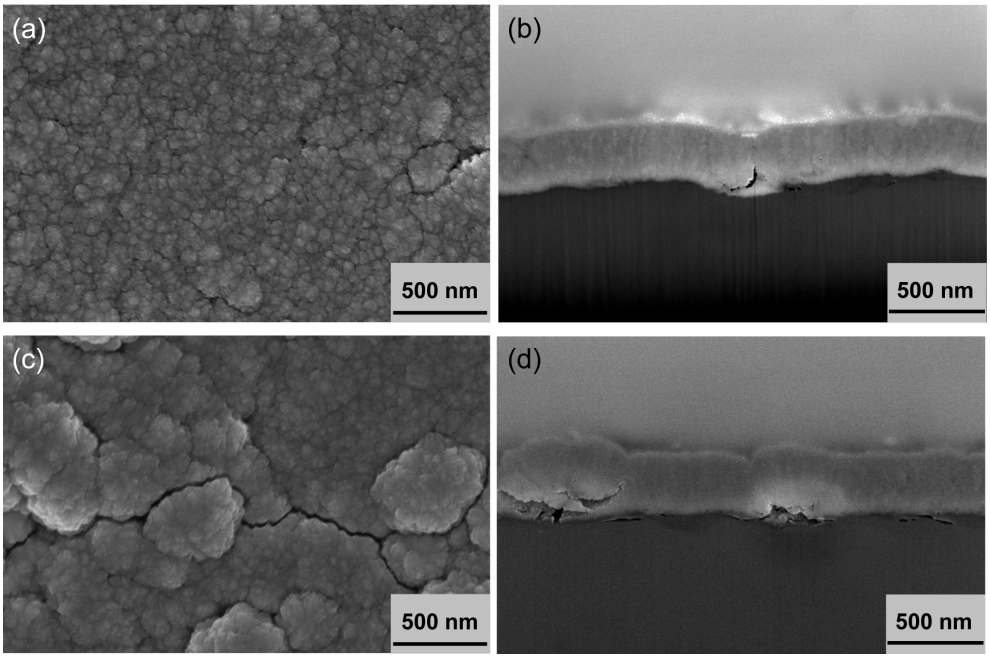

Figure 4.9: SEM images of a $TiC_{0.9}$ film on pyrolytic graphite, (a) film surface and (b) cross-section after sputter deposition, (c) film surface and (d) cross-section after annealing at 1035°C for 18 min

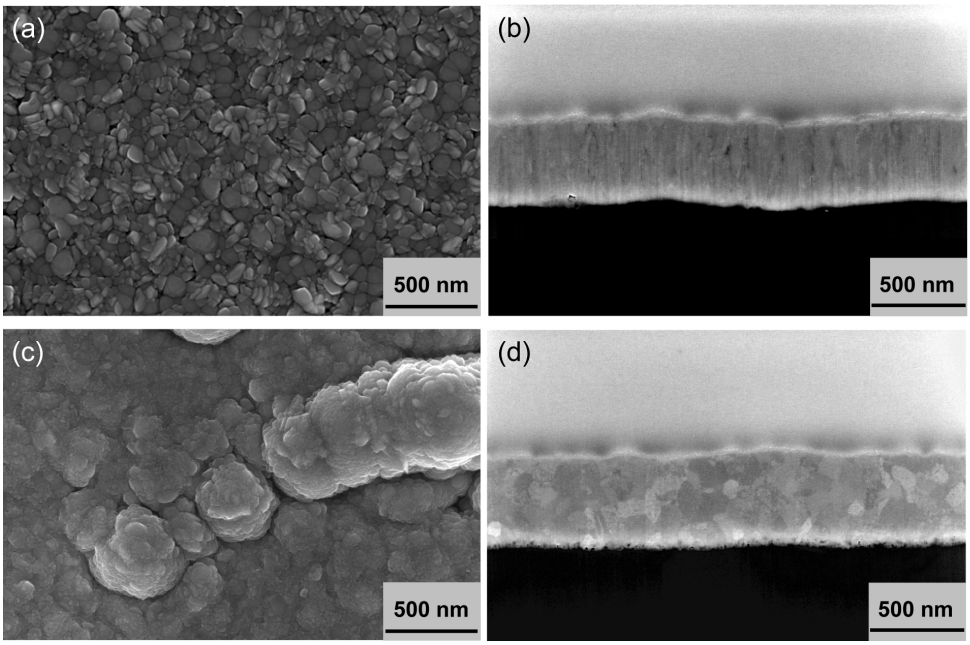

Figure 4.10: SEM images of a $TiC_{0.2}$ film on pyrolytic graphite, (a) film surface and (b) cross-section after sputter deposition, (c) film surface and (d) cross-section after annealing at 1035°C for 18 min

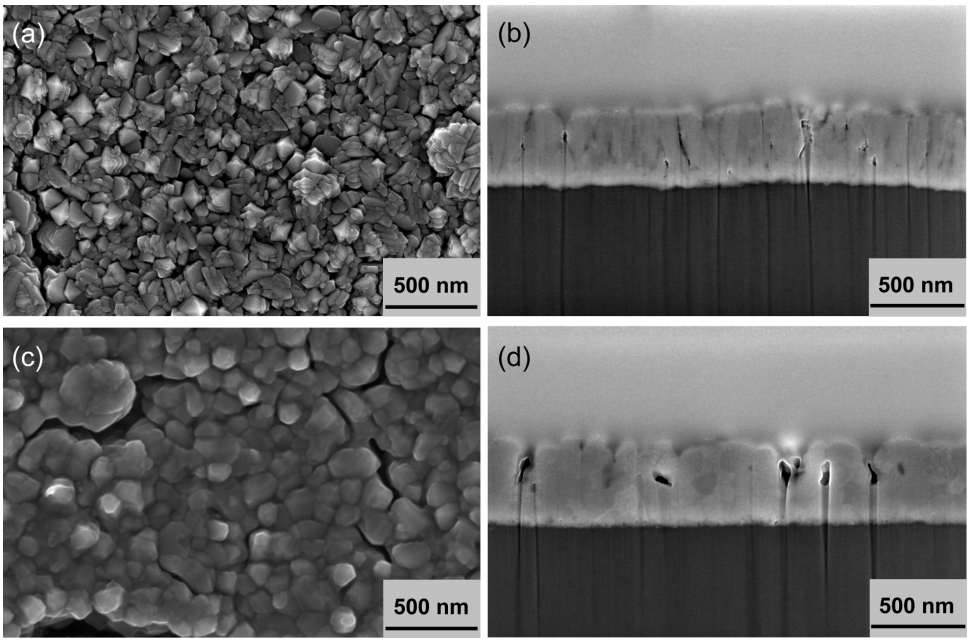

Figure 4.11: SEM images of a Ti film on pyrolytic graphite, (a) film surface and (b) cross-section after sputter deposition, (c) film surface and (d) cross-section after annealing at 1035°C for 18 min

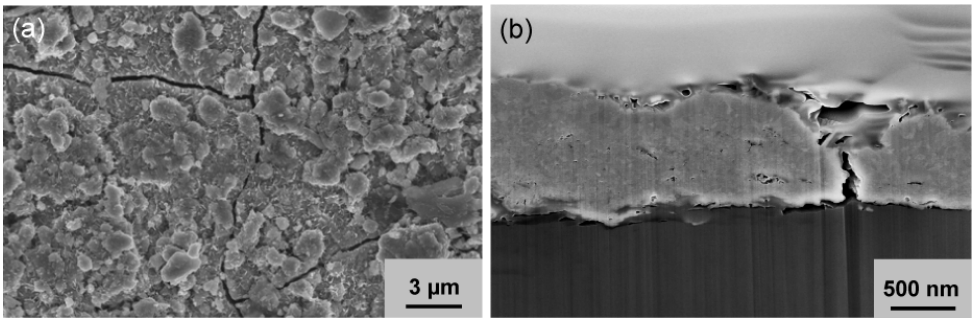

(a) Film surface

Figure 4.12: SEM images of a CVD-TiC film on pyrolytic graphite after deposition, (a) film surface and (b) cross-section

$TiC_{0.9}$, $TiC_{0.2}$, Ti and CVD-TiC on CFC NB31 All these films will be implemented for CFC/Cu braze joints (see chapter 5). Fig. 4.13 gives an impression how 500 nm of these films cover a CFC NB31 surface, before they are used for brazing. The films have been coated on the CFC surface, which is perpendicular to the ex-pitch fibers. The coatings structure of the $TiC_{0.9}$, $TiC_{0.2}$, Ti and CVD-TiC film is the same than observed on pyrolytic graphite (see cross-sections of fig. 4.13).

Differences in the coverage of the CFC surface could be detected in fig. 4.13. Magnetron sputtered coatings reproduce the topography of the CFC surface in a way that the fibers still can be identified, while CVD-TiC films fill every pore and every cavity between the ex-pitch fibers. However, the vertical sides of the ex-pitch fibers (i.e. areas perpendicular to the CFC surface) have been coated as well by the dual magnetron sputter deposition technique used in this work (see figs. 4.13 (b), (d) and (f)). This is due to the confocal arrangement of both sputter targets. But here, the coatings thickness is thinner and decreases with larger distance from the top.

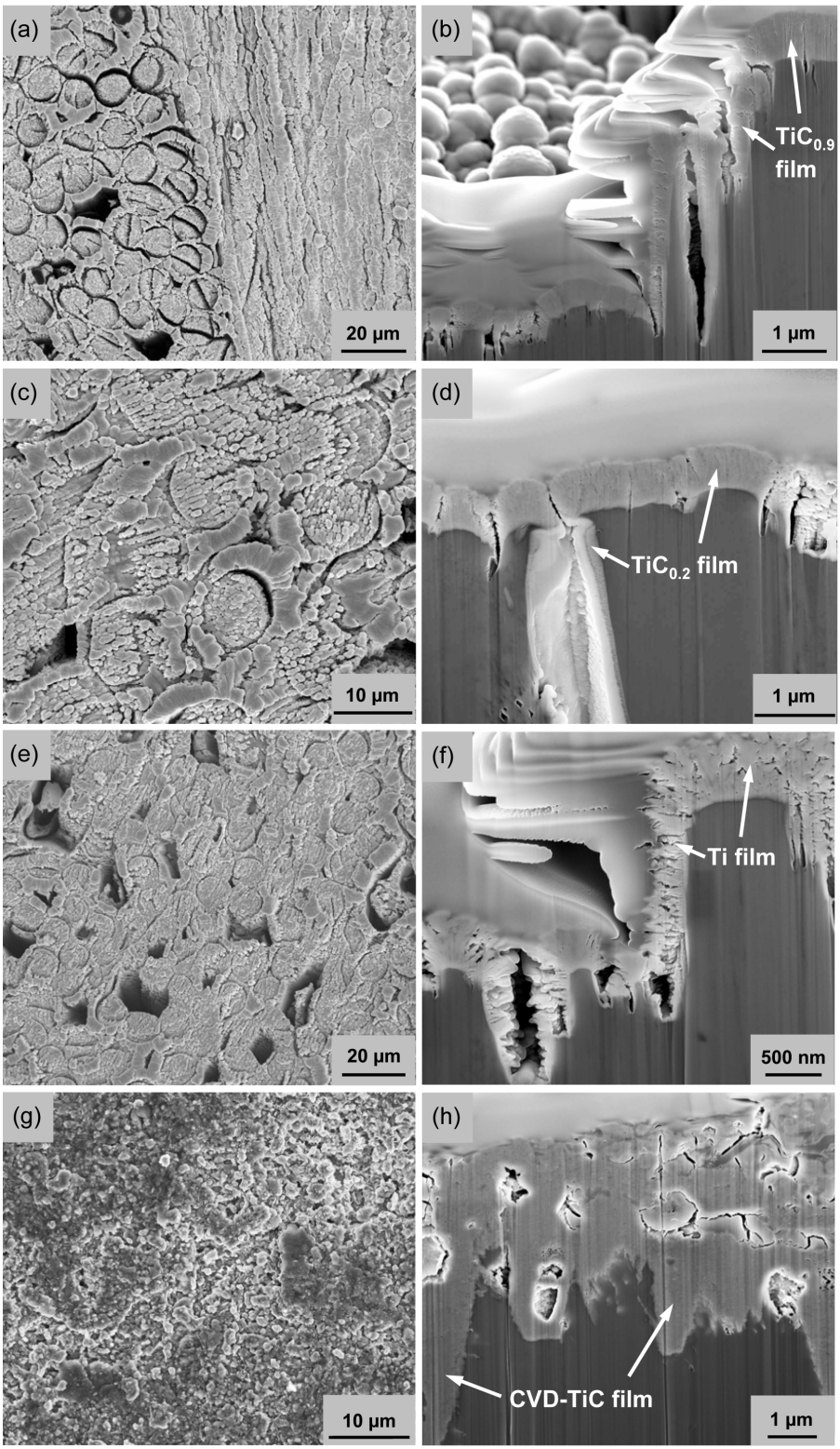

(a) Film surface

Figure 4.13: SEM images of TiC_x films deposited on CFC NB31 surfaces. (a) film surface and (b) cross-section of a magnetron sputter deposited $TiC_{0.9}$ film, (c) film surface and (d) cross-section of a magnetron sputter deposited $TiC_{0.2}$ film, (e) film surface and (f) cross-section of a magnetron sputter deposited Ti film, (g) film surface and (h) cross-section of a CVD-TiC film.

4.2 Stress in TiC_x films

Films that have been coated by atomic deposition processes (e.g. PVD or CVD methods) are usually in a stressed state. Large tensile stresses may lead to cracking of the film, large compressive stresses to buckling [72–74]. Both effects can lead to an increased surface roughness and to poor bonding, which results in delamination of the coating. A loss of the structural homogeneity makes a further technical use of these films impossible. Avoiding these effects and the control of the residual stresses are the most important issues of thin TiC_x film deposition processes with respect to a precise performance of wettability experiments (see section 4.3) and the implementation of TiC_x films in CFC/Cu divertor components.

Magnetron sputter deposited TiC_x films Many of the TiC_x films deposited by magnetron sputter deposition were subjected to extensive buckling, sometimes followed by delamination (see fig. 4.14). These observations were mainly made at films coated by low deposition rates or coated close to titanium carbide stoichiometry and seem to be a result of high compressive film stresses. Therefore, systematic investigations of the stress behavior of dual magnetron sputter deposited TiC_x layers were performed using both, the curvature and the $\sin^2\psi$ method (see section 3.3).

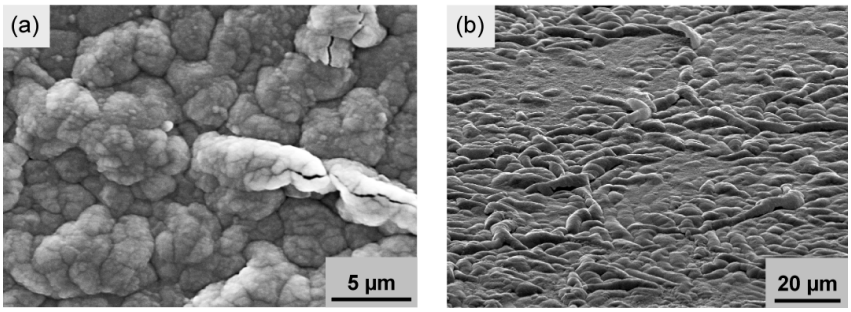

(a) Film surface

Figure 4.14: SEM images of a magnetron sputter deposited $TiC_{0.9}$ film coated on a pyrolytic graphite substrate showing extensive buckling, (a) film surface and (b) with tilted view

Intrinsic stress in thin films is generated by a variety of effects during the sputter deposition, which have been extensively discussed in literature [56, 77, 78, 180]. Plasma dependent processes can be controlled by varying different deposition parameters and therefore, influence the film growth conditions. These are, in the case of dual magnetron sputter deposited TiC_x films, the discharge power densities of both, the titanium and the graphite cathode, their correlation to each other (C/Ti power ratio, R) and the argon gas pressure during the deposition process. In general, power density almost linearly affects the amount of argon ions impinging on the cathodes and thus, the deposition rate r [77]. The ratio of the graphite to titanium discharge power determines the composition and therefore the factor of nonstoichiometry x (see section 4.1). The argon gas pressure p_{Ar} defines the mean free path of a sputtered target particle, which is the average distance covered by a sputtered particle between subsequent collisions with argon. In this work, at a mean free path of 2 cm for example, five or six collisions take place, because the target to substrate holder distance is fixed at 12 cm. The higher the pressure, the lower the mean free path and the lower the kinetic energy of the particles

arriving on the substrate, because kinetic energy is lost due to every elastic collision with an argon atom.

Table 4.1: Deposition parameters of magnetron sputtered TiC_x films used for intrinsic stress evaluation. Details about the titanium and graphite discharge power density (q_{Ti}, q_C), C/Ti power ratio R, composition (x in TiC_x), deposition rate r and content of oxygen impurity c_O are given for each coating. The entries are ordered in three levels of argon gas pressure p_{Ar}, three levels of composition (X1 – X3) and in three levels of power (P1 – P3). X3 represent coatings within $0.6 \leq x \leq 1.0$ (near stoichiometric TiC), X2 within $0.2 \leq x \leq 0.3$ and X1 at $x = 0$ (pure titanium). For X1 to X3 the levels of power are defined in a way that the entire width of each power spectrum (depends on the power supplies of both sputter targets) is divided in a low (P1), middle (P2) and high (P3) level. For X1 and X2 evaluations only for P3 were performed. Red fonts refer to cracked TiC_x coatings, which could not be investigated by the stress measurement methods.

		argon gas pressure p_{Ar}		
composition level	**power level**	$3 - 4 \cdot 10^{-3}$ mbar	$9 - 11 \cdot 10^{-3}$ mbar	$15 - 18 \cdot 10^{-3}$ mbar
X3	P3	$q_{Ti} = 3.4$ W/cm^2 $q_C = 11.4$ W/cm^2 $R = 3.3$ $x = 0.8$ $r = 8.3$ nm/min $c_O = 2$ at.%	$q_{Ti} = 3.4$ W/cm^2 $q_C = 11.4$ W/cm^2 $R = 3.3$ $x = 0.7$ $r = 9.0$ nm/min $c_O = 2$ at.%	$q_{Ti} = 3.4$ W/cm^2 $q_C = 11.4$ W/cm^2 $R = 3.3$ $x = 0.6$ $r = 8.6$ nm/min $c_O = 2$ at.%
X3	P2	$q_{Ti} = 1.4$ W/cm^2 $q_C = 4.5$ W/cm^2 $R = 3.3$ $x = 1.0$ $r = 3.3$ nm/min $c_O = 1$ at.%	$q_{Ti} = 1.4$ W/cm^2 $q_C = 4.5$ W/cm^2 $R = 3.3$ $x = 0.7$ $r = 3.6$ nm/min $c_O = 2$ at.%	$q_{Ti} = 1.4$ W/cm^2 $q_C = 4.5$ W/cm^2 $R = 3.3$ $x = 0.6$ $r = 3.2$ nm/min $c_O = 2$ at.%
X3	P1	$q_{Ti} = 0.6$ W/cm^2 $q_C = 1.9$ W/cm^2 $R = 3.3$ $x = 0.8$ $r = 1.1$ nm/min $c_O = 2$ at.%	$q_{Ti} = 0.6$ W/cm^2 $q_C = 1.9$ W/cm^2 $R = 3.3$ $x = 0.7$ $r = 1.4$ nm/min $c_O = 2$ at.%	$q_{Ti} = 0.6$ W/cm^2 $q_C = 1.9$ W/cm^2 $R = 3.3$ $x = 0.6$ $r = 1.3$ nm/min $c_O = 2$ at.%
X2	P3	$q_{Ti} = 13.6$ W/cm^2 $q_C = 11.4$ W/cm^2 $R = 0.8$ $x = 0.3$ $r = 30.0$ nm/min $c_O = 2$ at.%	$q_{Ti} = 13.6$ W/cm^2 $q_C = 11.4$ W/cm^2 $R = 0.8$ $x = 0.2$ $r = 30.7$ nm/min $c_O = 4$ at.%	$q_{Ti} = 13.6$ W/cm^2 $q_C = 11.4$ W/cm^2 $R = 0.8$ $x = 0.2$ $r = 30.0$ nm/min $c_O = 5$ at.%
X1	P3	$q_{Ti} = 13.6$ W/cm^2 $R = 0$ $x = 0$ $r = 33.3$ nm/min $c_O = 3$ at.%	$q_{Ti} = 13.6$ W/cm^2 $R = 0$ $x = 0$ $r = 36.8$ nm/min $c_O = 6$ at.%	$q_{Ti} = 13.6$ W/cm^2 $R = 0$ $x = 0$ $r = 38.0$ nm/min $c_O = 5$ at.%

Generalizations with respect to stress are difficult to make for sputtered films, because of the complexity of the plasma environment and the effect of the argon gas pressure. Normally, stress in thin films is tensile, e.g. for evaporated films reported in [56,78]. In sputter deposition processes compressive film stresses are often observed [181–184]. The incorporation of high energetic argon atoms which are reflected and neutralized at the sputter targets tends to compression of the upgrowing film [56]. On the other side, oxygen incorporated in the film favores tension.

TiC_x films were coated with different power densities, C/Ti power ratios and argon gas pressures on quartz glass slices in order to evaluate their intrinsic stress behavior using both, the curvature and the $\sin^2\psi$ method (see section 3.3). Tab. 4.1 gives detailed information about the parameters used for deposition. The influence of the deposition rate and argon gas pressure on the intrinsic stress of TiC_x coatings is shown in fig. 4.15. This data selection is devoted for films coated at a C/Ti power ratio of $R = 3.3$ (labeled as X3 in tab. 4.1). Both stress measurement methods demonstrate similar behavior and illustrate that these TiC_x layers tend to compressive stress. It is known that the stress is compressive when film atoms are too close. Thus, the atomic arrangement of these TiC_x films is quite close.

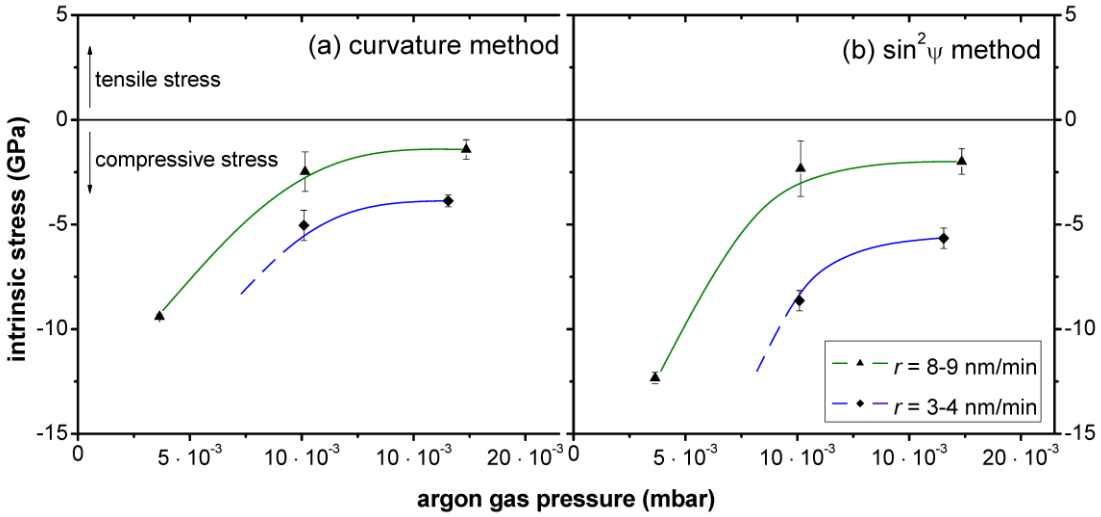

(a) Curvature method

Figure 4.15: Intrinsic stress of magnetron sputtered TiC_x films vs. argon gas pressure p_{Ar}. The C/Ti power ratio of these samples was $R = 3.3$, composition was determined to $0.6 \leq x \leq 1.0$. They differ only in their deposition rates (triangles: $r = 8 - 9\,\mathrm{nm/min}$, quadrangles: $r = 3 - 4\,\mathrm{nm/min}$). Analysis was performed by (a) the curvature method and (b) the $\sin^2\psi$ method.

The stress behavior of fig. 4.15 is highly affected by the modification of the argon gas pressure. Increasing the argon gas pressure leads to a stress reduction. A similar behavior is reported in [180,181]. Compressive stress was also generated due to argon atoms incorporated in the films, especially at low gas pressures. Oxygen incorporation can be neglected as stress determining factor for magnetron sputter deposited TiC_x coatings, because here, its concentration is relatively low (2 *at.*%, measured by RBS, see also tab. 4.1). Different deposition

rates (triangles: $r = 8 - 9\,\mathrm{nm/min}$, quadrangles: $r = 3 - 4\,\mathrm{nm/min}$) show that compressive stress also decreases with higher rates.

In fig. 4.15 the maximum of compression was reached at -9.4 GPa (curvature method) and -12.3 GPa ($\sin^2\psi$ method), respectively. Such high compressive stresses are unusual for magnetron sputter deposited TiC_x films. Coatings at $r = 1 - 2\,\mathrm{nm/min}$ must exceed these values, because they collapsed during deposition, even at high argon gas pressures. This behavior was also observed for the coating at low argon gas pressure and $r = 3 - 4\,\mathrm{nm/min}$. Thus, these films could not be evaluated.

In fig. 4.16, the intrinsic stress measured by (a) the curvature and (b) the $\sin^2\psi$ method is plotted as a function of the factor of nonstoichiometry x. These magnetron sputter deposited TiC_x films were coated by the high power level P3 mentioned in tab. 4.1 for three different discharge power ratios (blue: $R = 0$, X1; red: $R = 0.8$, X2; green: $R = 3.3$, X3) and three areas of different argon gas pressure (triangles showing downwards: $p_{Ar} = 3 - 4 \cdot 10^{-3}\,\mathrm{mbar}$, rectangles: $p_{Ar} = 9 - 11 \cdot 10^{-3}\,\mathrm{mbar}$ and triangles showing upwards: $p_{Ar} = 15 - 18 \cdot 10^{-3}\,\mathrm{mbar}$). Going from $x = 1$ (stoichiometric TiC) to $x = 0$ (pure titanium) the stress of the films decreases from compression to an almost stress-free state. TiC_x films coated at $p_{Ar} = 3 - 4 \cdot 10^{-3}\,\mathrm{mbar}$ reaches the low-stress state not until $x = 0$, while it is already obtained at $x = 0.3$ for higher argon gas pressures. This trend can be correlated to the structural transition of fcc-TiC into hcp-titanium crystallinity shown in fig. 4.4 (see section 4.1). Apparently, the crystal constitution of face centered cubic titanium carbide favors compression induced by the incorporation of small carbon atoms in octahedral vacancies in the titanium lattice. According to [56], incorporated oxygen atoms favor tension in sputter deposited films. Indeed, a slight increase of the oxygen content can be observed for TiC_x coatings with decreasing x (see tab. 4.1). That was expected due to the high oxygen affinity of titanium.

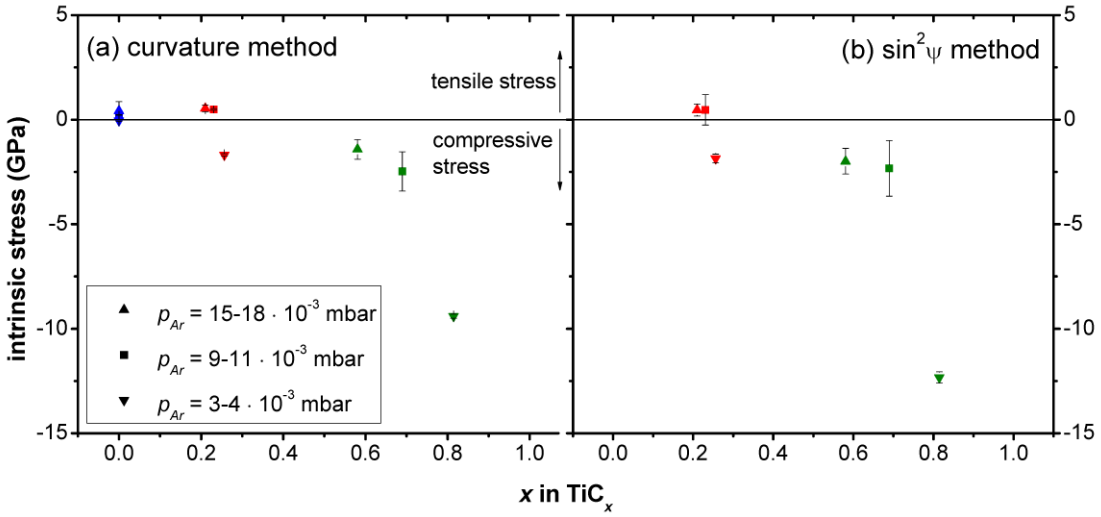

(a) Curvature method

Figure 4.16: Intrinsic stress of magnetron sputtered TiC_x films vs. factor of nonstoichiometry x. These coatings were deposited using a high power level (details can be found in tab. 4.1; here, this power level is labeled as P3), different C/Ti power ratios (blue: $R = 0$ (X1), red: $R = 0.8$ (X2), green: $R = 3.3$ (X3)) and three areas of different argon gas pressure. Analysis was performed by (a) the curvature method and (b) the $\sin^2\psi$ method.

In fig. 4.16 the argon gas pressure is crucial for stress differences within each compositional level (X1 – X3, notation: see tab. 4.1). By increasing the pressure the coatings tend to tensile stress (as already shown for X3 in fig. 4.15) and a stress transition from compression to tension was achieved for X1 and X2. Furthermore, compositional differences can be detected for varied argon gas pressures, although each TiC_x film of X1 to X3 was coated with the same discharge power ratio. The higher the pressure the lower is x. Comparing their rough atomic weight carbon atoms (12 g/mol) are stronger deflected by argon plasma particles (40 g/mol) than titanium atoms (48 g/mol). Thus, the coating contains systematically less carbon at increased argon gas pressure.

Both stress measurement methods (curvature method and $\sin^2\psi$ method) obtained similar trends with values in the same order of magnitude. Thus, high compressive stress values observed in fig. 4.15 and fig. 4.16 could be confirmed. Marginal differences were generated by inaccuracies, e.g. due to an approximation of the elastic and thermal material properties. $\mathrm{Sin}^2\psi$ method measurements with titanium films ($R = x = 0$, X1) have not been possible, because due to texture the titanium peak (0 0 2) dissapeared at the most tilting angles ψ. Such an extensive columnar fiber texture with highly orientated crystal grains (see fig. 4.6 (a) of section 4.1) inhibits the use of the $\sin^2\psi$ method. For films at $R = 0.8$ (X2) and $R = 3.3$ (X3) texture effects were still present (see figs. 4.6 (b) and (c) of section 4.1), but did not affect the formation of XRD reflexes over the whole range of tilting angles ψ.

The intrinsic stress of magnetron sputtered TiC_x films can be adjusted varying the deposition parameters used for this work: power density (both cathodes), C/Ti power ratio and argon gas pressure. Basically, three effects could be observed:

1. Increasing argon gas pressure favors tensile stress (stronger effect at $TiC_{x\to 1}$)
2. Increasing the power level (thus, the deposition rate) leads to tensile stress
3. Increasing the C/Ti power ratio R (thus, the factor of nonstoichiometry x) tends to compression

Investigations about intrinsic stress of magnetron sputtered TiC_x films show that low-stress coatings can be achieved in the whole stoichiometry range from $x = 0$ to $x = 1$. Any failure mechanism described in the beginning of this section can be avoided.

CVD-TiC films The stress state of CVD-TiC films on pyrolytic graphite was measured by the $\sin^2\psi$ method using the TiC (2 0 0) peak. Intrinsic stress was determined to be strongly compressive at -7.4 GPa. In literature a stress of -4.25 GPa is reported for CVD-TiC films coated on austenitic stainless steel substrates [185].

4.3 Wettability on TiC_x films

Wetting experiments on TiC_x films were performed in order to study their wetting improving behavior for CFC/Cu brazing applications. The brazing alloys Copper-ABA (Cu-Ti alloy) and Gemco (Cu alloy) were used as wetting liquids (for chemical composition see section 3.1.2).

For this purpose, 500 nm thick magnetron sputter deposited TiC_x films were produced within the composition range of $0 \leq x \leq 1$. As summarized in section 4.1.2, two different crystal structures were found for this range: the α-Ti phase with hexagonal closest packed (hcp) structure and the TiC phase with face-centered cubic (fcc) structure. They were found

for the stoichiometries $x = 0$ and $x = 0.6 - 1$, respectively. In between ($0 < x < 0.6$), a distorted crystal structure was determined. For the wetting experiments in this section, magnetron sputtered TiC_x films were chosen on the basis of these different zones of crystallinity (one film of each zone): hcp Ti, fcc $TiC_{0.9}$ and the intermediate $TiC_{0.2}$ (see fig. 4.17). The characterization of these films can be found in section 4.1. The low-stress inducing effects developed in section 4.2 were applied on these films to avoid any deposition defects (e.g. buckling, delamination), which can particularly influence the wetting behavior.

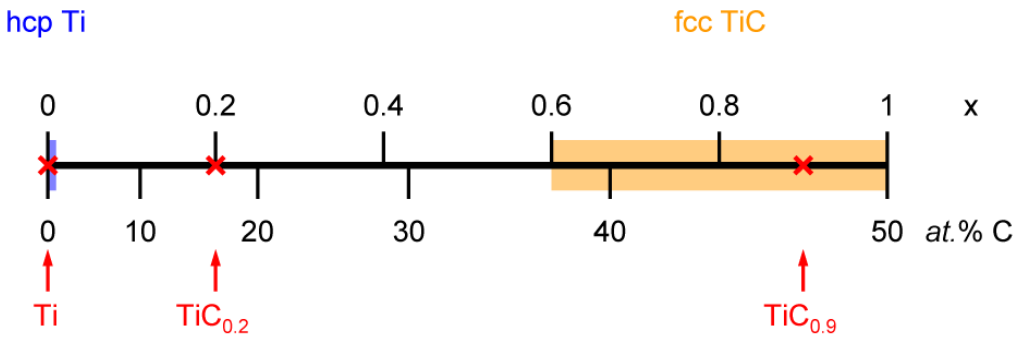

Figure 4.17: Magnetron sputter deposited TiC_x films in the range of $0 \leq x \leq 1$ exhibit different zones of crystallinity: hexagonal closest packed (hcp) α-Ti for $x = 0$ and face-centered cubic (fcc) TiC for $x = 0.6 - 1$. In between, a metastable crystal structure was found. For the wetting experiments, the films Ti, $TiC_{0.2}$ and $TiC_{0.9}$ were chosen in order to represent each zone of crystallinity.

In addition, 750 nm thick CVD-TiC films, delivered by the British company Archer Technicoat, were subjected to the wetting experiments. Their composition is close to magnetron sputtered $TiC_{0.9}$ coatings. Thus, a similar wetting behavior of these films would be expected. However, the CVD-TiC coatings exhibit a high amount of stress induced deposition defects (cracks and delamination), as it was shown in the previous sections. The influence of these deposition defects on the wetting behavior will be evaluated in this section.

Uncoated pyrolytic graphite substrates serve as reference samples in order to compare the wettability properties between TiC_x films and the systems Copper-ABA/C or Gemco/C.

Wetting by Copper-ABA is of main interest, because it is aimed to improve the wetting characteristics of the Copper-ABA brazing technology developed by Ansaldo Ricerche (see also sections 1.3 and 1.4). However, the wettability behavior of Gemco on TiC_x films was investigated as well in order to evaluate its suitability as an alternative brazing alloy for CFC/Cu brazing applications. Brazing by Gemco would have the advantage that it requires a lower process temperature than brazing by Copper-ABA. The Gemco melting temperature is 975°C, while it is 1024°C for Copper-ABA.

4.3.1 Contact angles

The degree of wetting is generally indicated by the contact angle formed at the interface between solid and liquid. The contact angle is specific for any given system and, under equilibrium conditions, governed by the surface and interfacial energies. It is said that the liquid wets the surface of a solid when the contact angle is less than 90°. On the other hand, a poor wetting of the solid is considered, if the contact angle is greater than 90°. Generally, it is

accepted that the smaller the contact angle, the better the wettability. In the case of reactive wetting, the initial contact angle θ_0 (recorded immediately after melting of the liquid) and the final contact angle θ_F are important parameters.

4.3.1.1 Wetting by Copper-ABA

High temperature (~1030°C) sessile drop experiments of Copper-ABA on uncoated and TiC_x coated pyrolytic graphite substrates were performed using the contact angle measurement device described in section 3.4. This device guarantees fast heating and a reproducible temperature evolution. The number of samples investigated per system (uncoated pyrolytic graphite, magnetron sputter deposited $TiC_{0.9}$, $TiC_{0.2}$ and Ti and CVD coated titanium carbide) was four. Every curve shown in one of the following contact angle vs. time plots was averaged by all data determined for the same wetting system. It has to be noted that the wetting experiments were accompanied by a high reproducibility, i.e. large errors of the contact angle evolutions in one wetting system were not observed.

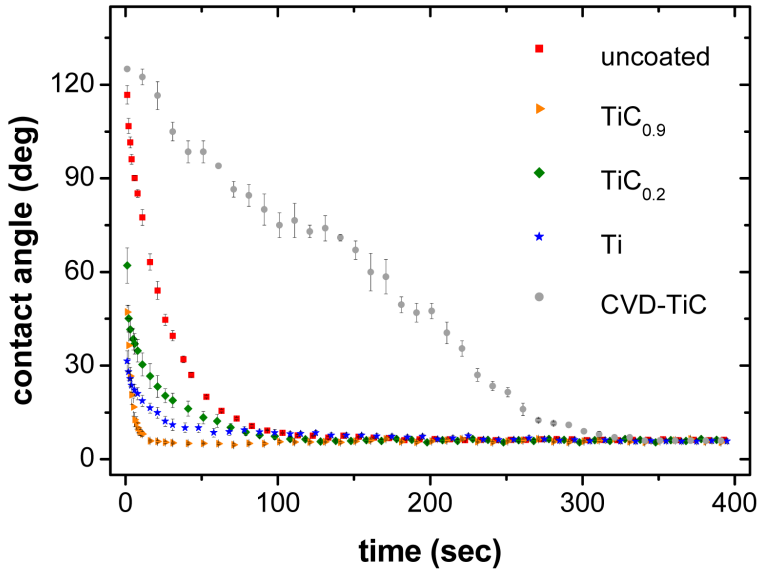

Figure 4.18: Wetting behavior of Copper-ABA on TiC_x films. The averaged contact angle evolutions vs. time were examined on magnetron sputter deposited $TiC_{0.9}$, $TiC_{0.2}$ and Ti films, on CVD-TiC films and on uncoated reference samples. All coatings were deposited on pyrolytic graphite substrates.

Results of the Copper-ABA contact angle measurements on uncoated and TiC_x coated pyrolytic graphite substrates are presented in fig. 4.18. The averaged contact angle evolutions are plotted as a function of time. For comparison, fig. 4.19 shows the initial (θ_0) and the final contact angle (θ_F) of each system. At $t = 0$ (Copper-ABA melting), all liquid droplets started to react with their surfaces (reactive wetting) and the contact angles decreased significantly (see fig. 4.18). A final contact angle of $\theta_F = 6°$ is observed for each system (see fig. 4.19). Thus, the Copper-ABA alloy ensures high wettability on uncoated and on TiC_x coated pyrolytic graphite substrates. The formation of such low final contact angles were expected due to the high titanium activity of the active brazing alloy Copper-ABA and will be explained later. The final contact angle of the uncoated reference samples is similar than reported for the

system Copper-ABA on vitreous carbon [37].

Fig. 4.18 shows that the time dependency of each contact angle curve is different. For example the contact angle evolution of CVD-TiC is almost linear, while it is similar to an exponential decay in the other systems. For $TiC_{0.9}$ films, the final contact angle is already realized after 10 s, while the liquid Copper-ABA droplet needs about 150 s to spread completely on uncoated, $TiC_{0.2}$ and Ti coated pyrolytic graphite and even 5 min on CVD-TiC films. Thus, $TiC_{0.9}$ films seem to improve the wetting behavior of Copper-ABA on C. The time dependency is a main factor that determines the wetting promoting behavior of TiC_x films and will be extensively discussed in the section about reaction kinetics 4.3.2.

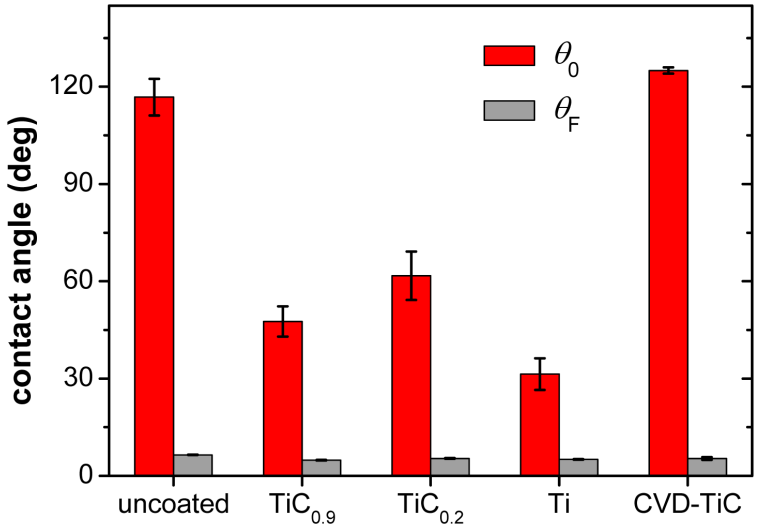

Figure 4.19: Averaged parameters of wetting experiments illustrated in fig. 4.18: initial θ_0 and final contact angle θ_F

Concerning the wetting behavior of TiC_x films, the initial contact angle θ_0 is as well a parameter of high relevance. θ_0 describes the wettability in the first moment of contact with the liquid Copper-ABA, i.e. before the wetting reactions have started. Fig. 4.19 compares the averaged values of the initial contact angles that can be determined in the wetting curves of fig. 4.18. In the case of the reference samples (uncoated pyrolytic graphite substrates), a high initial contact angle of $\theta_0 = 117°$ is observed, similar to the equilibrium contact angle of non-alloyed copper on graphite ($\theta = 122°$ [16]). In this situation, wetting at $t = 0$ is a C-Cu system, because the titanium concentration at the Copper-ABA/graphite interface is still too low. In this system, the solubility of C into liquid copper is very small (0.0001 *wt.*% C at 1373 K, 0.00015 *wt.*% C at 1573 K, 0.0005 *wt.*% C at 1773 K and 0.003 *wt.*% C at 1973 K [186]) and no C-Cu phases exist [187]. A poor initial wetting of liquid Copper-ABA on uncoated C is the consequence. On the other side, initial contact angles lower than 90° could be detected on magnetron sputtered $TiC_{0.9}$, $TiC_{0.2}$ and Ti films. Thus, the initial wetting behavior of Copper-ABA on C can be improved by coating with any magnetron sputter deposited TiC_x film. However, in these wetting systems ($TiC_{0.9}$, $TiC_{0.2}$ and Ti), a maximum of θ_0 is observed for the metastable $TiC_{0.2}$ ($\theta_0 = 62°$), while $TiC_{0.9}$ and Ti exhibit the lowest values ($\theta_0 = 47°$ and 31°). CVD-TiC coated pyrolytic graphite shows poor initial wetting with a value of $\theta_0 = 125°$. The liquid Copper-ABA droplets in this initial contact angle stage are presented in fig. 4.20, respectively.

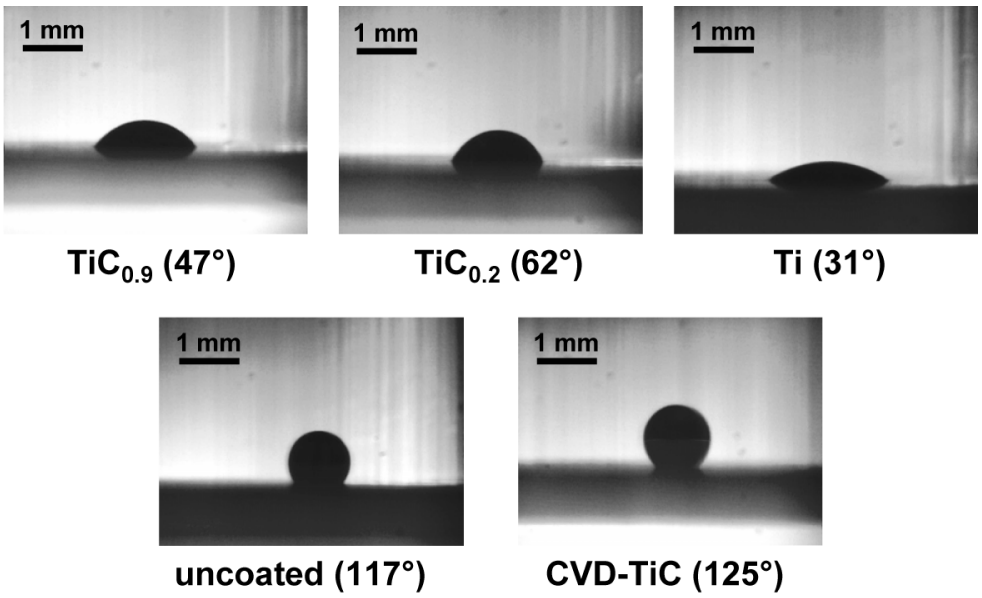

Figure 4.20: Initial contact angles θ_0 of Copper-ABA droplets on uncoated pyrolytic graphite, magnetron sputter deposited $TiC_{0.9}$, $TiC_{0.2}$ and Ti films and CVD coated TiC films

In the following, the thermodynamic aspects of the wetting reactions that occur during wetting of Copper-ABA on TiC_x films will be discussed on the basis of the reported literature and thermodynamic simulations. However, due to their complexity there is presently no satisfactory fundamental understanding of wetting in Copper-ABA/TiC_x systems.

Copper-ABA wets all surfaces investigated in fig. 4.18 and leads to low final contact angles. For these wetting events, reactive mechanisms are responsible, which are initiated by the active element Ti.

In the reference system Copper-ABA on graphite, the titanium atoms of the liquid Copper-ABA alloy react with carbon atoms from the substrate. They form substoichiometric titanium carbide ($TiC_{x<1}$) at the Copper-ABA/graphite interface [16, 188], according to the reaction:

$$(\mathrm{Ti})_{\mathrm{Cu}} + \langle \mathrm{C} \rangle_{\mathrm{graphite}} \longrightarrow \langle \mathrm{TiC}_{x<1} \rangle \tag{4.1}$$

$TiC_{x<1}$ represents a certain substoichiometric composition, which is thermodynamically favored in Cu/C systems including the element titanium (enthalpy of formation: -184 kJ/mol at $T = 1100$°C [153]). It is shown in [16, 189] that the $TiC_{x<1}$ reaction product significantly improves wetting of liquid copper. Actually, it is not stoichiometric TiC that favors wetting[1]. However, the exact composition of $TiC_{x<1}$ is not reported in literature and could not be examined experimentally.

Thermo-Calc DICTRA [194–196] simulations, performed by Dr. Klaus Schmid, were used to determine the composition of $TiC_{x<1}$. This software models the formation of thermodynamically stable phases and the diffusive transport of elements within these phases. The calculations are therefore limited by the available thermodynamic (chemical potential) and kinetic (mobility of species) data. The Copper-ABA/graphite system was reduced to a binary Ti/C diffusion couple, because the simulation failed to produce a stable solution for the

[1] It is reported that stoichiometric TiC even tends to high contact angles ($\theta \approx 120$°), when it is wetted by liquid copper [190–193].

system Cu-Ti-C due to the low solubility of copper in carbon [186]. Diffusion processes and compound formation were simulated at a temperature of 1100°C. The software determined the precipitation of fcc $TiC_{x<1}$ at the interface and simulated the diffusive growth of the carbide phase. The results are presented in fig. 4.21, which shows the formation of a $TiC_{x<1}$ interlayer. The carbon composition of this interlayer is determined to 36 *at.*% and correlates to a stoichiometry of $x = 0.6$.

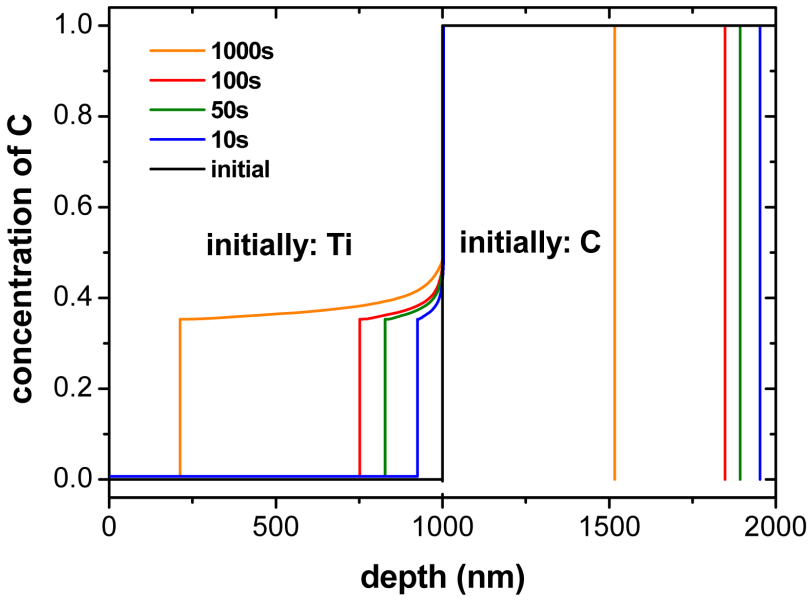

Figure 4.21: Thermo-Calc DICTRA simulations of the diffusive growth of a titanium carbide phase after formation from a Ti/graphite diffusion couple at a temperature of 1100°C

During wetting of Copper-ABA on TiC_x films, the process of TiC_x dissolution has to be considered as well. This process was discussed by Frage et al. [30], who investigated the Cu/TiC system. During the TiC_x dissolution, the titanium atoms from the TiC_x films transfer to the melt and graphite precipitates at the Copper-ABA/TiC_x interface, according to the reaction:

$$\langle TiC_x \rangle \longrightarrow (Ti)_{Cu} + \langle C \rangle_{graphite} \tag{4.2}$$

Both reactions, the formation of $TiC_{x<1}$ (eq. 4.1) and the dissolution of TiC_x (eq. 4.2), are simultaneous processes during wetting of Copper-ABA on TiC_x films and they are in a state of balance. As shown before, the process of eq. 4.1 favors wetting, whereas the process of eq. 4.2 inhibits wetting due to the insolubility of the graphite precipitations into liquid copper. The amount of precipitated graphite depends on the amount of titanium that is transferred into the Copper-ABA melt and is related to the equilibrium titanium concentration in the molten solution, which is in contact with the carbide phase. The equilibrium titanium concentration depends on the activity of titanium. Thus, the thermodynamic equilibrium in the Copper-ABA/TiC_x system including the reactions of eq. 4.1 and eq. 4.2 depends on the activity of titanium in the melt.

Assuming wetting by pure copper and at a given temperature, the activity of titanium in liquid copper increases with decreasing x in TiC_x [30, 197]. In this case, the $TiC_{0.9}$ films

would have not been wetted. But due to the initial content of 2.8 *at.*% Ti in the Copper-ABA alloy, the activity of titanium in the melt is already high enough. Thus, the tendency of $TiC_{x<1}$ formation (eq. 4.1) is favored and low final contact angles in the wetting system Copper-ABA/TiC_x can be achieved for all TiC_x stoichiometries, even for the $TiC_{0.9}$ films.

The $TiC_{x<1}$ formation in the system Copper-ABA/$TiC_{0.9}$ was confirmed by Thermo-Calc DICTRA simulations. A simplified system (Cu + 3*at.*% Ti/TiC) was chosen for the calculation at the temperature of 1100°C. Fig. 4.22 illustrates that Ti from the liquid Cu-Ti mixture segregates at the interface under formation of a thin (4 nm) substoichiometric titanium carbide film. It is well established that even a very thin layer may profoundly affect the wetting behavior [30]. Again, the stoichiometry of this film can be determined to $x = 0.6$.

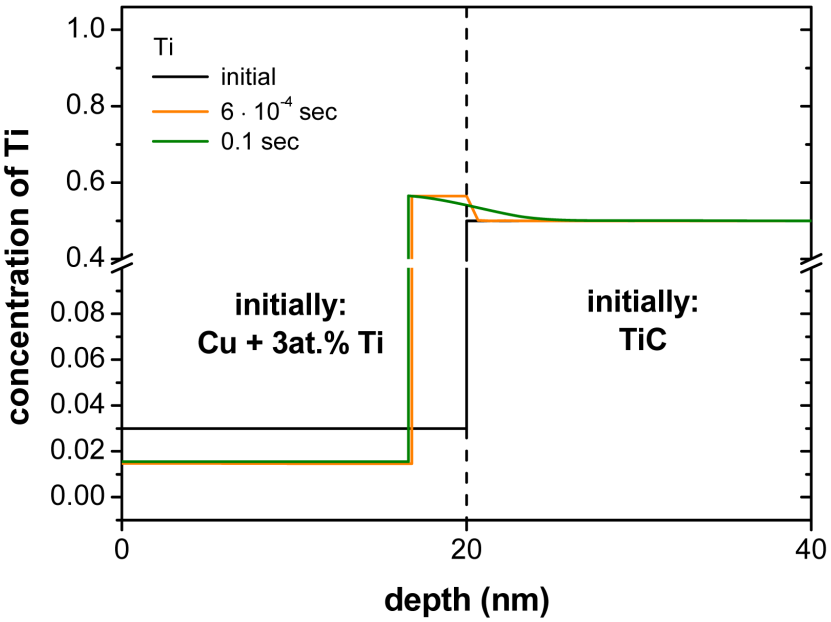

Figure 4.22: Thermo-Calc DICTRA simulations of the system Cu + 3*at.*% Ti/TiC at a temperature of 1100°C in order to evaluate processes as diffusion and compound formation

4.3.1.2 Wetting by Gemco

Contact angle measurements with Gemco brazing alloy were performed at ~980°C using the sessile drop device. Magnetron sputter deposited $TiC_{0.9}$, $TiC_{0.2}$ and Ti films as well as CVD-TiC films on pyrolytic graphite were employed as substrates (two samples per system). The contact angles as a function of time are presented in fig. 4.23.

The involved reactions of the Gemco/TiC_x systems are the same as described for the Copper-ABA/TiC_x systems: (1) formation of $TiC_{x<1}$ (see eq. 4.1) and (2) dissolution of TiC_x (see eq. 4.2). The thermodynamic equilibrium depends again on the activity of titanium.

Gemco alloy does not wet uncoated pyrolytic graphite (constant high contact angle of $\theta = 117°$). Due to the absence of a reactive element like titanium, a contact angle was observed, which is in the same range as that of pure liquid copper on carbon substrates ($\theta = 122°$ [16]). Fig. 4.24 (a) illustrates the solidified Gemco droplet on an uncoated graphite surface.

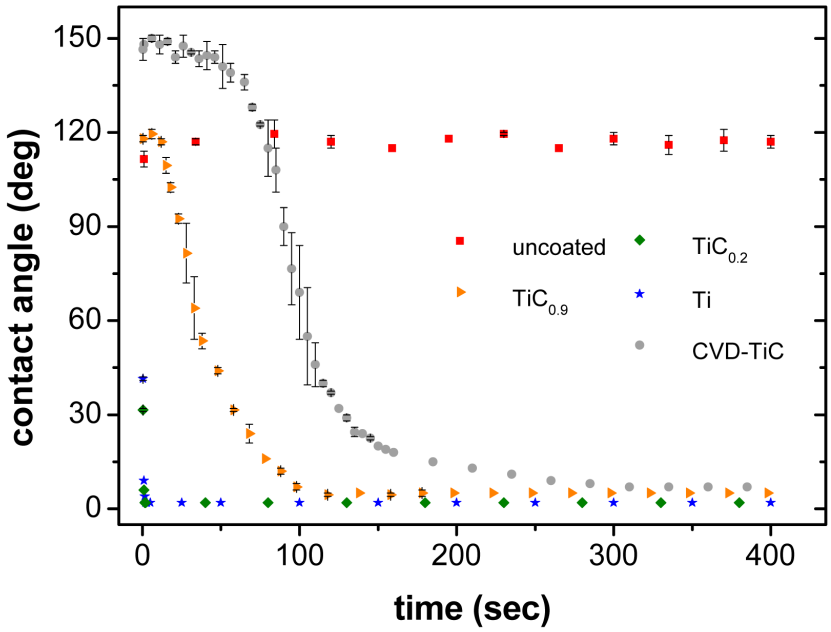

Figure 4.23: Wetting of Gemco on uncoated, TiC_x (magnetron sputter deposition) and TiC (CVD) coated pyrolytic graphite performed by the sessile drop device

Wetting experiments on magnetron sputter deposited $TiC_{0.9}$ films start with a high initial contact angle of $\theta_0 = 118°$, lead to a dynamic reaction and finally to a contact angle of $\theta_F = 5°$. However, it is known that liquid copper does not wet titanium carbide in the range of $0.65 < x \leq 1$ (low titanium activity in these systems) [190–193]. Thus, the titanium activity of the titanium-free Gemco alloy on $TiC_{0.9}$ should be low, too. But Gemco is alloyed with 0.3 *at.*% nickel. In the the Gemco/$TiC_{0.9}$ system, even small Ni additions have a wetting improving effect due to strong Ni–Ti inter-atomic interactions [30] that favor the transfer of Ti to the melt. A high interaction energy (-131 kJ/mole) in the binary Ni–Ti diluted liquid solution was reported in [198]. Therefore, the activity of titanium dissolved in liquid Gemco droplet has increased. Further, the solubility of C in molten Ni is higher by several orders of magnitude than that in molten Cu [30]. This implies that even relatively small additions of the alloying element Ni increase significantly the solubility of C in the Gemco alloy and, thereby, prevent the formation of graphite precipitations at the interface (according to the reaction of eq. 4.2), which inhibits wetting. Thus, wetting of copper on $TiC_{0.9}$ films can be significantly improved by small Ni additions. A wettability improving effect has not been reported for the alloying element Ge. Fig. 4.24 (b) shows a top view image of a $TiC_{0.9}$ film wetted by Gemco after the experiment. Thermal stresses, generated by different coefficients of thermal expansion, were released in cracking of the graphite surface. That crack is visible in fig. 4.24 (b) as ring next to the solidified Gemco droplet.

The wetting improving effect of small Ni additions is particularly intensified on substoichiometric TiC_x films. $TiC_{0.2}$ and Ti coatings wetted by Gemco lead to already low initial contact angles of $\theta_0 \approx 40°$ and to almost complete wetting ($\theta_F = 2°$) within a very short interval of 2 s. As figs. 4.24 (c) and (d) show, the Gemco alloy wetted large areas of these substrates. The wetting behavior of Gemco on $TiC_{0.2}$ and Ti films may also be influenced by the presence of the element Ni, which increases the Ti activity in the melt. In such a system, the TiC_x dissociation and free carbon precipitation at the interface (see eq. 4.2) will be inhibited [30].

The initial contact angle on non-optimized CVD titanium carbide substrates is extraordinarily high ($\theta_0 = 148°$). After a retardation of ~1 min it decreases to low angles ($\theta_F = 7°$) in the same manner as magnetron sputter deposited $TiC_{0.9}$ films (see fig. 4.24 (e)).

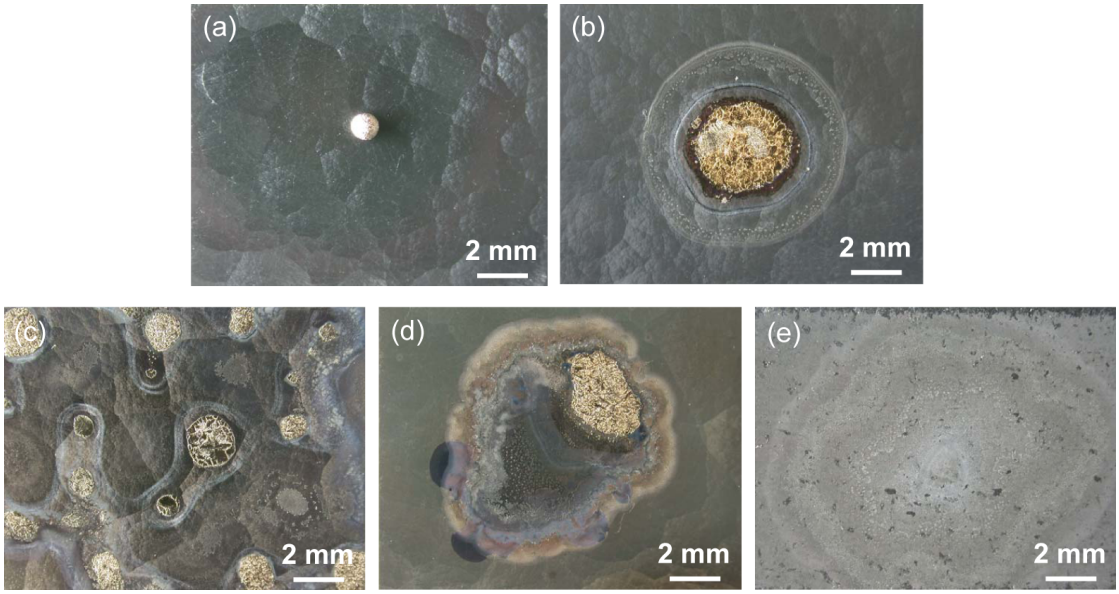

Figure 4.24: Top view images of uncoated (a), magnetron sputter deposited $TiC_{0.9}$ (b), $TiC_{0.2}$ (c), Ti (d) and CVD-TiC (e) coated pyrolytic graphite substrates after wetting experiments with Gemco alloy

4.3.2 Spreading kinetics

The spreading kinetics of the Copper-ABA and Gemco droplets are of high relevance in order to characterize the wetting improving behavior of TiC_x films. The observed spreading is controlled by the quasi two-dimensional growth of the $TiC_{x<1}$ reaction product parallel to the initial interface. Coupling between reaction and wetting processes is established at the triple line, which is defined as the contact line between the phases solid, liquid and vapor. The reaction rate between Ti and C at the triple line is a few orders of magnitude higher than that at the interface behind the triple line [16]. In fact, the liquid is continuously in contact with unreacted solid at the triple line, whereas at the interface far behind the triple line, the reaction occurs by slow diffusion through the solid $TiC_{x<1}$ layer. Thus, spreading is due to the quasi two-dimensional growth of a well wetted reaction layer and conversely, the preferential reactivity at the triple line is favored by the good wetting of the liquid on the reaction product $TiC_{x<1}$, allowing the liquid to be continuously in contact with unreacted substrate. Putting eq. 2.13 in eq. 2.12 and replacing θ by the contact angle on the reaction product θ_P, the reactive wetting driving force for $\theta < \theta_0$ is written as:

$$F_d(t) = \gamma_{lv} [\cos\theta_P - \cos\theta(t)] \tag{4.3}$$

When the contact angle reaches the equilibrium value of Copper-ABA or Gemco on the reaction product $TiC_{x<1}$, the triple line stops but the lateral extension of $TiC_{x<1}$ on the free surface of the substrate continues [199]. This effect is well visible in fig. 4.24 (b). However, because the Ti source (i.e. the triple line) and the reaction front get farther and farther apart,

the reaction slows down strongly. The same effect is reported in [200] for wetting of carbon by silicon-alloyed copper.

4.3.2.1 Wetting by Copper-ABA

The spreading kinetics due to the formation of a new compound can be sufficiently characterized by the time evolution of the drop base radius R_L, which is the distance between the center of the droplet and the triple line. It is presented in fig. 4.25 (a) for Copper-ABA/TiC_x systems at $T \sim 1030$°C. The $R_L(t)$ curves of uncoated and sputter coated TiC_x samples consist of one kinetic stage, curves of CVD-TiC samples of two different stages. In each stage the drop base radius is a nearly linear function of time (see black lines in fig. 4.25 (a)). These stages are attributed to the interfacial reaction between Copper-ABA and TiC_x films and characterize the velocity of the triple line. Fig. 4.25 (b) compares $\frac{dR_L}{dt}$ of each system. The significantly highest velocity of the triple line can be observed for $TiC_{0.9}$ films ($\frac{dR_L}{dt} = 143$ µm/s).

In this case of a constant triple line velocity, a stationary configuration with a constant chemical environment is established at the triple line during wetting. Thus, Copper-ABA spreading is reaction-limited for all TiC_x systems. The chemical kinetics at the triple line are rate-limiting, because diffusion of titanium atoms within the droplet is comparatively rapid (see also section 2.5.2). Before these linear stages, R_L increases parabolically with time, visible in all cases except $TiC_{0.9}$. It is assumed that during this stage a steady-state growth is not still established due to incomplete covering of the solid/liquid interface by the reaction product [111].

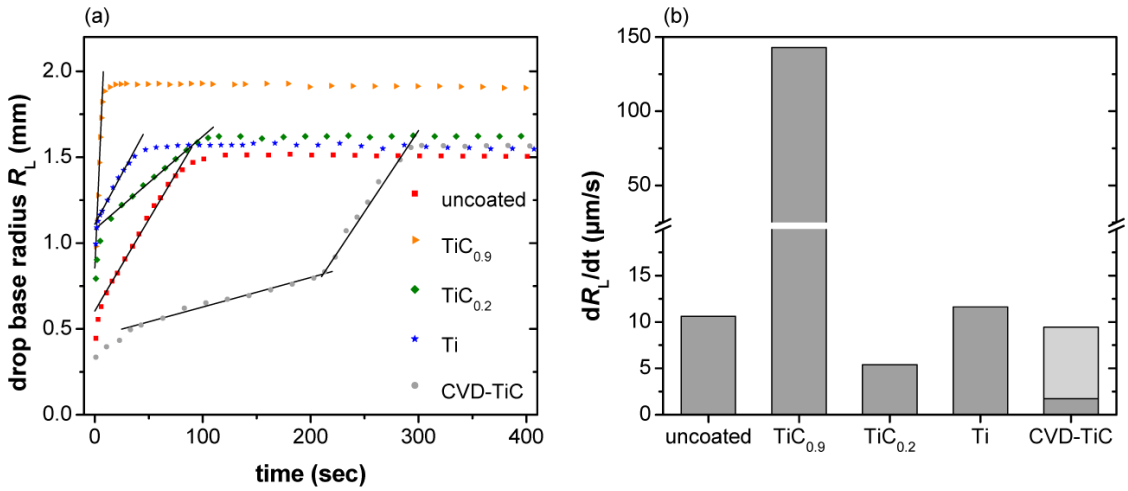

Figure 4.25: Results of wetting experiments using the sessile drop device: (a) drop base radii vs. time of Copper-ABA on uncoated, magnetron sputter deposited $TiC_{0.9}$, $TiC_{0.2}$, Ti and CVD-TiC coated pyrolytic graphite; (b) velocities of the drop base radius (two stages at CVD-TiC)

Writing the mass balance at the triple line and denoting by $v^m_{TiC_{x<1}}$ the molar volume of the reaction product, the velocity of the triple line for the reaction in eq. 4.1 forming $TiC_{x<1}$ is [16]:

$$\frac{\mathrm{d}R_\mathrm{L}}{\mathrm{dt}} = \mathrm{K}\, v^{\mathrm{m}}_{\mathrm{TiC_{x<1}}} \exp\left(\frac{-\triangle \mathrm{G}^*}{\mathrm{R}T}\right) \left(\mathrm{a_{Ti}} - \mathrm{a^{eq}_{Ti}}\right) \tag{4.4}$$

where $\mathrm{a}^{eq}_{\mathrm{Ti}}$ is the value of the activity of the reactive solute Ti in the liquid copper, which is in equilibrium with the substrate and the reaction product. $\triangle$ G* is the activation Gibbs energy of the reaction, R the gas constant and K is a constant. An increased titanium activity, e.g. at TiC_x films with high titanium concentration, could increase the reaction rate, but as we know from fig. 4.25 (b) only $TiC_{0.9}$ films (low-titanium TiC_x films) exhibit much higher velocities than the other wetting systems. The titanium activity does not seem to be the wetting reactions improving factor, since it is high enough for all Copper-ABA/TiC_x systems due to the titanium alloying of the melt.

An explanation for the rapid wetting of Copper-ABA on $TiC_{0.9}$ coatings could be that the triple line velocity depends on the crystal character of the deposited film (see fig. 4.17). $TiC_{0.9}$ is in the fcc TiC crystallinity interval ($x = 0.6 - 1$), where almost all octahedral interstitial sites of the titanium lattice are filled with carbon atoms and vacancies do not lead to a loss of the fcc TiC crystal structure (see [42] and fig. 4.5 (a) of section 4.1). Most likely, the crystallinity of the $TiC_{x<1}$ reaction product is also fcc TiC (see crystal structures after annealing of TiC_x films in fig. 4.7 of section 4.1). Thus, no structural changes have to occur during wetting at the Copper-ABA/$TiC_{0.9}$ interface. The reservoir of Ti and C atoms at the Copper-ABA/$TiC_{0.9}$ reaction site at the triple line is high enough to produce the $TiC_{x<1}$ reaction product rapidly, while the amount of carbon atoms at the Copper-ABA/$TiC_{0.2}$ (and Copper-ABA/Ti) interface decreases. In the latter cases, carbon atoms need to get in contact with the Cu-Ti melt to start the wetting inducing reaction of eq. 4.1, which occurs either by diffusion within the TiC_x film or by the reaction of eq. 4.2 (dissolution of TiC_x). Further, the crystal structure of the $TiC_{0.2}$ (metastable) and the Ti (hcp) film has to be changed into fcc TiC of the $TiC_{x<1}$ reaction product. Therefore, rapid wetting with the highest spreading velocities can be achieved for TiC_x films already existing in the fcc TiC crystal phase. The wetting behavior of Copper-ABA on the uncoated reference system could significantly be improved by coating of magnetron sputter deposited $TiC_{0.9}$ films.

The crystallinity of CVD-TiC films is fcc TiC (see section 4.1.2). During wetting experiments, CVD-TiC coatings should behave like sputtered $TiC_{0.9}$ films with the same crystal structure. However, they react very slowly and the initial contact angles are higher than in the $TiC_{0.9}$ and in the other TiC_x wetting systems. Most likely, cracks leading to rough surfaces and high film stresses (see previous sections 4.1 and 4.2) inhibit a fast progress of reactive wetting. It is a well-known effect that cracks, grooves and sharp edges influence the wetting behavior of rough surfaces when they are wetted by a liquid [16,201,202]. These barriers generate blocking or even pinning of an advancing triple line leading to a low rate of the wetting reaction.

4.3.2.2 Wetting by Gemco

The spreading behavior of liquid Gemco alloy on uncoated, magnetron sputter deposited $TiC_{0.9}$, $TiC_{0.2}$, Ti and CVD-TiC coated pyrolytic graphite substrates is illustrated in fig. 4.26 (a) visualized as drop base radii $R_\mathrm{L}(t)$. Their velocities are presented in fig. 4.26 (b). Due to constant velocity regimes, spreading is again reaction-limited for all Gemco/TiC_x systems, except the uncoated case, which is non-reactive. The highest velocities were achieved during wetting of $TiC_{0.2}$ and Ti films ($\frac{\mathrm{d}R_\mathrm{L}}{\mathrm{dt}} = 1160$ µm/s and $\frac{\mathrm{d}R_\mathrm{L}}{\mathrm{dt}} = 730$ µm/s, respectively). Their final

drop base radii could not be examined (see figs. 4.24 (c) and (d)). Wetting of $TiC_{0.9}$ films with a velocity of $\frac{dR_L}{dt} = 14$ µm/s was only realized by small Ni-additions in the Gemco alloy, enhancing the wetting activity as discussed above in section 4.3.1. In the case of CVD-TiC again two stages of linear growth of the drop base radius were observed. Thus, a comparison between the spreading behavior of CVD-TiC and the sputtered $TiC_{0.9}$ film (both fcc TiC crystal structure) was again not possible.

The spreading velocity of TiC_x films wetted by the titanium-free Gemco alloy can be improved by increasing the titanium content in the coating. In comparison with Copper-ABA/TiC_x systems, the velocity depends now on the titanium activity (see eq. 4.4), which increases by the titanium concentration in the initial TiC_x film.

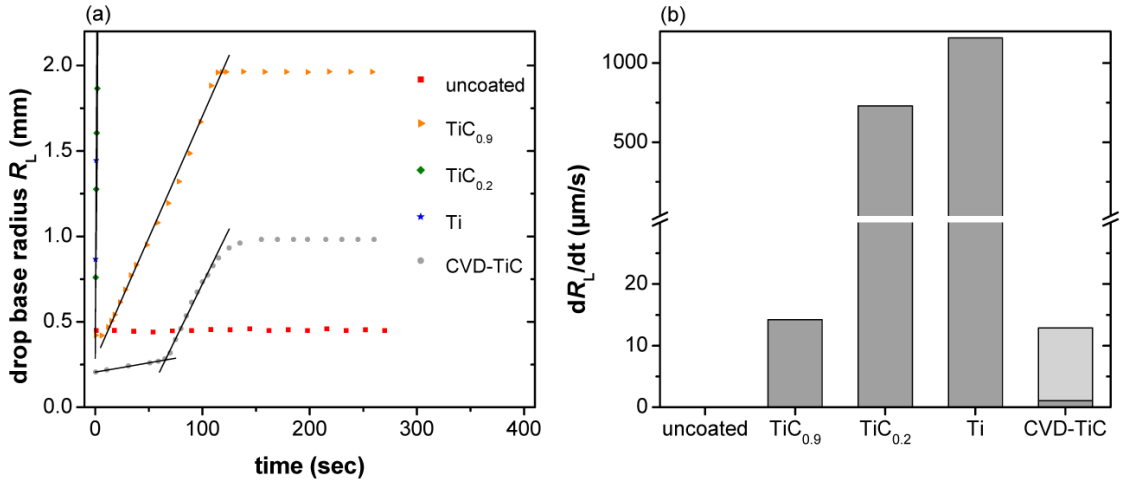

Figure 4.26: Results of wetting experiments using the sessile drop device: (a) drop base radii vs. time of Gemco on uncoated, magnetron sputter deposited $TiC_{0.9}$, $TiC_{0.2}$, Ti and CVD-TiC coated pyrolytic graphite; (b) velocities of the drop base radius (two stages at CVD-TiC)

4.3.3 Summary of wetting experiments

High temperature wetting experiments were performed to examine the wettability characteristics of magnetron sputter deposited TiC_x films wetted by the copper-based brazing alloys Copper-ABA and Gemco. $TiC_{0.9}$ (fcc titanium carbide), $TiC_{0.2}$ (metastable) and Ti (hcp α-titanium) coatings were chosen to represent each crystallinity zone in the range of $0 \leq x \leq 1$. CVD-TiC films and uncoated graphite substrates (reference samples) were tested as well.

In case of the Cu-Ti alloy Copper-ABA, initial contact angles lower than 90° were obtained for all magnetron sputtered TiC_x films, but not for the CVD-TiC and the reference sample. Due to the high titanium activity in the Copper-ABA alloy, every sample was wetted at the same low final contact angle ($\theta_F = 6°$). These processes are based on reactive wetting. In all systems, a high-wettable reaction product was formed at the wetting interface: the thermodynamically favored $TiC_{x<1}$. Its stoichiometry was evaluated by thermodynamic calculations (Thermo-Calc DICTRA) and determined to $x = 0.6$, its crystal structure is fcc titanium carbide. The significantly highest spreading velocities of Copper-ABA droplets were achieved for magnetron sputter deposited $TiC_{0.9}$ films. Thus, the wetting behavior of Copper-ABA on carbon materials can be improved by coating of TiC_x films, which already exist in the

face-centered cubic TiC crystal phase ($x = 0.6 - 1$).

Wetting in Gemco/TiC_x systems strongly depends on the activity of titanium atoms in the melt. High spreading velocities and low initial contact angles of titanium-free Gemco droplets were observed for magnetron sputter deposited $TiC_{0.2}$ and Ti films. TiC_x films close to the composition of pure titanium are characterized by high titanium activities. Thus, a wetting promoting behavior using the Gemco alloy was found for films with a high titanium concentration ($TiC_{x\to 0}$). For low-titanium containing films $TiC_{x\to 1}$ the formation of the wettable $TiC_{x<1}$ reaction product was only achieved by the alloying element nickel, which increased the activity of titanium in the melt. A poor wetting behavior with constant contact angles higher than 90° was observed in the Gemco/non-coated graphite system due to the absence of reactive titanium.

The wetting behavior of the CVD-TiC films was inhibited by stress-induced deposition defects (cracks). Poor wetting of Copper-ABA and Gemco was observed (high initial contact angles, low spreading velocities). The comparison of low-stress magnetron sputter deposited TiC_x films with CVD-TiC coatings shows the importance of stress optimization for a good wetting performance.

The wettability tests have shown that magnetron sputter deposited TiC_x films in the range of $x = 0.6 - 1$ improve the Copper-ABA wetting performance. They are possible candidates to be implemented in the Copper-ABA brazing technology for producing thermally resistant CFC/Cu components.

On the other side, TiC_x films enable the formation of CFC/Cu braze joints using the non-reactive Gemco alloy. Here, improved wetting was achieved for films close to the composition of pure titanium ($TiC_{x\to 0}$). Thus, brazing by the Gemco alloy and using a Ti-rich TiC_x interlayer can be proposed as an option for the CFC/Cu brazing technology using Copper-ABA. The Gemco/$TiC_{x\to 0}$ systems exhibit good wetting characteristics and, in particular, melting temperatures lower than for wetting with Copper-ABA ($T_{melt,\,Copper-ABA} = 1024$°C, $T_{melt,\,Gemco} = 975$°C).

5 Implementation of TiC_x films in brazed CFC/Cu components

This chapter describes the application of thin TiC_x films in the manufacturing process of flat tile divertor components consisting of the armor material CFC NB31 and copper-based heat sinks. The aim is to analyze the impact of their wetting promoting behavior (see section 4.3) on the well-established Copper-ABA brazing process in order to improve the bonding strength at the CFC/Cu interface. TiC_x modified compounds were tested under thermomechanical loads such as interfacial shear stresses or high heat fluxes in order to evaluate their implemention in CFC armored flat tile divertor applications.

For these investigations TiC_x coatings in the range of $0 \leq x \leq 1$ were produced by magnetron sputter deposition. The same films as for the wetting experiments in section 4.3 (one film of each crystallinity zone) were chosen: face-centered cubic (fcc) $TiC_{0.9}$, $TiC_{0.2}$ (metastable) and hexagonal closest packed (hcp) Ti (see fig. 4.17 of section 4.3). They were deposited on CFC NB31 surfaces perpendicular to the ex-pitch direction that will be used for brazing. In addition, CVD-TiC coatings were included as an example, that demonstrates the importance of a stress-optimized and defect-free TiC_x film structure.

Section 5.1 characterizes the interfaces of TiC_x modified CFC/Cu joints, brazed by Copper-ABA, as they were used for the subsequent shear stress and high heat flux tests in section 5.2 and 5.3.

5.1 Interface characteristics of TiC_x modified CFC/Cu braze joints

5.1.1 Penetration of CFC pores by the brazing alloy

Optical microscope images of the TiC_x modified CFC/Cu braze joints are presented in fig. 5.1. They are representative images characterizing each cross-section. They show, whether TiC_x wetting promoting films (especially the rapid-wetting $TiC_{0.9}$, see section 4.3) improve the penetration of CFC pores by the liquid brazing alloy Copper-ABA. In general, a good wetting and adhesion behavior could be achieved in all cases, except CVD-TiC. However, only pores of $TiC_{0.9}$ coated CFC were penetrated to the full extent. The samples '$TiC_{0.2}$' and 'Ti' and the uncoated reference sample exhibit several pores, which are not or only half filled by the brazing alloy Copper-ABA. The good penetration of $TiC_{0.9}$ coated pores is in accordance with the Copper-ABA wetting results of section 4.3. By contrast, gaps between CFC and the Ti-rich reaction interface indicate that non-optimized CVD-TiC coatings lead to poor adherence after solidification of the liquid alloy (see fig. 5.1 (e)).

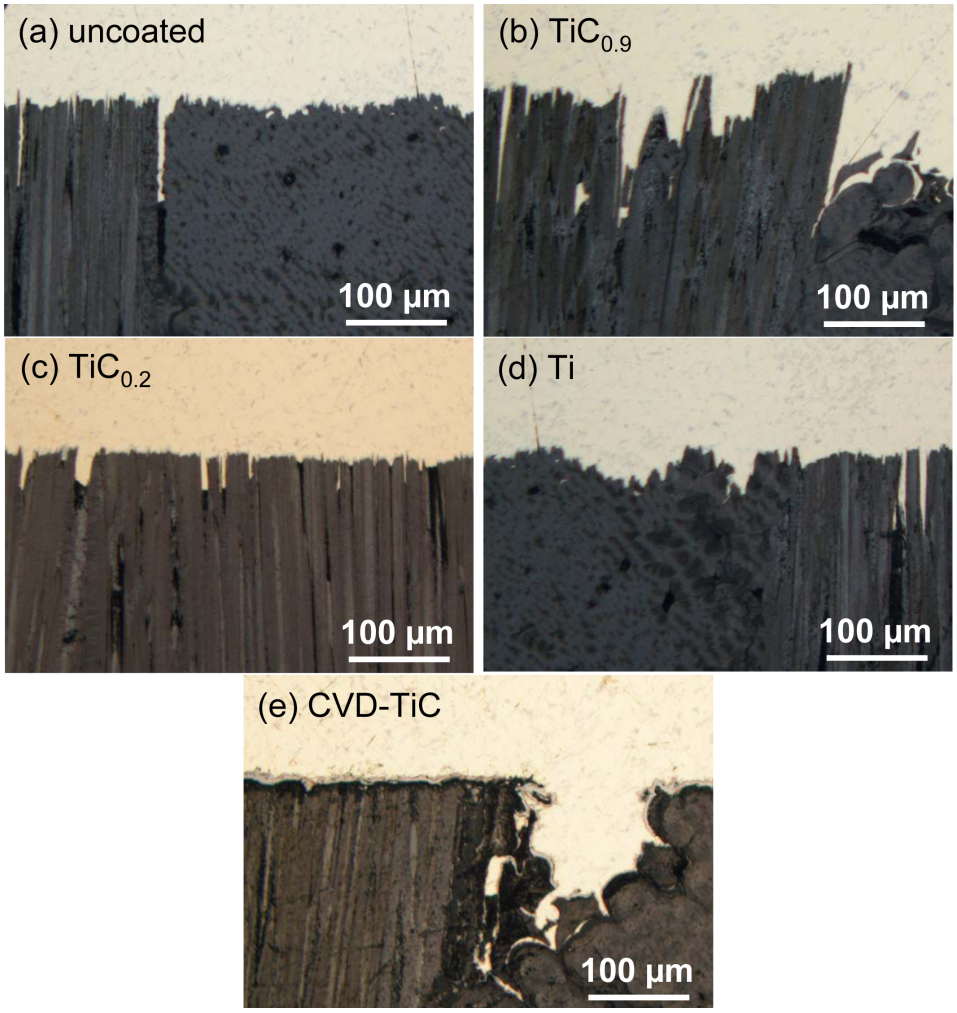

Figure 5.1: Penetration behavior of CFC NB31 pores by the Copper-ABA alloy at TiC_x modified CFC/Cu braze joints, (a) uncoated, (b) magnetron sputter deposited $TiC_{0.9}$, (c) $TiC_{0.2}$ and (d) Ti and (e) CVD TiC

5.1.2 Reaction zone analysis

During TiC_x modified CFC/Cu brazing processes, chemical reactions take place between the brazing alloy Copper-ABA and TiC_x coated carbon (relevant reactions were described in section 4.3.1.1). Chemical analyses of these reaction zones were performed by EDX linescans using Focussed gallium-Ion Beam (FIB) sputtered cross-sections. SEM images and EDX intensities of these investigations are presented in figs. 5.2 to 5.7 for the uncoated, $TiC_{0.9}$, $TiC_{0.2}$, Ti and the CVD-TiC system, respectively.

Both, the formation of new interlayers and the modification of existing TiC_x films were observed. For every TiC_x system titanium signals were only found within the thin reaction product interlayers at the carbon/Copper-ABA interfaces. The diffusion of titanium from the brazing alloy towards carbon was necessary in order to allow the formation of the Ti-C reaction product that joins copper with carbon. In addition, Si from the Copper-ABA alloy diffused to the reaction zone, too. It was found only in a Ti-Si phase.

The reaction zone can be separated into four different subzones: (1) the Cu-alloy, (2) a

Ti-Si rich zone, (3) a Ti-C rich zone (substoichiometric titanium carbide interlayer as predicted in section 4.3.1) and (4) the carbon bulk material. At any system, the Ti-C rich zone is located next to the carbon bulk. Fine Cu agglomerations are observed at the interface between (3) and (4), except for the CVD-TiC system, and may probably be allocated to Cu-Ti intermetallics.

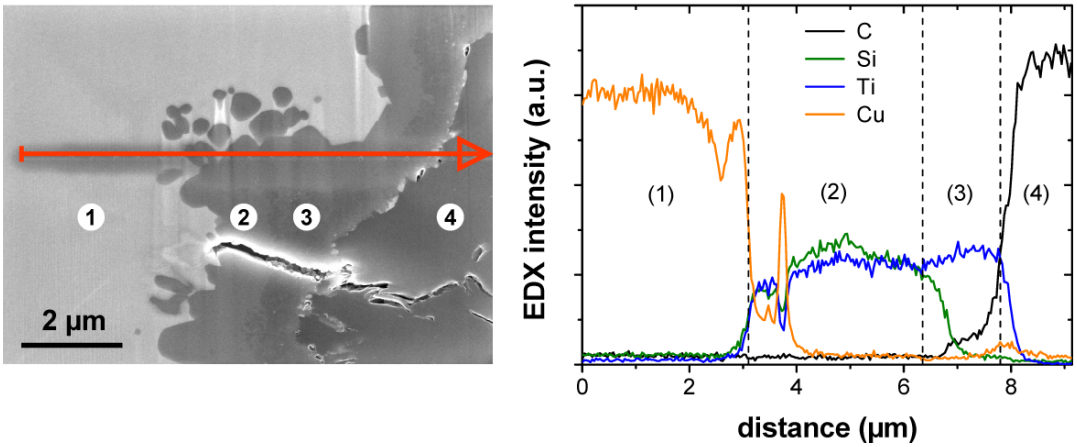

Figure 5.2: EDX linescan of the reaction zone after Copper-ABA brazing of copper to uncoated carbon at 1050°C; (1) Cu-alloy, (2) Ti-Si rich zone, (3) formed Ti-C rich zone and (4) carbon bulk

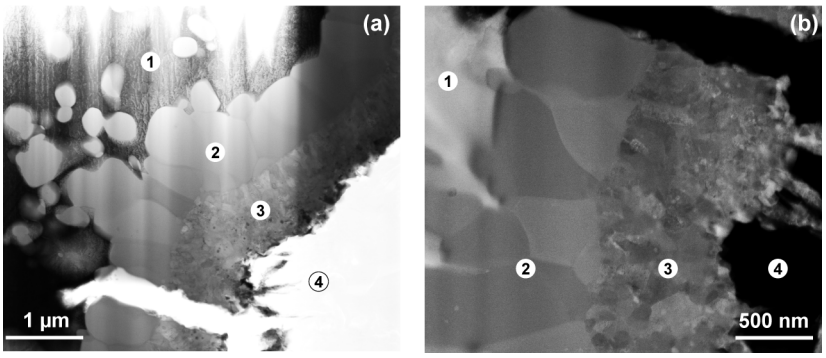

Figure 5.3: Scanning Transmission Electron Microscope (STEM) images of the reaction zone after Copper-ABA brazing of copper to uncoated carbon at 1050°C; (1) Cu-alloy, (2) Ti-Si rich zone, (3) formed Ti-C rich zone and (4) carbon bulk; (a) bright-field mode, (b) dark-field mode

In the case of brazing without additional TiC_x layer (reference sample, see fig. 5.2), the thickness of the zones (2) and (3) is ~1 µm, respectively. Scanning Transmission Electron Microscope (STEM) viewgraphs of these zones are presented in fig. 5.3 with higher resolution and magnification. Fine dispersed grains with different orientations and sizes in the range of 50 nm to 200 nm are observed in the Ti-C rich zone, whereas grains of the Ti-Si rich zone are larger (sizes of up to 1 µm) and even go from one end of the zone to the other. Some grains of zone (2) extend into zone (1).

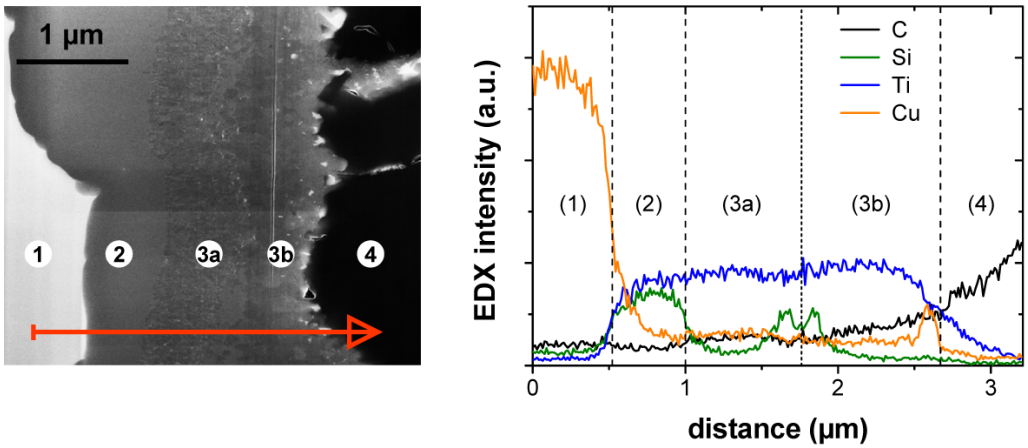

Figure 5.4: EDX linescan of the reaction zone after Copper-ABA brazing of copper to magnetron sputter $TiC_{0.9}$ coated carbon at 1050°C; (1) Cu-alloy, (2) Ti-Si rich zone, (3a) formed Ti-C rich zone, (3b) initial sputter deposited $TiC_{0.9}$ film and (4) carbon bulk

Brazing with a $TiC_{0.9}$ layer exhibits two Ti-C rich layers: a new layer (3a), which is formed by reactive wetting and the initially deposited 500 nm thin $TiC_{0.9}$ film (3b) (see fig. 5.4). The EDX intensities of the carbon signals of zone (3a) are lower than of zone (3b). In all probability, zone (3a) is the substoichiometric titanium carbide reaction product, which was predicted in section 4.3 (noted as $TiC_{x<1}$). Unfortunately, a quantitative EDX analysis (in order to determine the exact composition of zone (3a)) was not possible, because too many interfering carbon signals existed (re-deposition of carbon during ion-polishing of the cross-section surface). Some Ti-Si rich areas remain at the interface between zone (3a) and (3b), as indicated by Si-peaks in the EDX diagram.

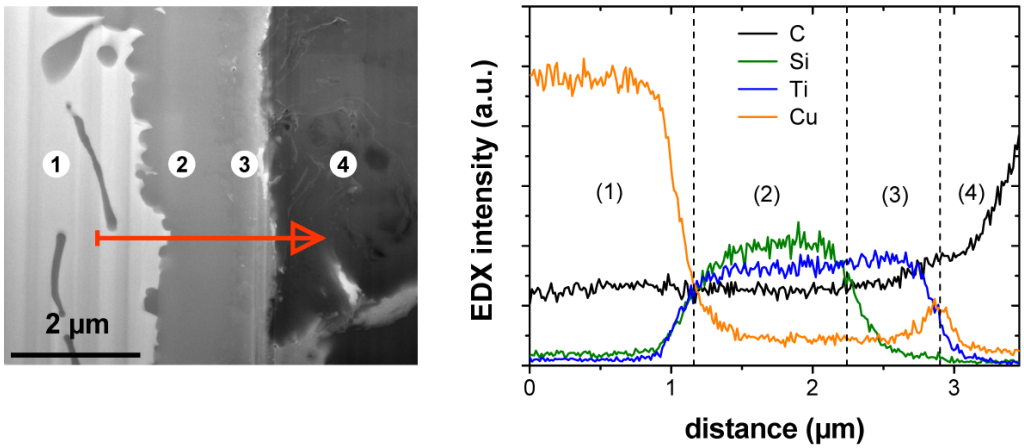

Figure 5.5: EDX linescan of the reaction zone after Copper-ABA brazing of copper to magnetron sputter $TiC_{0.2}$ coated carbon at 1050°C; (1) Cu-alloy, (2) Ti-Si rich zone, (3) Ti-C rich zone and (4) carbon bulk

As seen in fig. 5.5, the reaction zone after Copper-ABA brazing with a $TiC_{0.2}$ layer does not exhibit an additional Ti-C rich interlayer, which is visible as zone (3a) for $TiC_{0.9}$ (see fig. 5.4). Zone (3) includes the previously deposited 500 nm thick $TiC_{0.2}$ film, which had a distorted

crystal structure before brazing (see section 4.1.2). In contrast to $TiC_{0.9}$, the crystallinity of the $TiC_{0.2}$ film changes its crystal structure (into fcc TiC) during the brazing process and the film reacts at the Copper-ABA/$TiC_{0.2}$ interface into substoichiometric titanium carbide (see lower carbon signals towards zone (2) in fig. 5.5).

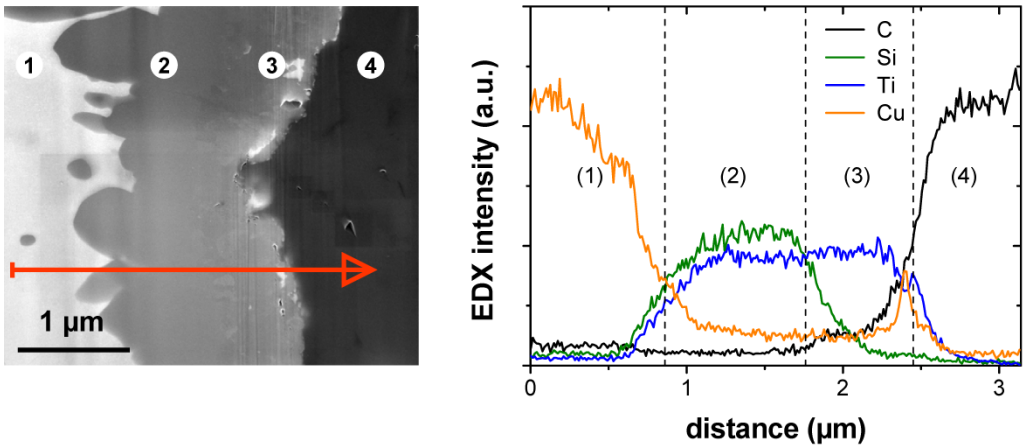

Figure 5.6: EDX linescan of the reaction zone after Copper-ABA brazing of copper to magnetron sputter Ti coated carbon at 1050°C; (1) Cu-alloy, (2) Ti-Si rich zone, (3) Ti-C rich zone and (4) carbon bulk

The resulting reaction interlayer after brazing with an initial sputter deposited Ti film (see fig. 5.6) seems to be exactly the same as with $TiC_{0.2}$.

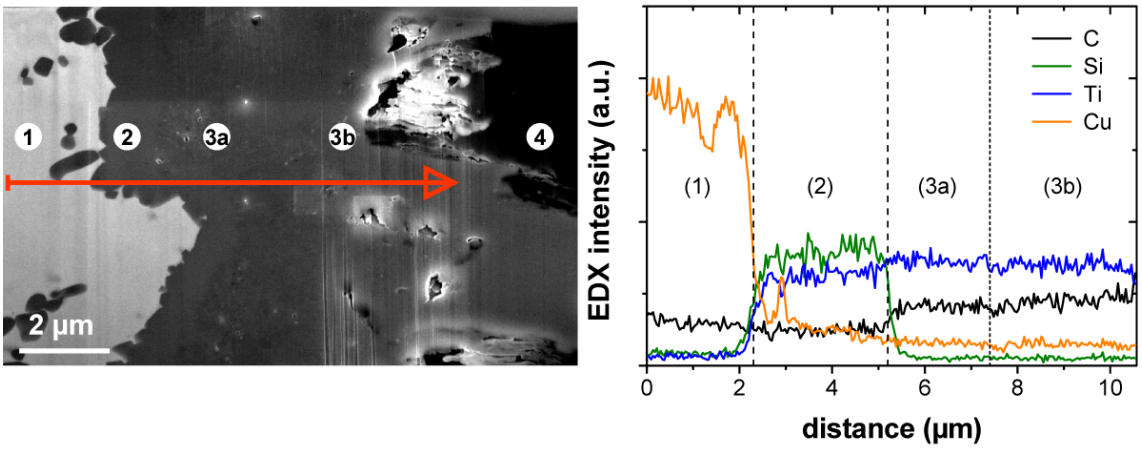

Figure 5.7: EDX linescan of the reaction zone after Copper-ABA brazing of copper to CVD-TiC coated carbon at 1050°C; (1) Cu-alloy, (2) Ti-Si rich zone, (3a) formed Ti-C rich zone, (3b) initial deposited CVD-TiC film and (4) carbon bulk

The reaction zone after Copper-ABA brazing with a CVD-TiC film is presented in fig. 5.7. The image shows that pores of the deposited CVD-TiC film (see fig. 4.12) still exist after the brazing process. Besides, a reaction zone was detected, which coincide with the magnetron sputter deposited $TiC_{0.9}$ sample (see fig. 5.4). Again, two Ti-C rich zones (3a) and (3b) could be detected. Thus, it can be said that the same processes occur with sputtered $TiC_{0.9}$ and

with CVD-TiC films during Copper-ABA brazing.

5.2 Shear strength properties of TiC_x modified CFC/Cu braze joints

The bonding strength of the TiC_x modified copper to CFC assemblies were determined by shear strength tests following standards like ASTM D905-03. Shear strength tests are of high relevance, because thermal stress causes shear in the CFC/Cu interface in divertor modules under operation. These shear loads are induced by different thermal expansion coefficients of the CFC armor tiles and the copper-based cooling structure (see section 1.2). All mechanical characterizations have been performed at room temperature.

5.2.1 Tests with as-received CFC

TiC_x modified CFC/Cu braze joints were submitted to shear strength tests using a type of the so-called double lap configuration (test with Cu/CFC/Cu sandwich-like compounds). Fig. 5.8 shows typical shear strength values of Cu/CFC/Cu assemblies using as-received CFC NB31. It compares the shear strength properties found for TiC_x modified joints and the reference joints (uncoated).

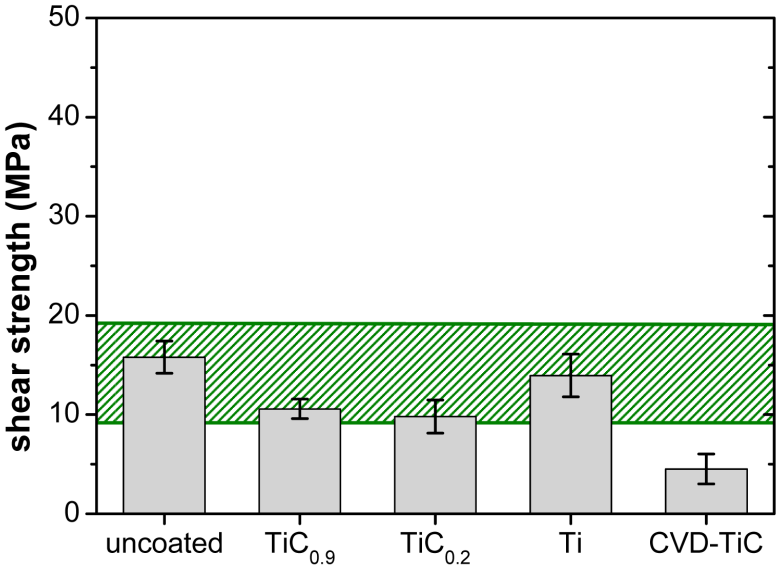

Figure 5.8: Shear strength of uncoated, magnetron sputter-TiC_x and CVD-TiC coated CFC/Cu interfaces brazed by Copper-ABA, using as-received CFC NB31; the shear strength range of CFC NB31, according to Schlosser et al. [123], is highlighted as green area

The shear strengths of the samples modified by sputter deposited ($TiC_{0.9}$, $TiC_{0.2}$ and Ti) films and the reference samples are in the range of 13 ± 4 MPa. The values are slightly higher at uncoated and Ti-coated samples comparing them to samples modified by $TiC_{0.9}$ and $TiC_{0.2}$ films. However, the differences are within the error bars so that it can be maintained that all

these values are in the same order of magnitude. Statements, whether sputter deposited TiC_x films improve the shear strength of CFC/Cu interfaces, cannot be derived.

Compared to any other sample of fig. 5.8, the shear strength of CVD-TiC modified Cu/CFC/Cu braze joints was much lower (∼5 MPa). Various cracks and pores within the CVD-TiC film (see sections 4.1 and 5.1) may lead to non-adhesive CFC/Cu interfaces that are responsible for these low values. Thus, the bonding strength depends on the film quality and the manufacturing process. Unlike CVD-TiC coatings, low-stress and crack-free magnetron sputter deposited TiC_x films did not reduce the CFC/Cu shear strength.

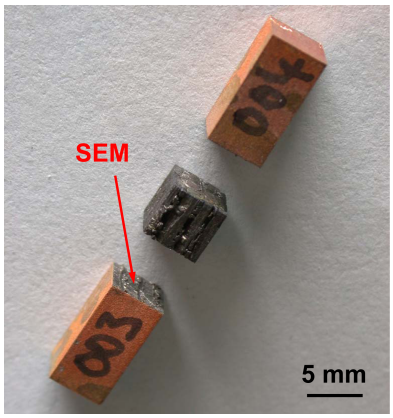

Figure 5.9: Selected shear strength test sample after the test. This sample was brazed with a $TiC_{0.9}$ film. Rests of CFC NB31 fibers remain on the copper fragments.

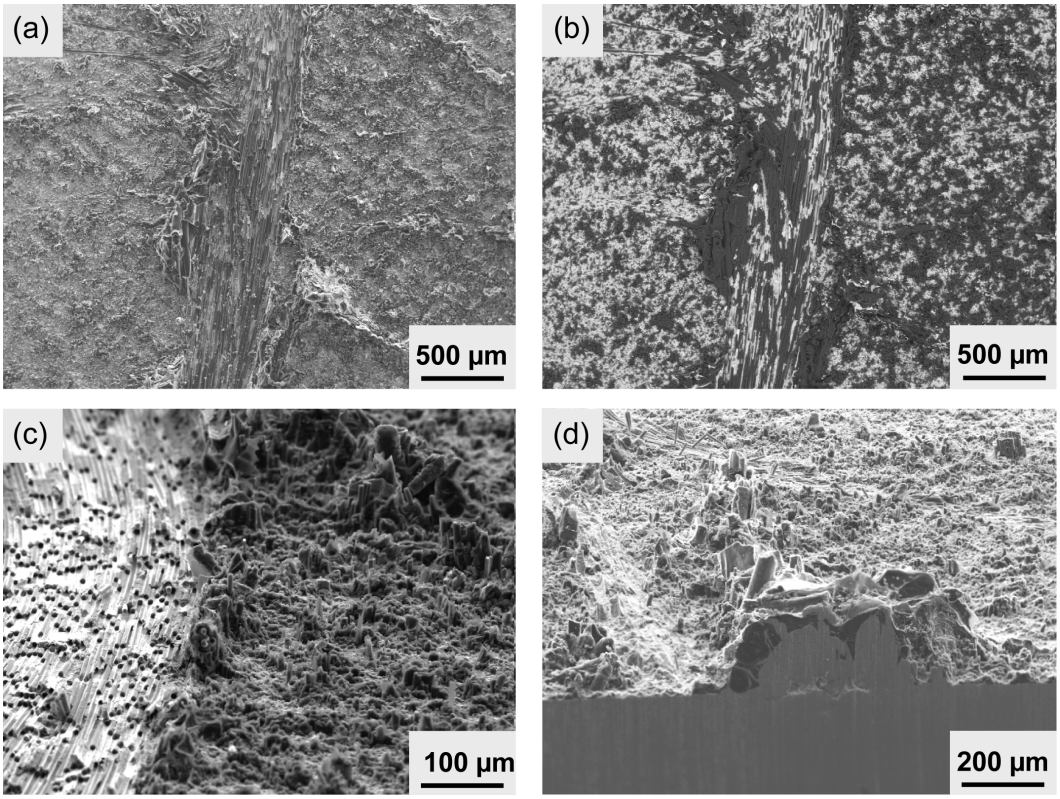

Figure 5.10: SEM images of a typical fracture surface after the shear strength tests with TiC_x modified CFC/Cu braze joints, taken at a '$TiC_{0.9}$' sample. They show the surface of the copper fragment with remaining CFC fiber pieces, (a), (c) and (d) in the SE mode and (b) in the BSE mode (same location as (a)). A cross-section is shown in (d). The images (c) and (d) are with tilted view.

All shear strength values (except for CVD-TiC) are within the range of the interlaminar shear strength τ_{NB31} of CFC NB31 (τ_{NB31} = 15 MPa [13] and τ_{NB31} = 9 - 19 MPa [123]). It might lead to the assumption that the fracture occurred not at the interface, but only inside the CFC. Therefore, fracture surfaces of the copper fragments (see fig. 5.9) were characterized.

The SEM images of these surfaces are very similar for all samples. Therefore, only the fracture surface of a $TiC_{0.9}$ modified Cu/CFC/Cu shear strength test sample is shown in fig. 5.10. The cross-section of fig. 5.10 (d) demonstrates that the fracture occurred at the interface. However, rests of cracked ex-PAN and ex-pitch fibers are still visible showing that the fracture is also in the CFC, but close to the CFC/Cu interface. Fig. 5.10 (b) (BSE mode) illustrates the same location on the fracture surface as fig. 5.10 (a) (SE mode). SE enhances the topography and BSE the material contrast. The bright areas of fig. 5.10 (b) are identified to be composed mainly of copper, the dark areas of carbon. This image shows a homogeneous distribution of areas cracked at the CFC/Cu interface or in CFC fibers. Copper infiltrations into CFC pores could also be observed as 'humps' on the fracture surface (see fig. 5.10 (d)).

Upon these observations, no statements can be made, whether the values of fig. 5.8 (without CVD-TiC) represent the shear strength of CFC NB31 fibers, which cracked close to the interface, or the interfacial shear strength of the TiC_x modified CFC/Cu interfaces. In order to solve this question, similar tests were performed, but with oxygen plasma treated CFC surfaces.

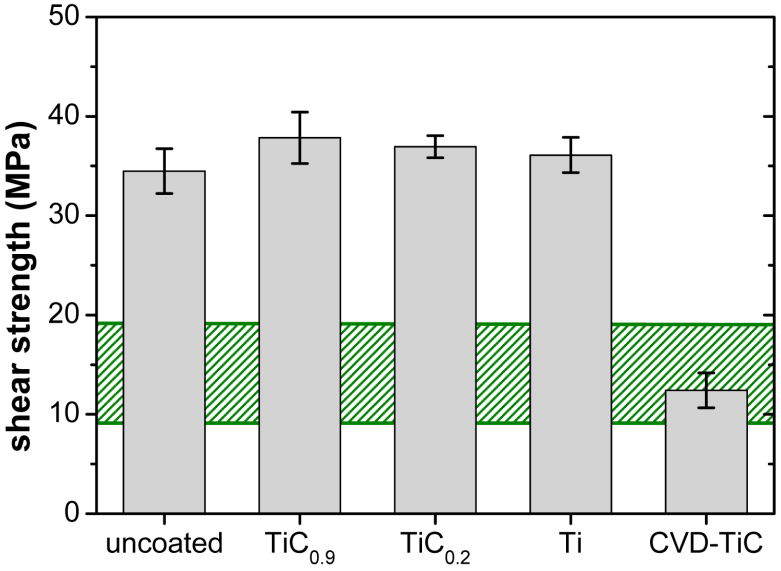

Figure 5.11: Shear strength of uncoated, magnetron sputter-TiC_x and CVD-TiC coated CFC/Cu interfaces brazed by Copper-ABA, using oxygen plasma treated CFC NB31; the shear strength range of CFC NB31, according to Schlosser et al. [123], is highlighted as green area

5.2.2 Tests with oxygen plasma treated CFC

Shear strength tests with TiC_x modified Cu/CFC/Cu braze joints were repeated under the same conditions as in section 5.2.1, but using oxygen plasma treated CFC NB31. The intensive plasma induced erosion at a bias voltage of -100 V for 20 hours leads to an increase of the CFC surface roughness and to an opening of small pores (see images in section 3.6). The aim is to

achieve a better anchorage of copper to NB31, increase the size of the strengthened bonding area and promote the bonding adhesion and strength.

The results are presented in fig. 5.11. In any case, the shear strength of the interfaces exceeds the corresponding values of the tests performed with as-received CFC NB31 by a factor of 2 and more. Differences between uncoated and TiC_x-sputtered Cu/CFC/Cu assemblies were not detected.

A mechanical modification of CFC surfaces at NB31 to copper assemblies has also been reported by Schedler et al. [22]. Instead of roughening by oxygen plasma and brazing with different TiC_x layers they used the AMC bonding technique (see section 1.3) in combination with a micro-machining process of the CFC surface. With this method shear strength values on the same level illustrated in fig. 5.11 could be achieved.

SEM images of the fracture surfaces tested in fig. 5.11 exhibit the same appearance. They are shown in fig. 5.12 for a '$TiC_{0.9}$' sample. Again, rests of cracked ex-PAN and ex-pitch fibers are still visible on the copper fragment. However, ex-PAN fibers parallel to the CFC/Cu interface stick to the copper fragment in a greater extent as they do in fig. 5.10 for as-received CFC samples (see BSE image, fig. 5.12 (b)). This is related to a better anchorage of CFC to copper due to the opening of CFC pores caused by the oxygen plasma treatment before brazing. More and larger copper infiltrations into CFC pores generated a strengthening of the bonding area at the CFC/Cu interface. Thus, the CFC to copper shear strength has increased.

The generally higher values found for the oxygen plasma treated CFC/Cu braze joints lead to the conclusion that this joint is more robust compared to the solution applied for as-received NB31. By this way, higher values than the interlaminar shear strength τ_{NB31} of CFC NB31 can be achieved with the shear strength setup used for this work. Therefore, the interfacial shear strength of the TiC_x modified CFC/Cu interfaces was measured in all cases, even for samples with as-received CFC.

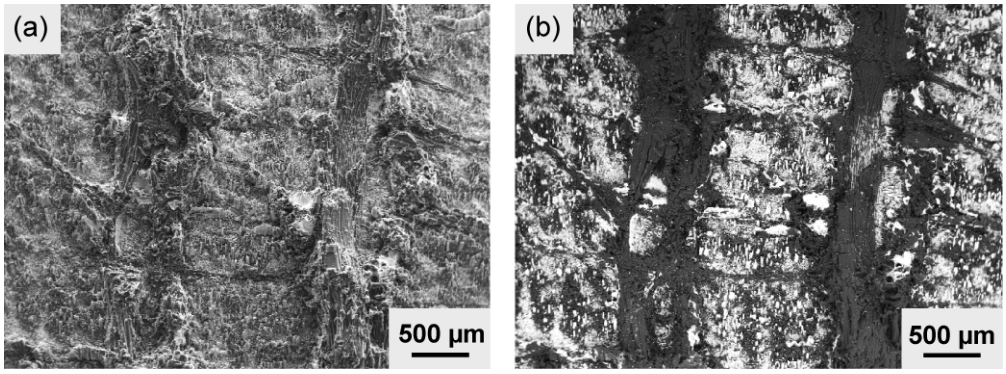

Figure 5.12: SEM images of a typical fracture surface after the shear strength tests with oxygen plasma treated and TiC_x modified CFC/Cu braze joints, taken at a '$TiC_{0.9}$' sample. They show the surface of the copper fragment with remaining CFC fiber pieces, (a) in the SE mode and (b) in the BSE mode (same location as (a)).

5.2.3 Summary of shear strength tests

TiC_x modified copper to CFC NB31 assemblies, which have been brazed with the commercial brazing alloy Copper-ABA were subjected to shear strength tests. They have shown for all investigations, that the modification by thin TiC_x films do not increase the CFC/Cu bonding strength. An increase of the shear strength by a factor of 2 and more was only achieved by

changing the roughness of the initial CFC surface. A treatment with biased oxygen plasma provided the opening of CFC pores by physical and chemical erosion. This had a beneficial impact on the anchoring effect of the liquid brazing alloy in the CFC. By this way, a bonding strength was achieved comparable to experiments performed with other CFC/Cu bonding technologies. For braze joints modified by non-optimized CVD-TiC coatings low shear strength values have been expected and were measured due to their non-adhesive behavior after brazing (see section 5.1).

Mechanical testing of copper to CFC assemblies is an inadequate method to test and validate different TiC_x wetting promoting films in CFC/Cu braze joints.

5.3 High heat flux tests of TiC_x modified CFC/Cu/CuCrZr flat tile mock-ups

The next step was to demonstrate the feasibility of implementing TiC_x wetting promoters in actively cooled flat tile divertor mock-ups and to analyze and validate the overall thermal performance of the component under high heat flux (HHF) loadings. The goal of long cycle thermomechanical fatigue tests was to improve the long-term bonding quality between the plasma facing material CFC and the cooling structure by modification with thin TiC_x wetting promoting films. They were coated on oxygen plasma treated CFC NB31. The plasma induced erosion process was adopted to increase the wettable CFC surface (opening of the pores) and thus to achieve a high stability of the interface against thermal stress. The TiC_x modified actively water-cooled CFC/Cu/CuCrZr flat tile mock-ups were brazed successfully and subsequently prepared for screening and thermal cycling tests in the high heat flux facility GLADIS.

5.3.1 Finite Element Analysis (FEA)

Thermal 2D FEA was performed using the commercial finite element suite ABAQUS [162] in order to estimate the expected temperature profile within the component during high heat flux testing. The temperature was calculated for the CFC tile surface ($T_{surface}$), the thermocouples placed above the cooling channel in bulk CFC, 2.5 mm under the exposed surface (T_{TC1}) and in the CuCrZr cooling structure, 10 mm under the exposed surface (T_{TC2}), the brazed interfaces ($T_{CFC/Cu}$ and $T_{Cu/CuCrZr}$) and for the cooling tube wall (T_{wall}) (see fig. 5.13 (a)).

As an example, the temperature evolution as a function of time within the flat tile mock-up at a heat flux of 10 MW/m^2 is shown in fig. 5.14 (a). The simulation was performed for a cycle of 10 seconds pulse duration and 50 seconds cooling. After 10 seconds, all temperatures reach a steady state. As indicated in fig. 5.14 (b), the temperature decreases with decreasing distance to the cooling channel. Fig. 5.13 (b) shows the temperature distribution of the CFC/Cu/CuCrZr flat tile mock-up for 10 MW/m^{2}at steady state conditions. The temperature in the CFC flat tile was calculated to be laterally homogeneous although the edges are farthest away from the cooling channels. Fig. 5.14 (c) presents the calculated steady state temperature at dedicated heat fluxes between 2 and 26 MW/m^2, which serves as basis for comparison with the experimental temperature data. In general, the temperatures increase almost linearly with increasing heat fluxes. The temperature evolution of T_{wall}, T_{TC2}, $T_{Cu/CuCrZr}$ and $T_{CFC/Cu}$ indicate at ~14 MW/m^2 a decrease of the slope of the temperature resulting in a smaller temperature increase at higher heat fluxes than at the CFC surface and at ther-

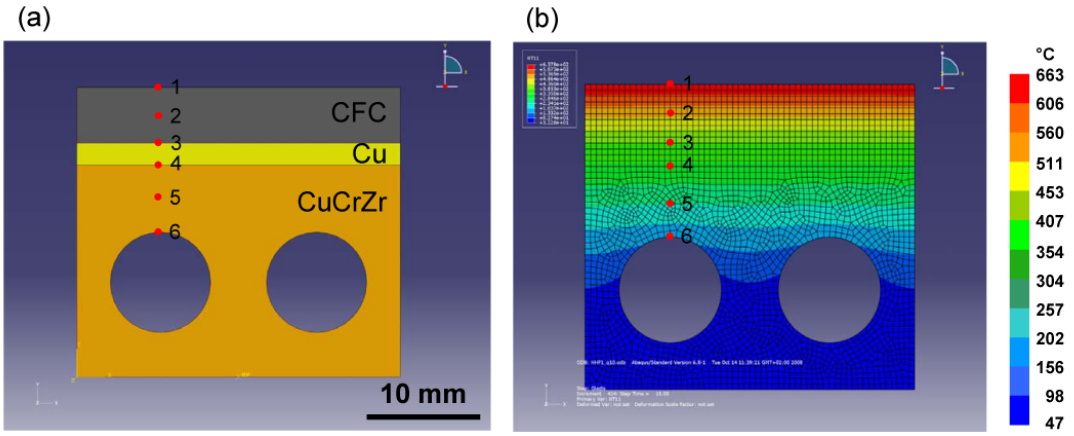

Figure 5.13: Temperature distribution plot of the 2D cross-section of the CFC/Cu/CuCrZr flat tile mock-up at a heat flux of 10 MW/m^2 and steady state conditions; (1) CFC surface, (2) thermocouple 1 (TC1), (3) CFC/Cu interface, (4) Cu/CuCrZr interface, (5) thermocouple 2 (TC2), (6) cooling tube wall

mocouple TC1. Here, the heat transfer process at the cooling channel wall changes from the forced convection regime into the partial sub-cooled boiling regime resulting in a higher heat exchange coefficient α.

A maximum allowed temperature for steady state conditions characterizes each material. Regarding the alloys used for brazing a theoretical heat flux maximum was determined to ~22 MW/m^2 (see fig. 5.14 (c)), because the temperature of the Copper-ABA brazed CFC/Cu interface, $T_{CFC/Cu}$, reaches 80% of the Copper-ABA melting temperature ($T_{limit,Copper-ABA}$) at that heat flux. Going higher would degrade the interface strength, which can lead to a detachment of the heat resistant CFC tiles. $T_{limit,Gemco}$ would not be achieved at heat fluxes below 26 MW/m^2. The maximum temperature in Cu is set to 550°C ($T_{limit,Cu}$). This value results from thermal shock tests performed with specimens at this temperature with no tile detachment. The maximum temperature in CuCrZr is set to 450°C ($T_{limit,CuCrZr}$), a temperature from which this material starts losing its material strength. Both limits for Cu and CuCrZr are reported in [122]. Calculations show that the maximal temperature in CuCrZr and in Cu at 10 MW/m^2 represents 77% of $T_{limit,CuCrZr}$ and 74% of $T_{limit,Cu}$, respectively. At 12 MW/m^2, they already reach 92% of $T_{limit,CuCrZr}$ and 88% of $T_{limit,Cu}$, respectively. At heat fluxes higher than ~13 MW/m^2 the CuCrZr cooling structure has to withstand temperatures higher than 450°C. The design provides a sufficient margin to operate the mock-ups within the heat flux requirements of WENDELSTEIN 7-X (10 MW/m^2). To achieve higher heat fluxes, a CFC armor material thicker than 5 mm, as used in the current work, should be adopted for future developments to reduce the temperature in the CuCrZr cooling structure.

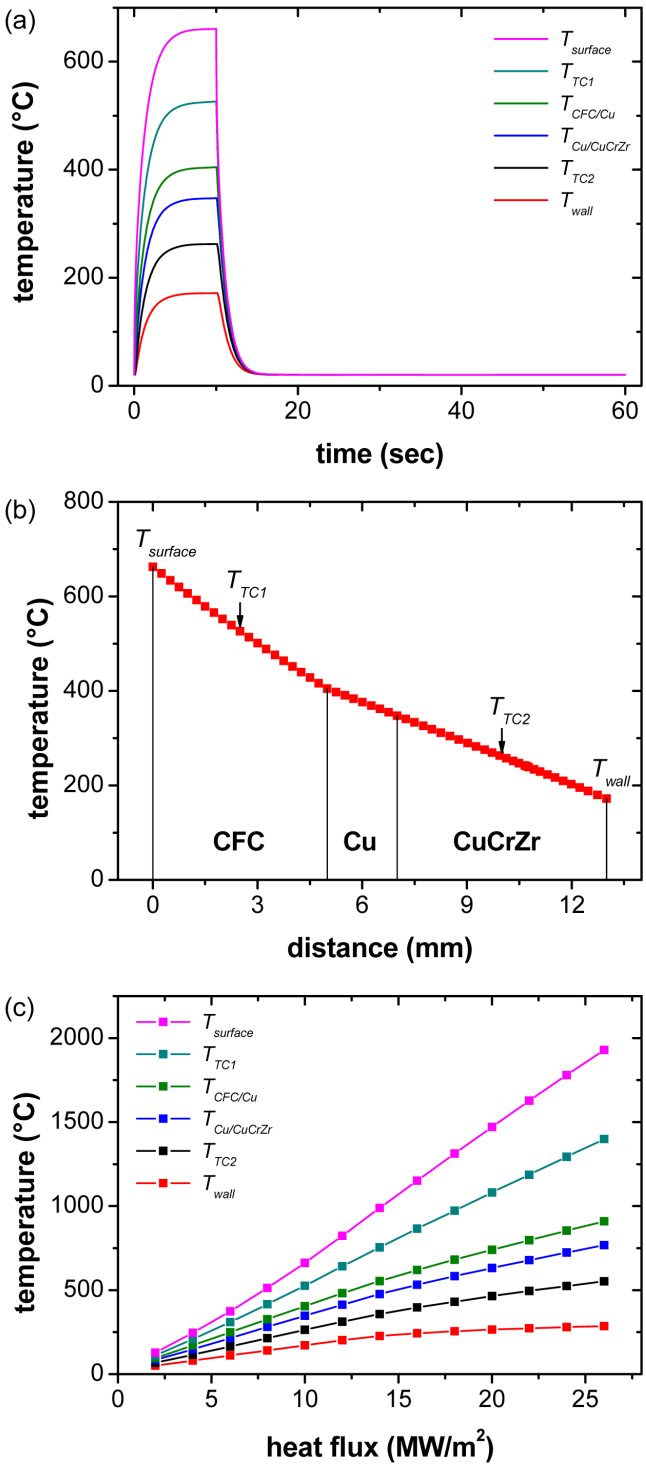

Figure 5.14: (a) Temperature evolution as function of time within the CFC/Cu/CuCrZr flat tile mock-up at a heat flux of 10 MW/m^2 for one heat cycle of 10 s pulse duration and 50 s cooling,
(b) Temperature evolution over the distance from the CFC surface to the cooling channel at a heat flux of 10 MW/m^2 (steady state),
(c) Expected temperatures of the flat tile mock-up at the CFC surface, at the thermocouples, at the interfaces and at the CuCrZr cooling tube wall in dependence of different heat fluxes calculated by ABAQUS

5.3.2 Temperature analysis of the heat-loaded TiC_x mock-ups

Screening tests were performed on the actively cooled TiC_x modified CFC/Cu/CuCrZr flat tile mock-ups to estimate the overall thermal performance under high heat flux loadings from 2 to 15 MW/m^2. Fig. 5.15 presents the temperature evolution of the mock-ups with increasing heat flux load at the CFC tile surface and at the thermocouples. These compounds withstood 10 MW/m^2 without any crucial bonding defects, even the increase to 15 MW/m^2 did not lead to a weakening of the involved materials and bonding interfaces.

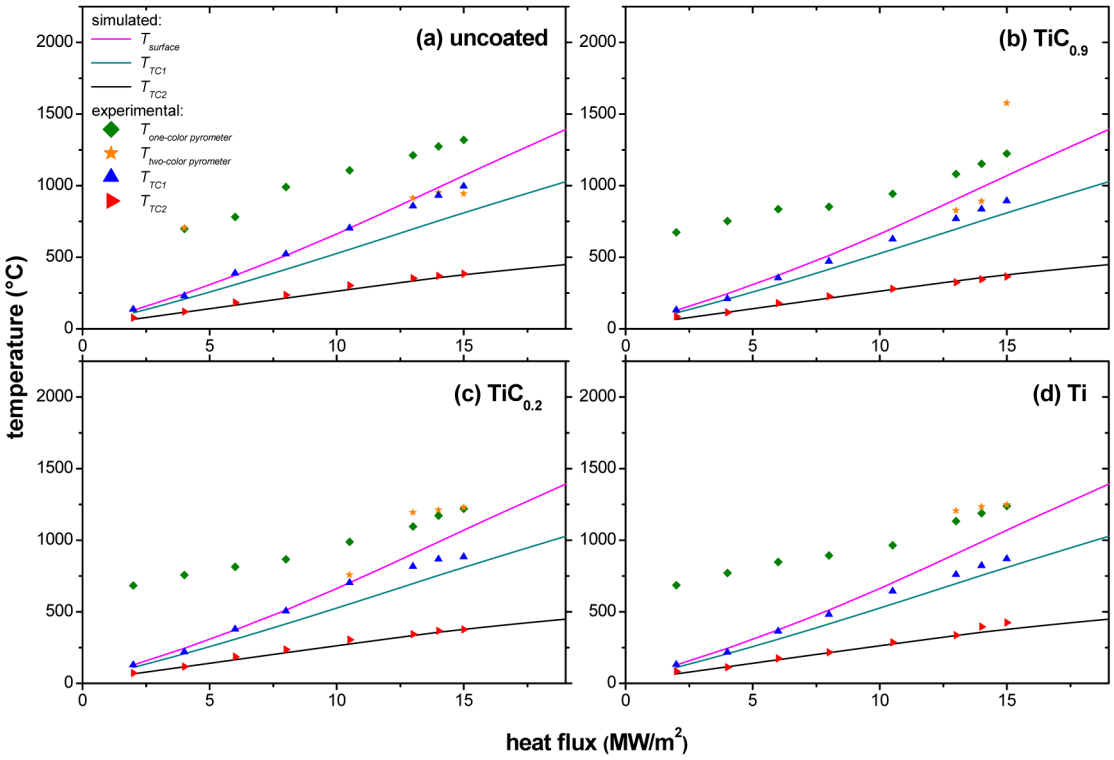

Figure 5.15: Estimated temperatures of infrared camera, pyrometer and installed thermocouples within CFC tile #3 of each CFC/Cu/CuCrZr flat tile mock-up in dependence of different heat fluxes compared with the surface and thermocouple temperatures calculated by ABAQUS, for (a) non-, (b) $TiC_{0.9}$, (c) $TiC_{0.2}$ and (d) Ti modified components

In general, the surface temperature and the bulk temperatures of CFC and the CuCrZr cooling structure increase with the applied heat flux. The temperatures determined by the one-color pyrometer (spot size of $d = 6$ mm) and the two-color pyrometer (spot size of $d = 18$ mm) were measured on the same CFC tiles that are equipped with the thermocouples (CFC tile #3, see section 3.7.2). Values for $T_{one-color\,pyrometer}$ are much higher than the calculated surface temperatures. Local hot spots at the CFC surface, e.g. at the ends of carbon fibers, which considerably affect the temperature determination, might be responsible for these intense values. With increasing heat flux load these hot spots are negligible compared to the average emission level of the CFC surface. In this case, the values of $T_{one-color\,pyrometer}$ approach the calculated temperature curve. This effect can be observed in fig. 5.15. The temperatures of the two-color pyrometer, $T_{two-color\,pyrometer}$, agree with $T_{one-color\,pyrometer}$ very infrequently. These irregularities are related to the morphological inhomogeneity of CFC surfaces that

generates variable emissivities at the wavelengths measured by the two-color pyrometer.

The temperatures measured by both thermocouples, T_{TC2} and T_{TC1}, followed the expected temperature predicted by FEA for different heat fluxes. However, values of TC1 (CFC bulk) are slightly above the simulation and demonstrate that the material properties of NB31, taken from [13], do not agree exactly with the batch used in this work. These variations from batch to batch have already been distinguished in [203]. Since the same NB31 batch was used for all TiC_x modified flat tile mock-ups, there should be no differences of experimentally determined T_{TC1} values. However, the temperature T_{TC1} in bulk CFC is a bit higher for the non-modified and $TiC_{0.2}$ modified sample (see figs. 5.15 (a) and (c)) compared to the $TiC_{0.9}$ and Ti modified mock-ups (see figs. 5.15 (b) and (d)). This is an indication that the CFC/Cu interfaces of the mock-ups 'uncoated' and '$TiC_{0.2}$' consist of a higher amount of small bonding defects, which favors heat retention and raises the temperatures within the CFC tiles. That can be manifested by local dewetting at a very short lengthscale leading to pores at the interface or by an increased amount of carbon fiber cracks next to the interface. These cracks could be the result of an inadequate penetration of the CFC pores by the Copper-ABA brazing alloy leading to a less-strengthened CFC/Cu interface area. Nevertheless, a good bonding behavior could be demonstrated at the CFC tiles of all CFC/Cu/CuCrZr flat tile mock-ups accentuated in fig. 5.15.

Fig. 5.16 illustrates the infrared camera images at heat flux pulses of 6, 10.5, 12 and 15 MW/m^2, respectively, representing the surface temperature distribution for non-, $TiC_{0.9}$, $TiC_{0.2}$ and Ti modified CFC/Cu/CuCrZr flat tile mock-ups. These components show a quite similar behavior, the surface temperature increases with higher heat flux loadings and no incisive overheating that would lead to a detachment of a CFC tile can be observed. However, comparatively higher temperatures were found for tile #3 of the non-modified mock-up (see fig. 5.16 (a)) indicating some hot spots due to bonding failures. A small hot spot was also detected for the upper edge of tile #3 of the $TiC_{0.2}$ modified sample (see fig. 5.16 (c)). But this hot spot can also be a result of the thermocouple borehole. Nevertheless, these are indications that the wetting behavior of Copper-ABA on magnetron sputter deposited TiC_x films and on non-coated carbon substrates, shown in section 4.3.1, has an effect on the manufacturing of CFC/Cu/CuCrZr flat tile high heat flux components. The improved wettability of TiC_x films promotes the formation of a strengthened CFC/Cu bonding interface that can withstand high heat loads under thermal exposures.

Compared to magnetron sputter deposited $TiC_{0.9}$ films a deficient bonding performance of CVD-TiC coatings implemented in the CFC/Cu/CuCrZr flat tile mock-up can be observed in fig. 5.17. Tile #2 and #4 already show an overheating at 2 MW/m^2, identifying hot spots at the upper edges with temperatures of up to 1600°C. Therefore, the screening was stopped after a power density of 4 MW/m^2 and thermal cycling tests were abandoned, to avoid complete detachment of these tiles. This shows that the CVD-TiC coatings received for producing this mock-up could not provide adhesive CFC/Cu bonding free from defects.

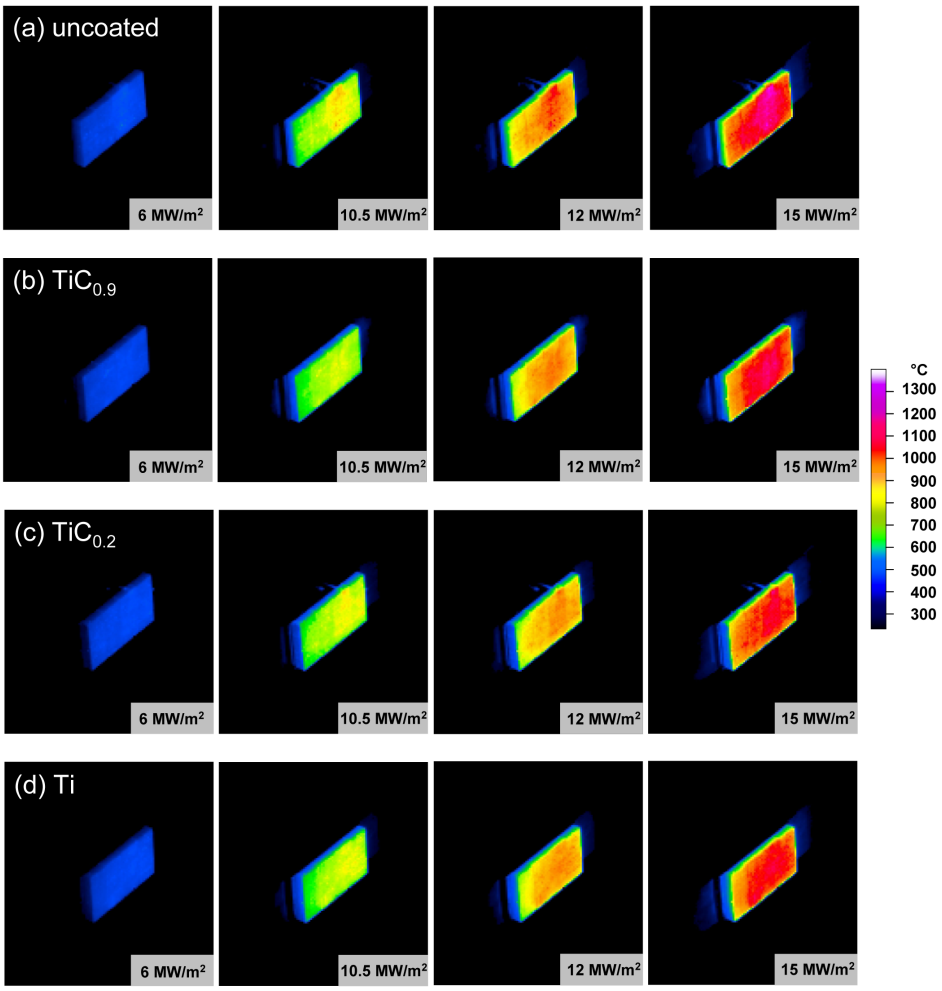

Figure 5.16: Infrared camera images during heat flux pulses at different power densities, representing the surface temperature distribution, for (a) non-, (b) $TiC_{0.9}$, (c) $TiC_{0.2}$ and (d) Ti modified CFC/Cu/CuCrZr flat tile mock-ups

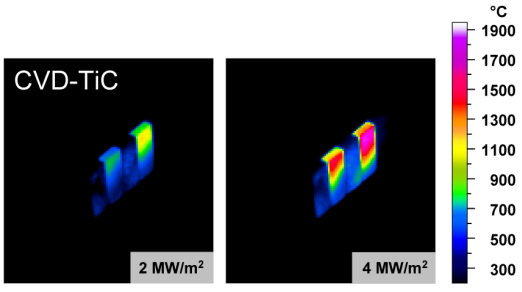

Figure 5.17: Infrared camera images during heat flux pulses at different power densities, representing the surface temperature distribution, for the CVD-TiC modified CFC/Cu/CuCrZr flat tile mock-up; screening was abandoned at 4 MW/m^2, because hot spots on two CFC tiles were identified indicating very high temperature loadings at the edges of the tiles

5.3.3 Microscopic post-examination

A cross-section analysis of each high heat flux tested mock-up was performed to check the bonding quality of the CFC/Cu interface. During cycling tests the temperatures at the thermocouples were homogeneous and did not change significantly with increasing number of cycles. Images of the components 'uncoated', '$TiC_{0.9}$', '$TiC_{0.2}$' and 'Ti' are shown in fig. 5.18. These viewgraphs were made at a cross-section of the CFC/Cu interface of each tile #3. They are representative for the whole cross-section, respectively. After 100 cycles at 15 MW/m^2 no detachment of the CFC tiles and no symptoms of CuCrZr cooling structure fatigue were observed. A good bonding behavior is established at the non-modified braze joint and at compounds brazed by magnetron sputter deposited TiC_x films.

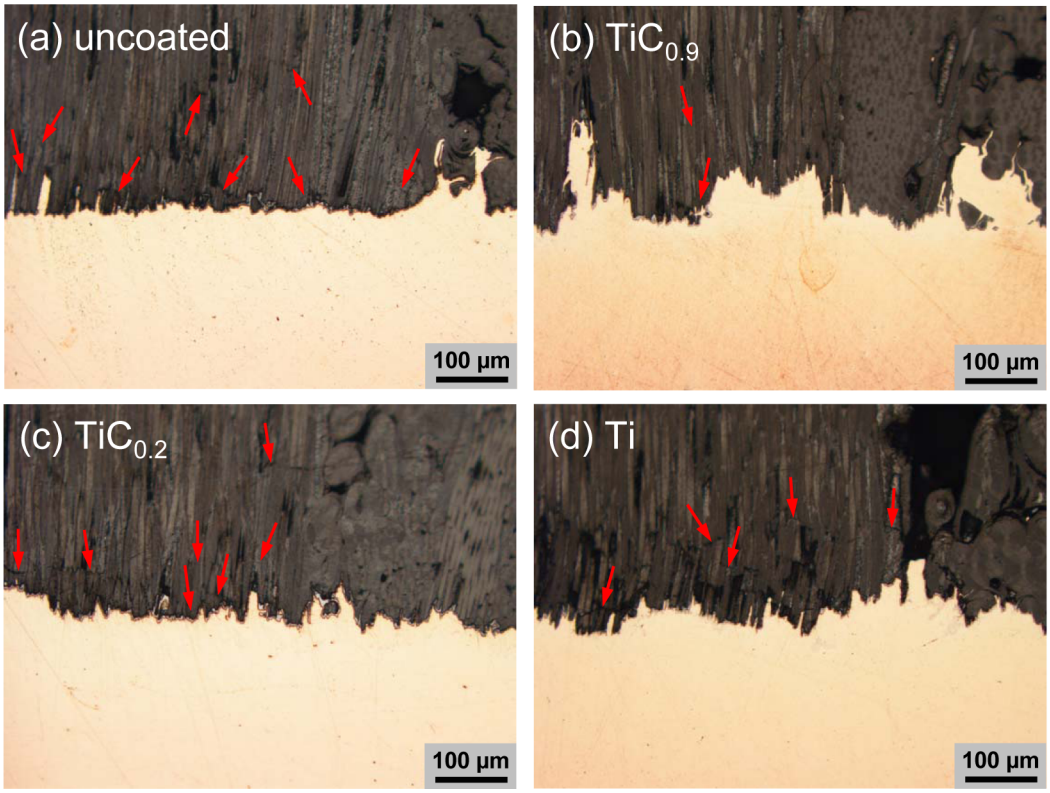

Figure 5.18: Cross-sections of the tile #3 CFC/Cu interface after 100 cycles at 15 MW/m^2, for (a) non-, (b) $TiC_{0.9}$, (c) $TiC_{0.2}$ and (d) Ti modified CFC/Cu/CuCrZr flat tile mock-ups; red arrows emphasize interface-near micro-cracks in the CFC

In a detailed inspection, differences could be detected in fig. 5.18. The compounds exhibit several micro-cracks of ex-pitch fibers visible in NB31 next to the CFC/Cu interface (red arrows). Table 5.1 lists the observed frequency of micro-cracks counted at the entire cross-sections, respectively. CFC micro-cracks have been counted from the CFC/Cu interface within the distance of 500 µm. The $TiC_{0.9}$ modified sample shows a perfect bonding quality with less micro-cracks even after 100 cycles at 15 MW/m^2. They appear more frequently at the non- and $TiC_{0.2}$ modified mock-up. The higher amount of micro-cracks indicate that the joint area of the 'uncoated' and '$TiC_{0.2}$' compound is less strengthened than the '$TiC_{0.9}$' and 'Ti' samples. The results of the wettability experiments shown in section 4.3 are in a good

agreement to these observations.

Table 5.1: Observed frequency of CFC micro-cracks next to the CFC/Cu interface counted at the cross-sections of tile #3 of the $TiC_{0.9}$, $TiC_{0.2}$, Ti and non-modified CFC/Cu/CuCrZr flat tile mock-up

	uncoated	$TiC_{0.9}$	$TiC_{0.2}$	Ti
observed frequency in (crack/mm)	10.1	4.8	8.8	6.5

Cross-sections of the CVD-TiC modified CFC/Cu/CuCrZr flat tile mock-up are presented in fig. 5.19. These microscope images show the CFC/Cu interface area at the upper edge of tile #2 after screening at 4 MW/m^2 (here, hot spots were detected, see fig. 5.17). A gap between CFC and the titanium carbide reaction layer could be observed (red arrows). Obviously, the CVD-TiC layer is responsible for the detachment at the CFC/Cu braze joint and for the overheating of the CFC tile during the HHF tests.

The CVD-TiC films received from the British company Archer Technicoat appear full of cracks and pores (see section 4.1). The amount of these manufacturing defects have been significantly higher with respect to magnetron sputter deposited TiC_x films. Cracks through the film probably inhibit the wetting behavior of the Copper-ABA brazing alloy on these films (see section 4.3). In addition, cracks along the CVD-TiC film/substrate interface, as observed in fig. 4.12, might lead to a reduced contact area. Therefore, debonding at the CFC/Cu interface during high heat flux tests could take place due to stress overloads at the reduced contact area. Obviously, the implementation of wetting promoting TiC_x films in CFC/Cu/CuCrZr flat tile mock-ups requires adhesive and crack-free coatings. They can be produced by optimizing the deposition process (as shown for magnetron sputter deposited TiC_x films in section 4.2).

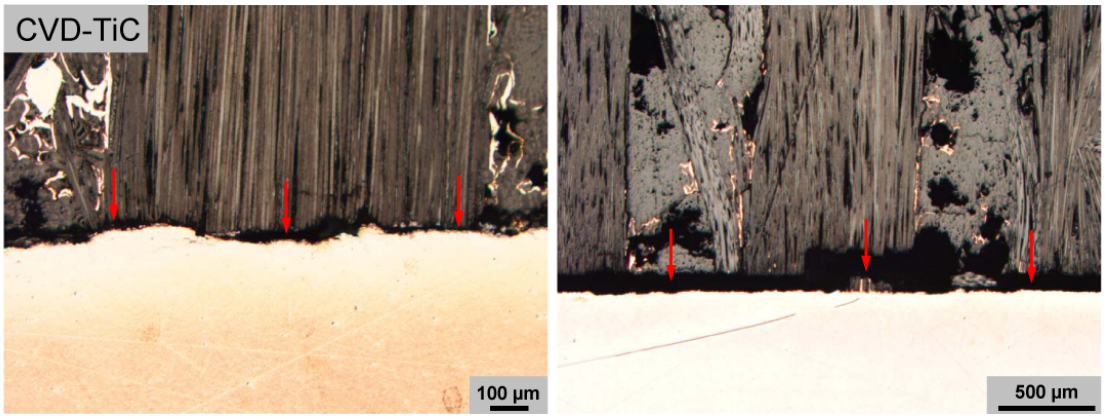

Figure 5.19: Cross-sections of the tile #2 CFC/Cu interface after screening tests of the CVD-TiC modified CFC/Cu/CuCrZr flat tile mock-up stopped at 4 MW/m^2; red arrows emphasize a gap (detachment) along the interface of CFC and the titanium carbide reaction layer

5.3.4 Summary of high heat flux tests

Actively cooled TiC_x modified CFC/Cu/CuCrZr flat tile mock-ups were brazed successfully and tested in the high heat facility GLADIS. The feasibility of implementing wetting promoting TiC_x films was demonstrated for magnetron sputter deposited coatings, $TiC_{0.9}$, $TiC_{0.2}$ and Ti. These elements, as well as the non-modified reference mock-up, did not exhibit serious bonding defects at heat fluxes of up to 15 MW/m^2 and withstood 100 cycles at 15 MW/m^2 without detachment of the CFC tiles. Actually, the oxygen plasma treatment of the CFC bonding surfaces significantly contributes to these results. Temperatures measured within these flat tile mock-ups confirm the thermal behavior predicted by the FEA. Mentionable bonding defects were observed only at the $TiC_{0.2}$ and the non-modified mock-up.

Microscopic investigations of cross-sections after the cycling tests gave more information about the thermal performance of these elements. Micro-cracks within the CFC were detected at the CFC/Cu interfaces. The highest frequency of these cracks was observed at the non-modified mock-up. On the other hand, the compound prepared by a $TiC_{0.9}$ film exhibited the best bonding performance even after 100 cycles at 15 MW/m^2. Thus, the wetting promoting behavior of TiC_x films, which already exist in the face-centered cubic TiC crystal phase ($x = 0.6 - 1$, see section 4.3), has an impact on long cycle fatigue tests of TiC_x modified CFC/Cu/CuCrZr flat tile components and results in good bonding characteristics.

CVD-TiC film assisted brazing of CFC/Cu/CuCrZr flat tile mock-ups generated areas of low-adhesion at the CFC/Cu interface resulting in debonding and overheating of CFC tiles. The test was stopped after a heat flux density of 4 MW/m^2 and thermal cycling tests were abandoned to avoid complete detachment of these tiles. Implementing CVD-TiC films requires a deposition process providing a defect-free and low-stress film consistency, as it was achieved by magnetron sputter deposited TiC_x coatings.

The high heat flux tests have shown that magnetron sputter deposited TiC_x coatings in the range of $x = 0.6 - 1$ improve the long-term performance of brazed CFC/Cu/CuCrZr flat tile components under high heat flux loadings and are possible candidates to be implemented in actively cooled divertor applications like for ITER or WENDELSTEIN 7-X.

6 Assessment of the component performance

6.1 Aspects of the CFC/Cu joint

Different TiC_x films were coated on CFC to enhance the wetting and penetration properties during the brazing procedure of CFC/Cu flat tile divertor components. In this work, magnetron sputter deposited $TiC_{0.9}$, $TiC_{0.2}$ and Ti films and a CVD-TiC coating were analysed with respect to their structural and wettability behavior and tested in brazed CFC/Cu components. In the following, several aspects of these TiC_x modified CFC/Cu braze joints are discussed in detail.

6.1.1 Wetting velocity

An enhanced wetting velocity turned out to be the main improvement of thin TiC_x films concerning the wetting behavior of Copper-ABA on carbon substrates and was extensively discussed in section 4.3.2. The idea was to implement thin wetting improving TiC_x films in the Copper-ABA brazing procedure of CFC/Cu flat tile divertor components, which was developed by the Italian company, Ansaldo Ricerche (see section 1.3), in order to obtain a good anchorage to the porous CFC and hence a better component adhesion under thermal and mechanical exposures. It is essential that these compounds sustain high heat loads, which occur in nuclear fusion divertor applications. Therefore, wettability studies of liquid Copper-ABA were performed on TiC_x films coated on flat carbon substrates, as described by the sessile drop method in section 3.4.

As we know from section 2.5, there are two important parameters to characterize the wettability behavior of a liquid on a solid: the degree of wetting and the rate of wetting. They are governed by the laws of thermodynamics and kinetics and indicated by the equilibrium or final contact angle and the wetting velocity, respectively. In the case of wetting by Copper-ABA, the final contact angle is of low relevance for characterizing the wetting improving behavior of TiC_x films on carbon substrates. Due to the high titanium activity in the Copper-ABA alloy, the same high-wettable reaction product was formed for every TiC_x film and the uncoated reference sample (reactive wetting). In section 4.3.1, this reaction product was identified as $TiC_{0.6}$ with face-centered cubic crystal structure.

The experiments in section 4.3 have shown that a comparison of different Copper-ABA/TiC_x systems is only reasonable by characterizing the wetting velocity. In all systems the wetting velocity was constant (reaction-limited reactive wetting). In this case, a stationary configuration with a constant chemical environment is established at the reaction front during wetting. Fig. 4.25 of section 4.3.2.1 illustrates one of the most important results of this work: the significantly highest wetting velocity within different Copper-ABA/TiC_x systems was achieved for magnetron sputter deposited $TiC_{0.9}$ films. Rapid wetting occurred only on TiC_x films with this specific stoichiometry, while the $TiC_{0.2}$ and Ti films and the uncoated reference sample

exhibited wetting velocities of one order of magnitude lower.

The XRD measurements of section 4.1.2 have shown for magnetron sputter deposited TiC_x films that two different crystal phases exist in the stoichiometry range $0 \leq x \leq 1$: the α-Ti phase (hcp structure) for $x = 0$ and the TiC phase (fcc structure) for $x = 0.6 - 1$. In the range of $0 < x < 0.6$, hcp and fcc structures were found as well, but in a distorted or metastable constitution. The atomic order or disorder of these crystal structures was reviewed in section 2.1. The $TiC_{0.9}$ films represent the whole fcc TiC phase, the Ti films the hcp Ti phase and the $TiC_{0.2}$ films the intermediate phase. The wetting velocity obviously depends on the crystal structure of the TiC_x coatings. Films, which already exist in the face-centered cubic TiC crystal phase ($x = 0.6 - 1$), lead to a higher wetting velocity and thus, to an improved wetting behavior of the Copper-ABA/TiC_x systems.

In section 4.2, it was figured out that the stress state of the TiC_x films has a great influence on the wetting velocity. It is essential to use low-stress coatings for the wettability experiments, because otherwise, the wetting reaction is slowed down by failures of the film constitution generated by high film stresses. These failures appear in form of buckling, cracks and delamination. A systematic stress optimization of magnetron sputter deposited TiC_x films was performed and low-stress coatings without such failures could be achieved by varying the deposition parameters. Using these optimized films, reasonable wettability results were produced that allow the comparison of the wetting velocity among each other. Non-optimized CVD-TiC coatings were tested as well (see section 4.3) and serve as an example for a wettability behavior that cannot be compared with other TiC_x films. Cracks and delamination were responsible for low and even different wetting velocities (see fig. 4.25 of section 4.3.2.1) during one wetting process of Copper-ABA on CVD-TiC films. In fact, it was expected to achieve the same high wetting velocity as magnetron sputter deposited $TiC_{0.9}$ film, because CVD-TiC coatings exist in the same face-centered cubic TiC crystal phase. The low wetting velocity of these non-optimized CVD-TiC films also affected the performance tests of chapter 5. In all experiments using TiC_x modified CFC/Cu braze joints, the CVD-TiC sample failed (see section 5.3) or achieved too low strength values (see section 5.2). Therefore, it could be shown in this work that it is important to use stress-optimized (low-stress) coatings for any wettability experiments with thin films and for their implementation in braze joined components.

After implementation of TiC_x films in CFC/Cu braze joints (brazed by Copper-ABA), no differences could be detected within the results of the shear strength tests (see section 5.2). The shear strength of $TiC_{0.9}$ modified CFC/Cu compounds was on the same level as other TiC_x samples (Ti, $TiC_{0.2}$ and the uncoated reference sample). Thus, the high wetting velocity of Copper-ABA on $TiC_{0.9}$ films, which was determined under the wetting test configuration of section 4.3 (film on smooth carbon substrates), does not automatically lead to an improved anchorage of copper to the porous CFC or to an improved shear strength of the CFC/Cu interface. Thin TiC_x coatings deposited on CFC surfaces (see fig. 4.13 of section 4.1.3) have no impact on mechanical properties of subsequently brazed CFC/Cu components. In principle, the high heat flux tests of TiC_x modified CFC/Cu/CuCrZr flat tile mock-ups came to the same conclusion: the $TiC_{0.9}$ sample made no exception and a similar thermal performance of all components was observed (see section 5.3). However, the lowest frequency of micro-cracks after 100 cycles at 15 MW/m^2 was detected at the $TiC_{0.9}$ modified component. Most likely, this is an indication that the high wetting velocity of $TiC_{0.9}$ films still has an impact on the performance and component adhesion of CFC/Cu braze joints under thermal exposures.

High wetting velocities during wetting experiments on TiC_x films were also observed with the Gemco alloy (see section 4.3). Unlike wetting with Copper-ABA, the Gemco/TiC_x sys-

tems strongly depend on the titanium activity in the melt. Thus, high wetting velocities were achieved for films with a high titanium concentration (Ti and $TiC_{0.2}$). Due to these good wetting characteristics and, in particular, due to the lower Gemco melting temperature ($T_{melt,Copper-ABA} = 1024°C$, $T_{melt,Gemco} = 975°C$), brazing by the Gemco alloy and using a Ti-rich TiC_x interlayer ($TiC_{x\to 0}$) can be proposed as an option for the CFC/Cu brazing technology using the Copper-ABA alloy.

6.1.2 Oxygen plasma treatment

The effect of the CFC surface roughening by the oxygen plasma treatment, as it can be seen in fig. 3.8 of section 3.6, was introduced during the shear strength evaluation (see section 5.2), because it was not clear, whether the values without oxygen plasma treatment represent the real interfacial shear strength of the TiC_x modified CFC/Cu interfaces or the interlaminar shear strength of the CFC fibers, which failed close to the interface. The aim of the oxygen plasma treatment was to solve this problem by increasing the size of the strengthened bonding area, which actually correspond to the penetration depth of the brazing alloy Copper-ABA into the CFC pores. Section 5.2.2 has shown that the shear strength values determined with oxygen plasma treated CFC exceed the corresponding values of the tests performed without oxygen plasma treatment by a factor of 2 and more. In addition, they exceed the interlaminar shear strength of the CFC by the same factor. By this result, it can be concluded that in any experiment, with or without oxygen plasma treatment, the real shear strength values of the TiC_x modified CFC/Cu interfaces were measured.

By this means, another important observation of this work was made: the oxygen plasma treatment leads to a better anchorage of the brazing alloy Copper-ABA in the CFC and promotes the CFC/Cu bonding strength and adhesion. The principle behind the CFC surface roughening is similar to Plansee's AMC technique (see section 1.3), but works with the oxygen plasma treatment instead of a laser structuring of the CFC surface. A detailed comparison between both techniques can be found in section 6.2.

The oxygen plasma treatment was also applied to the high heat flux tests of TiC_x modified CFC/Cu/CuCrZr flat tile mock-ups (see section 5.3). As the results of these tests show, all components (except for CVD-TiC) exhibited a good thermal performance under high heat flux loadings. The oxygen plasma treatment of the CFC brazing surfaces significantly contributes to these results. Even the non-modified sample withstood 100 cycles at 15 MW/m^2 without mentionable bonding defects. Therefore, the roughening of the CFC brazing surfaces by physical and chemical erosion, i.e. by oxygen plasma treatment, is an effective way to improve the bonding strength and adhesion of CFC/Cu divertor components.

6.2 Relevance for nuclear fusion research

In a nuclear fusion reactor the divertor components are exposed to the highest particle fluxes and heat loads. Therefore, it is important that the CFC/Cu bonding techniques of section 1.3 achieve a high bonding and adhesive strength under thermomechanical loadings. The aim of this work was to improve the Copper-ABA brazing procedure, as it was developed by the Italian company, Ansaldo Ricerche, by the introduction of a wetting enhancing thin TiC_x film.

The tests described in chapter 4 and 5 have shown that magnetron sputter deposited TiC_x coatings in the range of $x = 0.6 - 1$ exhibit a improved wetting behavior, but hardly improve the long-term performance of brazed CFC/Cu/CuCrZr flat tile components under high

heat flux loadings (see section 5.3). Nevertheless, these coatings are possible candidates to be implemented in actively cooled fusion divertor applications like for ITER or WENDELSTEIN 7-X.

The oxygen plasma treatment of the CFC surfaces before brazing could achieve much higher bonding strength values than the modification by wettability enhanced TiC_x films (see section 5.2). By this procedure, the bonding strength could be increased by a factor of 2 and more. In fact, these values reached the same order of magnitude that have been obtained by CFC/Cu joints produced by Plansee's AMC technique (see section 5.2.2). This technique is described in section 1.3 and is presently the most frequently used CFC/Cu joining technique for fusion divertor applications [12,22,29]. In the following, similarities and differences between both techniques will be discussed.

Both CFC/Cu joining methods, the AMC technique and the Copper-ABA brazing procedure with the oxygen plasma pre-treatment, have in common that they use a mechanical interlocking and that they increase the bonding surface. Therefore, a better anchorage of copper in the CFC can be achieved. However, this enlargement of the CFC bonding surface is realized by two different ways: the oxygen plasma treatment utilizes atomic processes (chemical and physical erosion), which leads to a CFC surface roughening in a micro-scale (µm-range), while the AMC technique uses a laser structuring of the CFC surface in a macro-scale (mm-range). The oxygen plasma treatment has a beneficial selective effect, because the the porous CFC matrix is removed from the brazing surface and the ex-pitch fibers are uncovered. By this way, a direct joining between copper and the ex-pitch fibers is possible. These fibers highly contribute to the good mechanical strength characteristics of CFC in the direction perpendicular to the joint. By contrast, the AMC laser structuring of the CFC bonding surfaces is performed randomly. Compared to the brazing technique that uses the oxygen plasma treatment, the AMC method is much more complex and expensive. In addition, the CFC/Cu/CuCrZr brazing procedure can be performed in a single-step, while it is a double-step in the AMC process.

It can be recommended to join copper to CFC by the Copper-ABA brazing technique including a pre-treatment of the CFC brazing surface (ex-pitch fibers perpendicular to the brazing surface) by oxygen plasma (see section 3.6) and by coating of a thin face-centered cubic TiC_x film in the range of $x = 0.6 - 1$. Then, adequate bonding strength values and a good thermomechanical performance of the CFC/Cu compound is guaranteed. In conclusion, the Copper-ABA brazing technique including the oxygen plasma pre-treatment can be used as an equivalent option (compared to the AMC method) in order to produce high-qualitative CFC/Cu joints for fusion divertor applications like ITER or WENDELSTEIN 7-X. However, further considerations for a large-scale production are still required.

Alternatively, the brazing technique using the titanium-free alloy Gemco can be adopted to produce CFC/Cu joints. However, there is one requirement that has to be fulfilled for brazing of CFC/Cu joints by the Gemco alloy: a titanium-rich TiC_x film ($TiC_{x\to 0}$) has to be implemented in order to ensure good wettability properties during brazing. By this way, the brazing temperature of the Copper-ABA procedure could be decreased about 50°C (see wettability experiments of section 4.3). It would increase the distance of the brazing temperature and the melting temperature of pure copper, which leads to safer brazing. In addition, the single-step brazing of a CFC/Cu/CuCrZr component could be performed using just one brazing alloy.

7 Conclusion

The divertor design of future fusion machines like ITER or WENDELSTEIN 7-X comprises joints between CFC and the copper alloy heat sink. These joints must operate under vacuum conditions and withstand cyclic thermal, mechanical and neutron loads. Furthermore, the joints must have an adequate lifetime and reliability in order to limit the overall cost of the component. The main problem of the CFC/Cu joint manufacturing is the large thermal expansion mismatch of the components and the very high contact angle of molten copper on carbon substrates.

The CFC/Cu brazing technology developed by the Italian company, Ansaldo Ricerche, foresees the use of a commercial Cu–Ti active brazing alloy (Copper-ABA®). However, an insufficient penetration of CFC pores turned out to be the main bonding drawback during this brazing procedure. Furthermore, the sudden change of physical and mechanical properties across the CFC/Cu joint and the presence of intermetallic compounds formed by the titanium atoms that do not react with the CFC surface are detrimental to thermal fatigue lifetime. Thus, the control of the wettability during the CFC/Cu joint manufacturing process is of high relevance.

The main focus of this work was to investigate the wettability behavior of thin titanium carbide films (TiC_x), produced by physical and chemical vapor deposition methods. The goal was to improve the brazing procedure of CFC/Cu high heat flux components by the introduction of a wetting enhancing thin TiC_x film in order to obtain a good anchorage to the porous CFC and hence a better component adhesion under thermal and mechanical exposures.

For this purpose, thin TiC_x films with stoichiometries from pure titanium to stoichiometric TiC ($0 \leq x \leq 1$) were produced by dual magnetron sputter deposition. This method offers a variety of deposition parameters in order to tailor the coatings properties and to adjust a specific stoichiometry. In addition, stoichiometric TiC coatings were produced by the CVD technique. Various analytical techniques were applied to achieve a comprehensive view about the structure, stress state and wetting behavior of these TiC_x films. Subsequently, TiC_x modified CFC/Cu braze joints were tested under thermomechanical loads in order to evaluate the impact of the TiC_x films on the CFC/Cu bonding strength.

The results are divided in two main sections, dealing with investigations on the **characterization of TiC_x films** and on the **implementation of TiC_x films in CFC/Cu braze joints**, and are summarized below.

Characterization of TiC_x films

The TiC_x film structure TiC_x coatings with different stoichiometries could be achieved by the dual magnetron sputter deposition technique by varying the discharge power densities of both, the titanium and the graphite cathodes. The stoichiometries of the TiC_x films were determined by RBS, their crystallinity by XRD investigations. Two different crystal phases were found in the stoichiometry range $0 \leq x \leq 1$: the α-Ti phase (hcp structure) for $x = 0$

and the TiC phase (fcc structure) for $x = 0.6 - 1$. In the range of $0 < x < 0.6$, hcp and fcc structures were found as well, but due to the shifting of X-ray diffraction peaks to positions that deviate from bulk α-Ti and bulk TiC and due to the low intensities of these reflexes, the crystallinity can be assumed to be distorted or metastable. Hcp and fcc structures were never found simultaneously within one diffractogram of a certain stoichiometry. At increasing x from $x = 0$ to $x = 1$, the change of the α-Ti (0 0 2) peak into the TiC (1 1 1) peak points at the transition of the c-axis of hcp titanium into the space diagonal of fcc TiC. The fcc TiC phase found for the range $x = 0.6 - 1$ is in accordance with the TiC homogeneity interval of the Ti-C phase diagram. A thermodynamically favored crystal structure was detected for $TiC_{0.9}$ films.

The CVD technique produced only stoichiometric TiC films with fcc crystal structure. However, this deposition procedure generated many defects in the film, like pores and cracks.

Influence of the deposition parameters on the stress state in TiC_x films Under certain deposition conditions, magnetron sputter deposited TiC_x films exhibited high compressive film stresses resulting in extensive buckling and delamination. Therefore, systematic investigations of the intrinsic film stress were performed using both, the curvature and the $\sin^2\psi$ method. The intrinsic stress of magnetron sputtered TiC_x films could be adjusted by varying the deposition parameters used for this work: power density (both cathodes), C/Ti power ratio and argon gas pressure. Basically, three effects could be observed:

1. Increasing argon gas pressure favors tensile stress (stronger effect at $TiC_{x\to 1}$)
2. Increasing the power level (thus, the deposition rate) leads to tensile stress
3. Increasing the C/Ti power ratio (thus, the factor of nonstoichiometry x) tends to compression

Investigations about intrinsic stress of magnetron sputtered TiC_x films showed that low-stress coatings can be achieved in the whole stoichiometry range from $x = 0$ to $x = 1$. Any structural malfunction of the films could be avoided.

The wettability behavior on TiC_x films High temperature wetting experiments were performed by the sessile drop method to examine the wettability characteristics of TiC_x films wetted by the brazing alloy Copper-ABA. For this concern, a contact angle measurement device including an inductive heating system was constructed and successfully tested. Magnetron sputter deposited $TiC_{0.9}$ (fcc titanium carbide), $TiC_{0.2}$ (metastable) and Ti (hcp α-titanium) coatings were chosen to represent each crystallinity zone in the range of $0 \leq x \leq 1$. CVD-TiC films and uncoated graphite substrates (reference samples) were tested as well.

The tests have shown that initial contact angles lower than 90° were obtained for all magnetron sputtered TiC_x films, but not for the CVD-TiC and the reference sample. Due to the high titanium activity in the Copper-ABA alloy, every sample was wetted at the same low final contact angle ($\theta_F = 6°$). These processes can be attributed to reactive wetting. The significantly highest spreading velocities of Copper-ABA droplets were achieved for magnetron sputter deposited $TiC_{0.9}$ films. Thus, the wetting behavior of Copper-ABA on carbon materials can be improved by coating of TiC_x films, which already exist in the face-centered cubic TiC crystal phase ($x = 0.6 - 1$).

The wetting behavior of the CVD-TiC films was inhibited by stress-induced deposition defects (cracks). Poor wetting of Copper-ABA was observed (high initial contact angles, low spreading velocities). The comparison of low-stress magnetron sputter deposited TiC_x films with CVD-TiC coatings shows the importance of stress optimization for a good wetting performance.

In addition, wetting experiments of the titanium-free brazing alloy Gemco were performed on TiC_x films. Unlike wetting with Copper-ABA, these systems strongly depend on the titanium activity in the melt. Thus, high spreading velocities and low initial contact angles of Gemco droplets were observed for films with a high titanium concentration (Ti and $TiC_{0.2}$). Due to these good wetting characteristics and, in particular, due to the lower Gemco melting temperature ($T_{melt,Copper-ABA} = 1024°C$, $T_{melt,Gemco} = 975°C$), brazing by the Gemco alloy and using a Ti-rich TiC_x interlayer ($TiC_{x\to 0}$) can be proposed as an option for the CFC/Cu brazing technology using the Copper-ABA alloy.

Implementation of TiC_x films in CFC/Cu braze joints

Shear strength properties of TiC_x modified CFC/Cu braze joints TiC_x modified copper to CFC NB31 components, which have been brazed by the Copper-ABA alloy, were subjected to shear strength experiments. These tests have shown, that the modification by thin TiC_x films do not increase the CFC/Cu bonding strength. An increase of the shear strength by a factor of 2 and more was only achieved by a modification of the initial CFC surface. The treatment with biased oxygen plasma provided the opening of CFC pores by physical and chemical erosion. This had a beneficial impact on the anchoring effect of the liquid brazing alloy in the CFC. By this way, a bonding strength was achieved comparable to experiments performed with other CFC/Cu bonding technologies. For braze joints modified by CVD-TiC coatings a non-adhesive behavior after brazing was detected and hence, low shear strength values were measured.

Performance of TiC_x modified high heat flux components under cyclic thermomechanical loads Actively cooled TiC_x modified CFC/Cu/CuCrZr flat tile mock-ups were brazed successfully and tested in the high heat facility GLADIS. The feasibility of implementing wetting promoting TiC_x films was demonstrated for magnetron sputter deposited coatings, $TiC_{0.9}$, $TiC_{0.2}$ and Ti. These elements, as well as the non-modified reference mock-up, did not exhibit serious bonding defects at heat fluxes of up to 15 MW/m^2 and withstood 100 cycles at 15 MW/m^2 without detachment of the CFC tiles. Actually, the oxygen plasma treatment of the CFC bonding surfaces before the coating and the brazing procedure significantly contributes to these results. Temperatures measured within these flat tile mock-ups confirm the thermal behavior predicted by the finite element analysis. Mentionable bonding defects were observed only at the $TiC_{0.2}$ and the non-modified mock-up.

Microscopic investigations of cross-sections after the cycling tests gave more information about the thermal performance of these elements. Micro-cracks within the CFC were detected at the CFC/Cu interfaces. The highest frequency of these cracks was observed at the non-modified mock-up. On the other hand, the compound prepared by a $TiC_{0.9}$ film exhibited the best bonding performance even after 100 cycles at 15 MW/m^2. Thus, the wetting promoting behavior of TiC_x films, which already exist in the face-centered cubic TiC crystal phase ($x = 0.6 - 1$), has an impact on long cycle fatigue tests of TiC_x modified CFC/Cu/CuCrZr

flat tile components and results in good bonding characteristics.

CVD-TiC film assisted brazing of CFC/Cu/CuCrZr flat tile mock-ups generated areas of low-adhesion at the CFC/Cu interface resulting in debonding and overheating of CFC tiles. The test was stopped after a heat flux density of 4 MW/m^2 and thermal cycling tests were abandoned to avoid complete detachment of these tiles. Implementing CVD-TiC films requires a deposition process providing a defect-free and low-stress film consistency, as it was achieved by magnetron sputter deposited TiC_x coatings.

The high heat flux tests have shown that magnetron sputter deposited TiC_x coatings in the range of $x = 0.6 - 1$ improve the long-term performance of brazed CFC/Cu/CuCrZr flat tile components under high heat flux loadings and are possible candidates to be implemented in actively cooled divertor applications like for ITER or WENDELSTEIN 7-X.

8 List of publications and conference contributions

Publications

1. P. Worbs, M. Grattarola, H. Maier and H. Bolt. Wetting and fracture characteristics of TiC_x coated C/Cu braze joints. *Advanced Materials Research*, 59:230-236, 2009.

2. B. Schwarz, P. Worbs, C. Eisenmenger-Sittner. Applications of a high temperature sessile drop device. *Journal of Physics: Conference Series*, 100:082044, 2008.

Oral conference presentations

1. P. Worbs, M. Grattarola, H. Maier and H. Bolt. Wetting and fracture characteristics of TiC_x coated C/Cu braze joints. 1st International Conference on New Materials for Extreme Environments, June 2nd – 4th 2008, San Sebastian, Spain.

Poster presentations

1. P. Worbs, B. Schwarz, H. Maier and H. Bolt. TiC coatings as wetting promoter for optimizing carbon/copper brazed joints in high heat flux components. Euromat 2007, September 10th – 13th 2007, Nürnberg, Germany.

2. P. Worbs, F. Koch, K. Chaoui, S. Lindig and H. Bolt. Measurement and control of internal stress of magnetron sputtered tungsten coatings. 11th International Conference on Plasma Surface Engineering (PSE 2008), September 15th – 19th 2008, Garmisch-Partenkirchen, Germany.

Bibliography

[1] International Energy Agency (IEA). World Energy Outlook 2008.

[2] Bundesanstalt für Geowissenschaften und Rohstoffe. *http://www.bgr.bund.de.*

[3] Intergovernmental Panel on Climate Change (IPCC). Climate Change 2007 - Mitigation of Climate Change: Working Group III Contribution to the Fourth Assessment Report of the IPCC. Cambridge University Press, 2007.

[4] U. Schumacher. Status and problems of fusion reactor development. *Naturwissenschaften*, 88(3):102–112, 2001.

[5] G. Federici, A. Loarte, and G. Strohmayer. Assessment of erosion of the ITER divertor targets during type I ELMs. *Plasma Physics And Controlled Fusion*, 45(9):1523–1547, 2003.

[6] J. Boscary. Talk: Introduction to W7-X target elements – design review, March 2006.

[7] J. Wesson. *Tokamaks.* Oxford University Press, 3rd edition, 2004.

[8] M. Merola, G. Vieider, M. Bet, I. B. Vastra, L. Briottet, P. Chappuis, K. Cheyne, G. Dell'Orco, D. Duglue, R. Duwe, S. Erskine, F. Escourbiac, M. Febvre, M. Grattarola, F. Moreschi, A. Orsini, R. Pamato, L. Petrizzi, L. Plochl, B. Riccardi, E. Rigal, M. Rödig, J. F. Salavy, B. Schedler, J. Schlosser, S. Tahtinen, R. Vesprini, E. Visca, and C. H. Wu. European achievements for ITER high heat flux components. *Fusion Engineering And Design*, 56-57:173–178, 2001.

[9] P. Majerus, J. Compan, D. Pitzer, and M. Rödig. Measurement physical and mechanical properties of CFC delivered by SNECMA: Final Report, EFDA Task TW2-TVM-CFCQ2. Technical report, Forschungszentrum Jülich, IWV-2, August 2004.

[10] H. Renner, J. Boscary, V. Erckmann, H. Greuner, H. Grote, J. Sapper, E. Speth, F. Wesner, and M. Wanner. The capabilities of steady state operation at the stellarator W7-X with emphasis on divertor design. *Nuclear Fusion*, 40(6):1083–1093, 2000.

[11] B. Streibl, J. Boscary, H. Greuner, P. Grigull, J. Kisslinger, C. Li, B. Mendelevitch, T. Pirsch, N. Rust, S. Schweizer, A. Vorkoper, and M. Weissgerber. Manufacturing of the Wendelstein 7-X divertor and wall protection. *Fusion Engineering And Design*, 75-79:463–468, 2005.

[12] M. Merola, W. Danner, and M. Pick. EU R&D on divertor components. *Fusion Engineering And Design*, 75-79:325–331, 2005.

[13] Carbon Fibre Composites, Materials Assessment Report, ITER EDA Doc. Series, 2004, Chapter 2.3.

[14] Selection of Copper Alloys, Materials Assessment Report, ITER EDA Doc. Series, 2004, Chapter 1.4.

[15] J. F. Salavy, L. Giancarli, M. Merola, F. Picard, and M. Rödig. Analysis of high heat flux testing of mock-ups. *Fusion Engineering And Design*, 66-68:277–281, 2003.

[16] N. Eustathopoulos, M. G. Nicholas, and B. Drevet. *Wettability at High Temperatures.* Pergamon, 1999.

[17] D. A. Mortimer and M. Nicholas. Wetting of carbon by copper and copper alloys. *Journal Of Materials Science*, 5(2):149–155, 1970.

[18] D. A. Mortimer and M. Nicholas. Wetting of carbon and carbides by copper-alloys. *Journal Of Materials Science*, 8(5):640–648, 1973.

[19] F. Delannay, L. Froyen, and A. Deruyttere. The wetting of solids by molten metals and its relation to the preparation of metal-matrix composites. *Journal Of Materials Science*, 22(1):1–16, 1987.

[20] P. B. Abel, A. L. Korenyiboth, F. S. Honecy, and S. V. Pepper. Study of copper on graphite with titanium or chromium bond layer. *Journal Of Materials Research*, 9(3):617–624, 1994.

[21] F. Rainer and N. Reheis. Process for the manufacturing of a cooling unit. Patent EP 0 663 670. Plansee AG, Austria, 1995.

[22] B. Schedler, T. Huber, T. Friedrich, E. Eidenberger, M. Kapp, C. Scheu, R. Pippan, and H. Clemens. Characteristics of an optimized active metal cast joint between copper and C/C. *Physica Scripta*, T128:200–203, 2007.

[23] M. Ferraris, V. Casalegno, and M. Salvo. Process to join carbon based materials to metals and its applications. Patent WO2005/037734. Politecnico di Torino, Italy, 2005.

[24] S. Libera and E. Visca. Junction process for a ceramic material and a metallic material with the interposition of a transition material. Patent WO2006/024971. ENEA, Italy, 2006.

[25] M. Grattarola, M. Bisio, V. Branca, M. Di Marco, A. Federici, G. Gualco, P. Guarnone, U. Luconi, M. Merola, C. Ozzano, G. Pasquale, P. Poggi, S. Rizzo, and F. Varone. Manufacturing and testing in reactor relevant conditions of brazed plasma facing components of the ITER divertor. *Fusion Engineering and Design*, 75-79:277–83, 2005.

[26] M. Merola, A. Orsini, E. Visca, S. Libera, L. F. Moreschi, S. Storai, B. Panella, E. Campagnoli, G. Ruscica, and C. Bosco. Influence of the manufacturing heat cycles on the CuCrZr properties. *Journal Of Nuclear Materials*, 307:677–680, 2002.

[27] M. Salvo, V. Casalegno, S. Rizzo, F. Smeacetto, M. Ferraris, and M. Merola. One-step brazing process to join CFC composites to copper and copper alloy. *Journal Of Nuclear Materials*, 374(1-2):69–74, 2008.

[28] J. Linke. Plasma facing materials and components for future fusion devices - development, characterization and performance under fusion specific loading conditions. *Physica Scripta*, T123:45–53, 2006.

[29] H. Greuner, B. Böswirth, J. Boscary, A. Plankensteiner, and B. Schedler. High heat flux tests of the WENDELSTEIN 7-X pre-series target elements – Experimental evaluation of the thermo-mechanical behaviour. *Fusion Engineering And Design*, 82(15-24):1713–1719, 2007.

[30] N. Frage, N. Froumin, and M. P. Dariel. Wetting of TiC by non-reactive liquid metals. *Acta Materialia*, 50:237–245, 2002.

[31] H. O. Pierson. *Handbook of Refractory Carbides and Nitrides.* Noyes Publications, 1996.

[32] C. Gualco. *ExtreMat document: Table of Alternative Concepts for Work Package 4.2. No. EXM-SP4-TRE-ARI-0028. Rev. a.* Ansaldo Ricerche, 2nd November 2005.

[33] H. Maier and S. Levchuk. *ExtreMat document: Contribution of IPP to Deliverable 4.2.3: Concept Development Report (Phase 2). No. EXM-SP4-TRE-IPP-0005. Rev a.* Max-Planck-Institut für Plasmaphysik, 6th September 2005.

[34] C. C. Baker and S. I. Shah. Reactive sputter deposition of tungsten nitride thin films. *Journal Of Vacuum Science & Technology A-Vacuum Surfaces And Films*, 20(5):1699–1703, 2002.

[35] D. J. Kim, H. S. Sim, S. Lee, Y. T. Kim, S. Kim, and J. Park. Improvement of the reliability of a Cu/W-N/SiOF multilevel interconnect by inserting plasma enhanced chemical vapor deposited W-N thin film. *Japanese Journal of Applied Physics, Part 1 (Regular Papers, Short Notes & Review Papers)*, 40(3A):1214–1217, 2001.

[36] R. Hübler. Transition metal nitrides thin films deposition using a dynamically controlled magnetron sputtering apparatus. *Surface & Coatings Technology*, 158:680–684, 2002.

[37] B. Schwarz, P. Worbs, and C. Eisenmenger-Sittner. Applications of a high temperature sessile drop device. *Journal of Physics: Conference Series*, 100:082044, 2008.

[38] R. Freer. *The physics and chemistry of carbides, nitrides, and borides.* Kluwer Academic Publishers Dordrecht, 1990.

[39] M. Guemmaz, A. Mosser, L. Boudoukha, J. J. Grob, D. Raiser, and J. C. Sens. Ion beam synthesis of non-stoichiometric titanium carbide: Composition structure and nanoindentation studies. *Nuclear Instruments & Methods In Physics Research Section B-Beam Interactions With Materials And Atoms*, 111(3-4):263–270, 1996.

[40] A. I. Gusev and A. A. Rempel. Phase diagrams of metal-carbon and metal-nitrogen systems and ordering in strongly nonstoichiometric carbides and nitrides. *Physica Status Solidi A-Applied Research*, 163(2):273–304, 1997.

[41] A. I. Gusev and A. A. Rempel. *Atomic ordering and phase equilibria in strongly nonstoichiometric carbides and nitrides, in Materials Science of Carbides, Nitrides and Borides.* Kluwer Academic Publishers Dordrecht, 1999.

[42] A. I. Gusev, A. A. Rempel, and A. J. Magerl. *Disorder and Order in Strongly Nonstoichiometric Compounds: Transition Metal Carbides, Nitrides and Oxides.* Springer, 2001.

[43] G. Hägg. Gesetzmässigkeiten im Kristallbau bei Hydriden, Boriden, Karbiden und Nitriden der Übergangselemente. *Z. Phys. Chem.*, 12:33–56, 1931.

[44] J. L. Murray. *The C-Ti system, in Phase diagrams of Binary Titanium Alloys.* ASM Intern. Publ., Metals Park, Ohio, 1987.

[45] L. V. Zueva and A. I. Gusev. Effect of nonstoichiometry and ordering on the period of the basis structure of cubic titanium carbide. *Physics Of The Solid State*, 41(7):1032–1038, 1999.

[46] H. Goretzki. Neutron diffraction studies on titanium-carbon and zirconium-carbon alloys. *Physica Status Solidi*, 20(2):K141–K143, 1967.

[47] C. H. de Novion, B. Beuneu, T. Priem, N. Lorenzelli, and A. Finel. *Defect structures and order-disorder transformations in transition metal carbides and nitrides.* Kluwer Academic Publishers Dordrecht, Netherlands, 1990.

[48] V. N. Lipatnikov, L. V. Zueva, A. I. Gusev, and A. Kottar. Disorder-order phase transformations and electrical resistivity of nonstoichiometric titanium carbide. *Physics Of The Solid State*, 40(7):1211–1218, 1998.

[49] N. V. Dzhalabadze, B. G. Eristavi, N. I. Maysuradze, and E. R. Kuteliya. On structure of crystalline phases in thin Ti-C films. *Fizika Metallov I Metallovedenie*, 86(1):85–92, 1998.

[50] L. Ramqvist. Electronic structure of cubic refractory carbides. *Journal Of Applied Physics*, 42(5):2113–2120, 1971.

[51] V. A. Gubanov, V. P. Zhukov, and A. L. Ivanovsky. New achievements in theoretical calculations of electronic-structure and properties of transition-metal refractory compounds. *Quantum Mechanical Cluster Calculations In Solid State Studies*, pages 315–323, 1992.

[52] K. Schwarz. Band-structure and chemical bonding in transition-metal carbides and nitrides. *Crc Critical Reviews In Solid State And Materials Sciences*, 13(3):211–257, 1987.

[53] J. Redinger, R. Eibler, P. Herzig, A. Neckel, R. Podloucky, and E. Wimmer. Vacancy induced changes in the electronic-structure of titanium carbide. 1. band-structure and density of states. *Journal Of Physics And Chemistry Of Solids*, 46(3):383–398, 1985.

[54] J. Redinger, R. Eibler, P. Herzig, A. Neckel, R. Podloucky, and E. Wimmer. Vacancy induced changes in the electronic-structure of titanium carbide. 2. electron-densities and chemical bonding. *Journal Of Physics And Chemistry Of Solids*, 47(4):387–393, 1986.

[55] J. E. Mahan. *Physical Vapor Deposition of Thin Films.* Wiley, New York, 2000.

[56] M. Ohring. *The Materials Science of Thin Films.* Academic Press, San Diego, 1992.

[57] P. Sigmund. *Sputtering by ion bombardment: Theoretical concepts. In R. Behrisch (ed.), Sputtering by Particle Bombardment I: Physical Sputtering of Single-Element Solids*, volume 47 of Topics in Applied Physics. Springer, Berlin, 1981.

[58] F. Koch and H. Bolt. W-Si-Cr compounds as plasma-facing material for fusion reactors. In *European Congress on Advanced Materials and Processes (EUROMAT), Prag*, 2005.

[59] W. O. Hofer. *Angular, energy and mass distribution of sputtered particles. In R. Behrisch (ed.), Sputtering by Particle Bombardment III: Characteristics of Sputtered Particles, Technical Applications*, volume 64 of Topics in Applied Physics. Springer, Berlin, 1981.

[60] K. L. Choy. Chemical vapour deposition of coatings. *Progress In Materials Science*, 48(2):57–170, 2003.

[61] H. F. Döbele, H. Frey, W. Möller, and E. Taglauer. *Vakuum-Beschichtung 1: Plasmaphysik - Plasmadiagnostik - Analytik.* VDI, Düsseldorf, 1995.

[62] P. K. Bachmann, G. Gärtner, and H. Lydtin. *Plasma Assisted Chemical Vapor Deposition Processes.* MRS Bulletin, 1988.

[63] H. Bubert and H. Jennet, editors. *Surface and Thin Film Analysis. Principles, Instrumentation, Applications.* Wiley-VCH, Weinheim, 2002.

[64] J. C. Vickerman, editor. *Surface Analysis - The Principal Techniques.* John Wiley & Sons, 1997.

[65] W. K. Chu, J. W. Mayer, and M. A. Nicolet. *Backscattering Spectrometry.* Academic Press, New York, 1978.

[66] J. R. Tesmer and M. Nastasi, editors. *Handbook of modern Ion Beam Materials Analysis.* Materials Research Society, Pittsburgh, USA, 1995.

[67] M. Mayer. SIMNRA User's Guide, Tech. Rep. IPP 9/113. Max-Planck-Institut für Plasmaphysik, Garching bei München, 1997.

[68] B. D. Cullity and S. R. Stock. *Elements of X-ray Diffraction.* Addison-Wesley, 1967.

[69] M. Birkholz. *Thin Film Analysis by X-ray Scattering.* Wiley-VCH, Weinheim, 2006.

[70] G. I. Goldstein, D. E. Newbury, P. Echlin, D. C. Joy, C. Fiori, and E. Lifshin. *Scanning Electron Microscopy and X-ray Microanalysis.* Plenum Press, New York, 1981.

[71] G. C. A. M. Janssen. Stress and strain in polycrystalline thin films. *Thin Solid Films*, 515(17):6654–6664, 2007.

[72] A. Bagchi and A. G. Evans. The mechanics and physics of thin film decohesion and its measurement. *Interface Science*, 3(3):169–193, 1996.

[73] L. B. Freund and S. Suresh. *Thin Film Materials, stress, defect formation and surface evolution.* Cambridge University Press, 2003.

[74] M. W. Moon, H. M. Jensen, J. W. Hutchinson, K. H. Oh, and A. G. Evans. The characterization of telephone cord buckling of compressed thin films on substrates. *Journal Of The Mechanics And Physics Of Solids*, 50(11):2355–2377, 2002.

[75] M. F. Doerner and W. D. Nix. Stresses and deformation processes in thin-films on substrates. *Crc Critical Reviews In Solid State And Materials Sciences*, 14(3):225–268, 1988.

[76] H. Öttel and R. Wiedemann. Residual stresses in PVD hard coatings. *Surface & Coatings Technology*, 76(1-3):265–273, 1995.

[77] R. S. Wagner, A. K. Sinha, T. T. Sheng, H. J. Levinste, and F. B. Alexandre. Tungsten metallization for LSI applications. *Journal Of Vacuum Science & Technology*, 11(3):582–590, 1974.

[78] J. A. Thornton and D. W. Hoffman. Stress-related effects in thin-films. *Thin Solid Films*, 171(1):5–31, 1989.

[79] U. Welzel, J. Ligot, P. Lamparter, A. C. Vermeulen, and E. J. Mittemeijer. Stress analysis of polycrystalline thin films and surface regions by X-ray diffraction. *Journal Of Applied Crystallography*, 38:1–29, 2005.

[80] G. G. Stoney. The tension of metallic films deposited by electrolysis. *Proceedings Of The Royal Society Of London Series A – Containing Papers Of A Mathematical And Physical Character*, 82(553):172–175, 1909.

[81] P. A. Flinn, D. S. Gardner, and W. D. Nix. Measurement and interpretation of stress in aluminum-based metallization as a function of thermal history. *Ieee Transactions On Electron Devices*, 34(3):689–699, 1987.

[82] A. Mezin. Coating internal stress measurement through the curvature method: A geometry-based criterion delimiting the relevance of stoney's formula. *Surface & Coatings Technology*, 200(18-19):5259–5267, 2006.

[83] L. B. Freund, J. A. Floro, and E. Chason. Extensions of the stoney formula for substrate curvature to configurations with thin substrates or large deformations. *Applied Physics Letters*, 74(14):1987–1989, 1999.

[84] H. Windischmann and K. J. Gray. Stress measurement of CVD diamond films. *Diamond And Related Materials*, 4(5-6):837–842, 1995.

[85] I. C. Noyan and J. B. Cohen. *Residual Stress - Measurement by Diffraction and Interpretation*. Springer, New York, 1987.

[86] P. van Houtte and L. de Buyser. The influence of crystallographic texture on diffraction measurements of residual-stress. *Acta Metallurgica Et Materialia*, 41(2):323–336, 1993.

[87] M. Barral, J. M. Sprauel, and G. Mäder. *Eigenspannungen*. 2. Edition. DGM, Oberursel, 1983.

[88] M. Barral, J. L. Lebrun, J. M. Sprauel, and G. Mäder. X-ray macrostress determination on textured material - use of the ODF for calculating the X-ray compliances. *Metallurgical Transactions A-Physical Metallurgy And Materials Science*, 18(7):1229–1238, 1987.

[89] H. Blumenauer, editor. *Werkstoffprüfung*. Deutscher Verlag für Grundstoffindustrie, Stuttgart, 1994.

[90] V. I. Trefilov, O. N. Grigoriev, and S. M. Kushnerenko. Inhomogeneity of internal-stresses and X-ray elastic-constants of ceramic materials. *Materials Science And Engineering A-Structural Materials Properties Microstructure And Processing*, 168(1):99–102, 1993.

[91] H. U. Baron and V. Hauk. Evaluation of stresses on materials with fiber texture from lattice strain-measurements. *Zeitschrift Für Metallkunde*, 79(2):127–131, February 1988.

[92] A. Saerens, P. Van Houtte, B. Meert, and C. Quaeyhaegens. Assessment of different x-ray stress measuring techniques for thin titanium nitride coatings. *Journal Of Applied Crystallography*, 33:312–322, April 2000.

[93] V. Hauk and G. Vaessen. Residual-stresses in groups of crystallites of steels having preferred orientation. *Zeitschrift Fur Metallkunde*, 76(2):102–107, 1985.

[94] P. A. Flinn and C. Chiang. X-ray-diffraction determination of the effect of various passivations on stress in metal-films and patterned lines. *Journal Of Applied Physics*, 67(6):2927–2931, 1990.

[95] C. Quaeyhaegens, G. Knuyt, and L. M. Stals. Residual macroscopic stress in highly preferentially oriented titanium nitride coatings deposited on various steel types. *Journal Of Vacuum Science & Technology A-Vacuum Surfaces And Films*, 14(4):2462–2469, 1996.

[96] P. Gergaud, S. Labat, and O. Thomas. Limits of validity of the crystallite group method in stress determination of thin film structures. *Thin Solid Films*, 319(1-2):9–15, 1998.

[97] B. Lavi and A. Marmur. The exponential power law: partial wetting kinetics and dynamic contact angles. *Colloids And Surfaces A-Physicochemical And Engineering Aspects*, 250(1-3):409–414, 2004.

[98] R. Bhola and S. Chandra. Parameters controlling solidification of molten wax droplets falling on a solid surface. *Journal Of Materials Science*, 34(19):4883–4894, 1999.

[99] B. He, J. Lee, and N. A. Patankar. Contact angle hysteresis on rough hydrophobic surfaces. *Colloids And Surfaces A-Physicochemical And Engineering Aspects*, 248(1-3):101–104, 2004.

[100] J. Kijlstra, K. Reihs, and A. Klamt. Roughness and topology of ultra-hydrophobic surfaces. *Colloids And Surfaces A-Physicochemical And Engineering Aspects*, 206(1-3):521–529, 2002.

[101] P. T. Vianco and D. R. Frear. Issues in the replacement of lead-bearing solders. *Jom-Journal Of The Minerals Metals & Materials Society*, 45(7):14–19, 1993.

[102] D. R. Frear, W. B. Jones, and K. R. Kinsman. *Solder Mechanics: a State of the Art Assessment*. TMS, Warrendale, PA, 1991.

[103] M. M. Schwartz and Aircraft S. *Metals hand book*, volume 6. ASM, 10th edition, 1991.

[104] G. Kumar and K. N. Prabhu. Review of non-reactive and reactive wetting of liquids on surfaces. *Advances In Colloid And Interface Science*, 133(2):61–89, 2007.

[105] N. Eustathopoulos. Dynamics of wetting in reactive metal ceramic systems. *Acta Materialia*, 46(7):2319–2327, 1998.

[106] J. T. Davis and E. K. Rideal. *Interfacial phenomena.* Academic Press, New York, 2nd edition, 1966.

[107] P. Shen, H. Fujii, T. Matsumoto, and K. Nogi. Reactive wetting of SiO_2 substrates by molten Al. *Metallurgical And Materials Transactions A-Physical Metallurgy And Materials Science*, 35A(2):583–588, 2004.

[108] A. Contreras, C. A. Leon, R. A. L. Drew, and E. Bedolla. Wettability and spreading kinetics of Al and Mg on TiC. *Scripta Materialia*, 48(12):1625–1630, 2003.

[109] F. G. Yost. Kinetics of reactive wetting. *Scripta Materialia*, 42(8):801–806, 2000.

[110] A. Mortensen, B. Drevet, and N. Eustathopoulos. Kinetics of diffusion-limited spreading of sessile drops in reactive wetting. *Scripta Materialia*, 36(6):645–651, 1997.

[111] K. Landry and N. Eustathopoulos. Dynamics of wetting in reactive metal/ceramic systems: Linear spreading. *Acta Materialia*, 44(10):3923–3932, 1996.

[112] N. Eustathopoulos, J. P. Garandet, and B. Drevet. Influence of reactive solute transport on spreading kinetics of alloy droplets on ceramic surfaces. *Philosophical Transactions Of The Royal Society Of London Series A – Mathematical Physical And Engineering Sciences*, 356(1739):871–884, 1998.

[113] B. Drevet, K. Landry, P. Vikner, and N. Eustathopoulos. Influence of substrate orientation on wetting kinetics in reactive metal/ceramic systems. *Scripta Materialia*, 35(11):1265–1270, 1996.

[114] K. Landry, S. Kalogeropoulou, N. Eustathopoulos, Y. Naidich, and V. Krasovsky. Characteristic contact angles in the aluminiumn/vitreous carbon system. *Scripta Materialia*, 34(6):841–846, 1996.

[115] L. Espie, B. Drevet, and N. Eustathopoulos. Experimental-study of the influence of interfacial energies and reactivity on wetting in metal-oxide systems. *Metallurgical And Materials Transactions A-Physical Metallurgy And Materials Science*, 25(3):599–605, 1994.

[116] N. Eustathopoulos. Progress in understanding and modeling reactive wetting of metals on ceramics. *Current Opinion In Solid State & Materials Science*, 9(4-5):152–160, 2005.

[117] R. Voitovitch, A. Mortensen, F. Hodaj, and N. Eustathopoulos. Diffusion-limited reactive wetting: Study of spreading kinetics of Cu-Cr alloys on carbon substrates. *Acta Materialia*, 47(4):1117–1128, 1999.

[118] F. G. Yost, J. R. Michael, and E. T. Eisenmann. Extensive wetting due to roughness. *Acta Metallurgica Et Materialia*, 43(1):299–305, 1995.

[119] V. H. Lopez and A. R. Kennedy. Flux-assisted wetting and spreading of Al on TiC. *Journal Of Colloid And Interface Science*, 298(1):356–362, 2006.

[120] I. Jimbo and A. W. Cramb. Computer-aided interfacial measurements. *ISIJ International*, 32(1):26–35, 1992.

[121] M. Merola, M. Akiba, V. Barabash, and I. Mazul. Overview on fabrication and joining of plasma facing and high heat flux materials for ITER. *Journal Of Nuclear Materials*, 307:1524–1532, December 2002.

[122] J. Boscary, H. Greuner, B. Mendelevitch, B. Schedler, K. Scheiber, J. Schlosser, and B. Streibl. Applied technologies and inspections for the W7-X pre-series target elements. *Fusion Engineering And Design*, 75-9:451–455, 2005.

[123] J. Schlosser, E. Martin, C. Henninger, J. Boscary, G. Camus, F. Escourbiac, D. Leguillon, M. Missirlian, and R. Mitteau. CFC/Cu bond damage in actively cooled plasma facing components. *Physica Scripta*, T128:204–208, 2007.

[124] *http://www.wesgometals.com.*

[125] M. Singh, T. P. Shpargel, and R. Asthana. Brazing of yttria-stabilized zirconia (YSZ) to stainless steel using Cu, Ag, and Ti-based brazes. *Journal Of Materials Science*, 43(1):23–32, 2008.

[126] W. A. Rachinger. A correction for the alpha-1,alpha-2 doublet in the measurement of widths of X-ray diffraction lines. *Journal Of Scientific Instruments And Of Physics In Industry*, 25(7):254–255, 1948.

[127] M. M. Hall, V. G. Veeraraghavan, H. Rubin, and P. G. Winchell. Approximation of symmetric X-ray peaks by pearson type-7 distributions. *Journal Of Applied Crystallography*, 10(FEB1):66–68, 1977.

[128] *http://www.unipress.waw.pl/fityk/. Fityk - A curve fitting and data analysis program.*

[129] S. M. Schwarz, B. W. Kempshall, L. A. Giannuzzi, and M. R. McCartney. Avoiding the curtaining effect: Backside milling by FIB INLO. *Microscopy And Microanalysis*, 9(2):116–117, 2003.

[130] P. Formanek and E. Bugiel. Specimen preparation for electron holography of semiconductor devices. *Ultramicroscopy*, 106(4-5):365–375, 2006.

[131] *http://www.g-v-b.de.*

[132] L. Karlsson, L. Hultman, and J. E. Sundgren. Influence of residual stresses on the mechanical properties of $TiC_xN_1 - x$ (x = 0, 0.15, 0.45) thin films deposited by arc evaporation. *Thin Solid Films*, 371(1-2):167–177, 2000.

[133] P. Majumdar, S. B. Singh, and M. Chakraborty. Elastic modulus of biomedical titanium alloys by nano-indentation and ultrasonic techniques - a comparative study. *Materials Science And Engineering A-Structural Materials Properties Microstructure And Processing*, 489(1-2):419–425, 2008.

[134] H. Ogi, S. Kai, H. Ledbetter, R. Tarumi, M. Hirao, and K. Takashima. Titanium's high-temperature elastic constants through the hcp-bcc phase transformation. *Acta Materialia*, 52(7):2075–2080, 2004.

[135] O. N. Senkov, M. Dubois, and J. J. Jonas. Elastic moduli of titanium-hydrogen alloys in the temperature range 20 degrees c to 1100 degrees c. *Metallurgical And Materials Transactions A-Physical Metallurgy And Materials Science*, 27(12):3963–3970, December 1996.

[136] A. Buch. *Pure Metals Properties.* ASM International and Freund publishing House Ltd., 1999.

[137] M. Peters, C. Leyens, and J. Kumpfert, editors. *Titan und Titanlegierungen.* Werkstoff-Informationsgesellschaft, 2nd edition, 1998.

[138] *http://www.timet.com.*

[139] *http://en.wikipedia.org/wiki/Titanium.*

[140] D. Munz and T. Fett. *Ceramics: Mechanical Properties, Failure Behaviour, Materials Selection.* Springer, 1999.

[141] C. Kral, W. Lengauer, D. Rafaja, and P. Ettmayer. Critical review on the elastic properties of transition metal carbides, nitrides and carbonitrides. *Journal Of Alloys And Compounds*, 265(1-2):215–233, 1998.

[142] The International Centre for Diffraction Data (ICDD): powder diffraction files (PDF), database PDF-2, 2000.

[143] D. Zhong, E. Mateeva, I. Dahan, J. J. Moore, G. G. W. Mustoe, T. Ohno, J. Disam, and S. Thiel. Wettability of NiAl, Ni-Al-N, Ti-B-C, and Ti-B-C-N films by glass at high temperatures. *Surface & Coatings Technology*, 133:8–14, 2000.

[144] J. Zhu, A. Kamiya, T. Yamada, W. Shi, K. Naganuma, and K. Mukai. Surface tension, wettability and reactivity of molten titanium in Ti/yttria-stabilized zirconia system. *Materials Science And Engineering A-Structural Materials Properties Microstructure And Processing*, 327(2):117–127, 2002.

[145] H. N. Ho and S. T. Wu. The wettability of molten aluminum on sintered aluminum nitride substrate. *Materials Science And Engineering A-Structural Materials Properties Microstructure And Processing*, 248(1-2):120–124, 1998.

[146] P. Shen, H. Fujii, T. Matsumoto, and K. Nogi. Wetting of (0001) alpha-Al_2O_3 single crystals by molten Al. *Scripta Materialia*, 48(6):779–784, 2003.

[147] L. Yin, S. J. Meschter, and T. J. Singler. Wetting in the Au-Sn system. *Acta Materialia*, 52(10):2873–2888, 2004.

[148] G. Levi, M. Bamberger, and W. D. Kaplan. Wetting of porous titanium carbonitride by Al-Mg-Si alloys. *Acta Materialia*, 47(14):3927–3934, 1999.

[149] S. Tanaka and C. Iwamoto. Reactive wetting dynamics on 6H-SiC surface with oxide layer. *Aicam 2005*, 11-12:571–574, 2006.

[150] J. G. Li. Kinetics of wetting and spreading of Cu-Ti alloys on alumina and glassy-carbon substrates. *Journal Of Materials Science Letters*, 11(23):1551–1554, 1992.

[151] S. K. Roy, S. K. Bose, and S. C. Sircar. Pressure dependencies of copper oxidation for low-temperature and high-temperature parabolic laws. *Oxidation Of Metals*, 35(1-2):1–18, 1991.

[152] J. C. Yang, M. D. Bharadwaj, G. W. Zhou, and L. Tropia. Surface kinetics of copper oxidation investigated by in situ ultra-high vacuum transmission electron microscopy. *Microscopy And Microanalysis*, 7(6):486–493, 2001.

[153] I. Barin. *Thermochemical Data of Pure Substances*, volume 2. VCH Weinheim, 3rd edition, 1995.

[154] R. Tivey, M. Akiba, D. Driemeyer, I. Mazul, M. Merola, and M. Ulrickson. ITER R&D: Vacuum vessel and in-vessel components: Divertor cassette. *Fusion Engineering And Design*, 55(2-3):219–229, 2001.

[155] K. K. Hirakuri, K. Kuwashima, K. Tatsuta, and K. Sato. Etching of diamond-like carbon films deposited on polyethylene terephthalate. *Diamond And Related Materials*, 14(3-7):1067–1072, 2005.

[156] F. Eggenstein, F. Senf, T. Zeschke, and W. Gudat. Cleaning of contaminated XUV-optics at BESSY II. *Nuclear Instruments and Methods In Physics Research Section A – Accelerators Spectrometers Detectors And Associated Equipment*, 467:325–328, 2001.

[157] C. Hopf, W. Jacob, and V. Rohde. Oxygen glow discharge cleaning in nuclear fusion devices. *Journal Of Nuclear Materials*, 374(3):413–421, 2008.

[158] W. Jacob, B. Landkammer, and C. H. Wu. Removal of codeposited layers by ECR discharge cleaning. *Journal Of Nuclear Materials*, 266:552–556, 1999.

[159] B. Landkammer, A. von Keudell, and W. Jacob. Erosion of thin hydrogenated carbon films in oxygen, oxygen/hydrogen and water plasmas. *Journal Of Nuclear Materials*, 264(1-2):48–55, 1999.

[160] M. Avalle, A. Ventrella, M. Ferraris, and M. Salvo. Comparison of different shear test configurations for joined ceramics and CMCs: 29th International Conference on Advanced Ceramics and Composites, Cocoa Beach, January 23th-28th. 2005.

[161] H. Greuner, H. Bolt, B. Böswirth, T. Franke, P. McNeely, S. Obermayer, N. Rust, and R. Suss. Design, performance and construction of a 2 MW ion beam test facility for plasma facing components. *Fusion Engineering And Design*, 75-9:345–350, 2005.

[162] *ABAQUS/Standard, Version 6.8, Abaqus Inc., Providence, RI, 2008.*

[163] H. Greuner, A. Herrmann, H. Renner, P. Chappuis, and R. Mitteau. *Development of Divertor Targets for WENDELSTEIN 7-X*, 1998.

[164] M. Scheerer, H. Bolt, A. Gervash, J. Linke, and I. Smid. The design of actively cooled plasma-facing components. *Physica Scripta*, T91:98–103, 2001.

[165] J. Schlosser. *Update of Thermal Hydraulic Data Base. Pco/95-12, CEA Cadarache.*

[166] A. Herrmann. *Interface Optimization of Tungsten Fiber-Reinforced Copper for Heat Sink Application.* PhD thesis, Technische Universität, München, 2008.

[167] W. R. Gambill and R. F. Lopina. Discussion of heat transfer and pressure drop in tape-generated swirl flow of single-phase water. *Journal Of Heat Transfer*, 91(3):442, 1969.

[168] *VDI-Wärmeatlas, volume 3. VDI, Düsseldorf, 1977.*

[169] K. Stephan. *Wärmeübergang beim Kondensieren und beim Sieden.* Springer Verlag, Berlin, 1988.

[170] L. S. Tong and G. F. Hewitt. Overall viewpoint of flow boiling CHF mechanisms. *Mechanical Engineering*, 94(9):56, 1972.

[171] L. S. Tong. Phenomenological study of critical heat-flux. *Mechanical Engineering*, 97(12):105–105, 1975.

[172] U. Diebold. The surface science of titanium dioxide. *Surface Science Reports*, 48(5-8):53–229, 2003.

[173] M. P. Delplancke Ogletree and O. R. Monteiro. Deposition of titanium carbide films from mixed carbon and titanium plasma streams. *Journal Of Vacuum Science & Technology A-Vacuum Surfaces And Films*, 15(4):1943–1950, 1997.

[174] W. Eckstein. *Computer Simulation of Ion-Solid Interactions.* Springer Series in Materials Science 10. Springer, 1991.

[175] S. Levchuk. *Interface development for a EUROFER steel matrix composite with SiC-fibre reinforcement.* PhD thesis, Technische Universität, München, 2006.

[176] S. Inoue, Y. Wada, and K. Koterazawa. Deposition of TiC films by dual source dc magnetron sputtering. *Vacuum*, 59(2-3):735–741, 2000.

[177] P. Appendino, M. Ferraris, V. Casalegno, M. Salvo, M. Merola, and M. Grattarola. Proposal for a new technique to join CFC composites to copper. *Journal Of Nuclear Materials*, 348(1-2):102–107, 2006.

[178] *http://de.wikipedia.org/wiki/Rutil.*

[179] J. A. Thornton. Influence of apparatus geometry and deposition conditions on structure and topography of thick sputtered coatings. *Journal Of Vacuum Science & Technology*, 11(4):666–670, 1974.

[180] D. W. Hoffman and J. A. Thornton. Internal-stresses in Cr, Mo, Ta, and Pt films deposited by sputtering from a planar magnetron source. *Journal Of Vacuum Science & Technology*, 20(3):355–358, 1982.

[181] P. Worbs. Studie zur Beeinflussung von intrinsischen Spannungen in zerstäubten Wolframschichten. Semester thesis, Technische Universität, München, 2004.

[182] Z. Li-na, L. Guo-lu, W. Hai-dou, X. Bin-shi, Z. Da-ming, and L. Jia-jun. Microstructures and nano mechanical properties of the metal tungsten film. *Current Applied Physics*, 9(2):510–514, 2009.

[183] J. Tranchant, B. Angleraud, P. Y. Tessier, M. P. Besland, J. P. Landesman, and M. A. Djouadi. Residual stress control in MoCr thin films deposited by ionized magnetron sputtering. *Surface & Coatings Technology*, 200(22-23):6549–6553, 2006.

[184] S. Zhang, H. Xie, X. T. Zeng, and P. Hing. Residual stress characterization of diamond-like carbon coatings by an X-ray diffraction method. *Surface & Coatings Technology*, 122(2-3):219–224, 1999.

[185] H. Asada, Y. Kishi, and Y. Hirose. Measurement of youngs moduli of TiC-coated film by the X-ray-method. *Thin Solid Films*, 236(1-2):247–252, 1993.

[186] M. B. Bever and C. F. Floe. Solubility of carbon in molten copper. *Transactions Of The American Institute Of Mining And Metallurgical Engineers*, 166:128–143, 1946.

[187] P. R. Subramanian and D. E. Laughlin. *Phase Diagrams of Binary Copper Alloys*, 1994.

[188] M. G. Nicholas. Reactive metal brazing of ceramics. *Scandinavian Journal Of Metallurgy*, 20(2):157–164, 1991.

[189] X. B. Zhou and J. T. M. de Hosson. Reactive wetting of liquid metals on ceramic substrates. *Acta Materialia*, 44(2):421–426, 1996.

[190] L. Ramqvist. Wetting of metallic carbides by liquid copper, nickel, cobalt, and iron. *Int. J. Powder Metallurgy*, 1:2–21, 1965.

[191] H. Goretski, H. E. Exner, and W. Scheuermann. *Fundament. Sinter.*, 4:327, 1971.

[192] D. A. Mortimer. *AERE-R7941 cited by: R. Standing and M. Nicholas. J. Mater. Sci., 13, p. 1509, 1978*, 1975.

[193] P. Xiao and B. Derby. Wetting of titanium nitride and titanium carbide by liquid metals. *Acta Materialia*, 44(1):307–314, 1996.

[194] J. O. Andersson, T. Helander, L. H. Hoglund, P. F. Shi, and B. Sundman. THERMO-CALC & DICTRA, computational tools for materials science. *Calphad-Computer Coupling Of Phase Diagrams And Thermochemistry*, 26(2):273–312, 2002.

[195] A. Borgenstam, A. Engstrom, L. Hoglund, and J. Agren. DICTRA, a tool for simulation of diffusional transformations in alloys. *Journal Of Phase Equilibria*, 21(3):269–280, 2000.

[196] J. O. Andersson, L. Höglund, B. Jönsson, and J. Ågren. *Computer Simulation of Multicomponent Diffusional Transformations in Steel. Fundamentals and Applications of Ternary Diffusion.* Pergamon Press, New York, 1990.

[197] M. G. Nicholas. Active Metal Brazing. *British Ceramic Transactions And Journal*, 85(4):144–146, 1986.

[198] N. R. Frage, Y. G. Gurevich, A. V. Sokolova, and V. I. Chumanov. Stability of titanium carbide in molten iron and nickel. *Russian Metallurgy*, 3(3):30–34, 1989.

[199] K. Landry, C. Rado, R. Voitovich, and N. Eustathopoulos. Mechanisms of reactive wetting: The question of triple line configuration. *Acta Materialia*, 45(7):3079–3085, 1997.

[200] C. Rado, B. Drevet, and N. Eustathopoulos. The role of compound formation in reactive wetting: The Cu/SiC system. *Acta Materialia*, 48(18-19):4483–4491, 2000.

[201] R. N. Wenzel. Resistance of solid surfaces to wetting by water. *Industrial And Engineering Chemistry*, 28:988–994, 1936.

[202] A. B. D. Cassie and S. Baxter. Wettability of porous surfaces. *Transactions Of The Faraday Society*, 40:0546–0550, 1944.

[203] A. T. Peacock, M. Merola, M. A. Pick, and R. Tivey. Status of CFC development in europe for ITER. *Physica Scripta*, T128:23–28, 2007.

Acknowledgements

Zum Gelingen dieser Arbeit haben eine Vielzahl an Personen beigetragen, denen ich hiermit danken möchte.

Mein besonderer Dank gilt meinem Doktorvater **Prof. Dr. Dr. Harald Bolt**, der mir die Durchführung dieser Arbeit am IPP ermöglichte. Für seine Unterstützung und sein Interesse an meiner Arbeit möchte ich Ihm herzlichst danken. Für seine Aufgaben am Forschungszentrum Jülich wünsche ich Ihm alles Gute und weiterhin viel Erfolg.

Bei **Prof. Dr. E.Werner** möchte ich mich für die Bereitstellung als Zweitgutachter bedanken. **Prof. Dr. H. Baier** danke ich für die freundliche Unterstützung, meine Promotion an der Fakultät für Maschinenwesen durchführen zu können.

Mein größter Dank gilt meinem Betreuer **Dr. Hans Maier**, der mir in den letzten drei Jahren der Zusammenarbeit stets mit Rat und Tat zur Seite stand. Sein Vertrauen in mich, sein beeindruckendes fachliches Wissen und seine intensive Unterstützung bei Experimenten und der Anfertigung dieser Arbeit sowie die vielen hilfreichen Diskussionen werde ich nie vergessen. Herzlichen Dank!

Im Besonderen möchte ich meiner Zimmernachbarin **Dr. Aurelia Herrmann** für Ihre hilfsbereite und vertrauensspendende Art danken. Unsere zahlreichen gemeinsamen Aktivitäten, sei es sportlich oder gesellschaftlich, werden mir stets in Erinnerung bleiben.

Dr. Klaus Schmid war für mich des Öfteren so etwas wie ein "Retter in letzter Not". Für seine Unterstützung in thermodynamischen sowie in physikalischen Angelegenheiten danke ich Ihm sehr. Außerdem bedanke ich mich bei meinem "Seilpartner" für unsere bergsportlichen Abenteuer.

Für dringende und wichtige technische Arbeiten bedanke ich mich bei **Josef Schäftner**, **Albert Holzer** und **Reinhard Hoffmann**, im Besonderen aber bei **Werner Hohlenburger** bei seiner Hilfe zum Aufbau der Benetzungsanlage. Ebenso danke ich **Henri Greuner** und vor allem **Bernd Böswirth** für die tatkräftige Unterstützung bei der Durchführung der Experimente am Wärmeflussteststand GLADIS. **Jean Boscary** danke ich für die Bereitstellung vom CFC Material, **Gaby Matern** für die großartige Unterstützung in der Metallographie und Ihr Interesse an meinen bergsportlichen wie musikalischen Tätigkeiten sowie **Dr. Christian Linsmeier** für sein offenes Ohr, seine motivierenden Worte und für die Leitung und Organisation des hilfreichen Doktorandenseminars.

Durch die Teilnahme am EU Projekt ExtreMat durfte ich vielen besonderen Personen begegnen bei denen ich mich für die vielen wertvollen Tipps und die erfolgreiche Zusammenarbeit bedanken möchte. Mein Dank geht an **Dr. Carlo Gualco** und **Marco Grattarola** von Ansaldo Ricerche, an **Dr. Bernhard Schwarz** von der TU Wien und **Calvin Prentice** von Archer Technicoat. Einen lieben Dank widme ich meinen Kolleginnen **Inmaculada López Galilea** von CEIT und **Alba Centeno** von INCAR für ganz besondere Momente.

Für das angenehme Arbeitsklima und die Unterstützung bei Problemen aller Art geht ein ganz großes Dankeschön an alle Kollegen des Bereichs MF, speziell an die Arbeitsgruppe MSC. Ohne das viele Know-How und die Hilfe, die ich jederzeit von Euch erhalten habe, hätte ich diese Arbeit nicht stemmen können. Besonderen Dank schulde ich **Freimut Koch**

für die Sputter-Unterstützung, **Dr. Martin Balden** und **Stefan Lindig** für die Hilfe mit XRD, FIB und SEM und **Till Höschen** für sein technisches Wissen im Zusammenhang mit mechanischen Testversuchen. Außerdem danke ich **Dr. Thomas Schwarz-Selinger** für seine Unterstützung bei den Sauerstoff-Plasma Erosionsversuchen. **Marcin Rasinski** danke ich für die zeitaufwendigen Arbeiten an der FIB und **Dr. Jeong-Ha You** für die Einführung in ABAQUS. **Arno Weghorn** sowie dem Beschleuniger-Team mit **Joachim Dorner** und **Michael Fußeder** danke ich für lustige Kaffee-Runden und das bayrische Ambiente.

Ein ganz großer Dank gilt den Mitdoktoranden, Diplomanden und Praktikanten: **Verena Paffenholz**, **Martin Oberkofler**, **Thomas Köck**, **Florian Kost**, **Christoph Adelhelm**, **Juan Du**, **Yury Gasparyan**, **Beata Tyburska**, **Khadija Chaoui**, **Cecile Lavergne**, **Rainer Piechozek**, **Heun Lee**, **Matthias Reinelt**, **Alessandro Zivelonghi**, **Johann Riesch**, **Martin Köppen** und **Thomas Pickert**. Herzlichen Dank für Eure Unterstützung und vielen Hilfen. Unsere gemeinsamen Unternehmungen haben die Zeit für mich unvergesslich gemacht.

Im Besonderen möchte ich mich bei **Itxaso Segues Guridi** bedanken. Ihre wohltuende und charmante Art sowie unsere vielen gemeinsamen Tanzstunden werde ich nie vergessen.

Meinen **Eltern** und meinen **Schwestern** danke ich für Ihre liebevolle Unterstützung und ihr stetes Interesse an meiner Arbeit. Bei meinen **Freunden** und dem **Swing Orchestra Taufkirchen/Vils** bedanke ich mich besonders für die sportliche, musikalische und spirituelle Abwechslung während meiner Doktorarbeit. Ein herzliches Vergelt's Gott!